SENSORED AND SENSORLESS FIELD ORIENTED CONTROL FOR AN INDUCTION MOTOR DRIVE

A Project Report

submitted by

JOSE TITUS

in partial fulfilment of the requirements
for the award of the degree of

MASTER OF TECHNOLOGY

DEPARTMENT OF ELECTRICAL ENGINEERING
INDIAN INSTITUTE OF TECHNOLOGY MADRAS.

MAY 2014

THESIS CERTIFICATE

This is to certify that the thesis titled **SENSORED AND SENSORLESS VECTOR CONTROL OF AN INDUCTION MOTOR DRIVE**, submitted by **JOSE TITUS**, to the Indian Institute of Technology, Madras, for the award of the degree of **Master of Technology**, is a bona fide record of the project work done by him under my supervision. The contents of this thesis, in full or in parts, have not been submitted to any other Institute or University for the award of any degree or diploma.

Dr. Kamalesh Hatua
(Project Guide)
Asst.Professor
Dept. of Electrical Engineering
IIT-Madras, 600 036

Place: Chennai

Date: 1st May 2014

ACKNOWLEDGEMENTS

It gives me great pleasure to express my sincere and heartfelt gratitude to Dr. Kamalesh Hatua for his excellent guidance, motivation and constant support throughout my project . I consider myself extremely fortunate to have had a chance to work under his supervision. In spite of his hectic schedule he was always approachable and took his time off to discuss problems and give his advice and encouragement. I am also grateful for the laboratory facilities provided by him in the Power Electronics Simulation Laboratory and the Electrical Machines Laboratory, Department of Electrical Engineering, which facilitated my work.

I am grateful to Dr. Krishna Vasudevan for his enlightning lectures on Machine Modelling which instilled my passion for the subject. I also thank Dr. Srirama Srinivas and Dr. Lakshminarasamma for their help and support throughout the course of this project.

I thank Mr. Kothandaraman and Ms. Jayasudha for their help and advice in arranging the hardware setup. I also thank Mr. Balaganesh, Mr.Pandian and all the other staff of the central fabrication facility for their help during the hardware setup.

My appreciation to my fellow students in the Power Electronics Simulation Laboratory, especially Jayendra and Vasudev for spending their invaluable time with me, in discussing about the project, goes well beyond words. I would also extend my thanks to Neelesh, Parthasarathy, Hridya and Lokesh for their support during my work.

This work could not have come to this stage without the support and encouragement from my family. My heartfelt thanks to all of them.

ABSTRACT

KEYWORDS: Vector Control; Field Oriented Control; Sensorless Control

Vector Control or Field Oriented Control of Induction motors refers to a high performance control scheme which gives excellent dynamic torque and speed response similar to that from a DC machine. In this scheme the induction machine is modeled similar to a DC machine by transforming the currents and voltages to a rotor flux frame of reference. The control attempts to independently control the torque producing and flux producing components of the input current from a knowledge of the instantaneous angular position of the rotor flux space vector.

This project work has been carried out as part of the technical consultancy for developing a 1 MW, low voltage, vector controlled induction motor drive for BHEL. *Simulation studies are done for the 1 MW machine* using MATLAB/SIMULINK to verify the design of the power circuit and control algorithms for sensored and sensorless vector control. The control hardware is developed based on the TMS320F28335 DSP from Texas Instruments. The system design and control software for sensored and sensorless vector control is *experimentally validated on a scaled down model of a 30 kW induction machine*. An improved algorithm for estimating the rotor flux has been used in the sensorless control giving excellent low speed operation of upto upto 1 Hz stator frequency.

TABLE OF CONTENTS

LIST OF TABLES

LIST OF FIGURES

ABBREVIATIONS

FOC	Field Oriented Control
SCIM	Squirrel Cage Induction Machine
PI	Proportional and Integral
DC	Direct Current
CCS	Code Composer Studio
VSI	Voltage Source Inverter
PWM	Pulse Width Modulation
SVPWM	Space Vector Pulse Width Modulation
PD	Protection and Delay
ADC	Analog to Digital Converter
eCAP	Enhanced Capture
PEK	Peripheral Explorer Kit
QEP	Quadrature Encoder Pulse
SCI	Serial Communication Interface
SPI	Serial Peripheral Interface
CAN	Controller Area Network
$\boldsymbol{I^2C}$	Inter Integrated Circuit
JTAG	Joint Test Action Group
DMA	Direct Memory Access
PIE	Peripheral Interrupt Expansion
OTP	One Time Programmable
SARAM	Single Access RAM
IGBT	Insulated Gate Bipolar Transistor

NOTATION

v_a, v_b, v_c	Instantaneous voltages in abc frame, V
$v_{s\alpha}, v_{s\beta}$	Instantaneous stator voltages in $\alpha\beta$ frame, V
v_{sd}, v_{sq}	Instantaneous stator voltages in dq frame, V
i_{sd}, i_{sq}	Instantaneous stator currents in dq frame, A
$i_{s\alpha}, i_{s\beta}$	Instantaneous stator currents in $\alpha\beta$ frame, A
$i_{r\alpha}, i_{r\beta}$	Instantaneous rotor currents in $\alpha\beta$ frame, A
$\psi_{s\alpha}, \psi_{s\beta}$	Instantaneous stator flux in $\alpha\beta$ frame, Wb
$\psi_{r\alpha}, \psi_{r\beta}$	Instantaneous rotor flux in $\alpha\beta$ frame, Wb
L_s	Stator inductance , mH
L_r	Rotor inductance , mH
L_m	Magnetising inductance , mH
L_{ls}	Stator leakage inductance , mH
L_{lr}	Rotor leakage inductance , mH
R_s	Stator resistance , Ω
R_r	Rotor resistance , Ω
τ_r	Rotor time constant , sec
V_d	Inverter DC bus voltage, V
ω_{mr}	Rotor flux speed, $elect.rad/s$
ω	Rotor speed, $elect.rad/s$
ω_m	Rotor speed, rad/s
ω_{slip}	Slip speed, $elect.rad/s$
K_p	Proportional gain of the PI controller
K_i	Integral gain of the PI controller
T_s	Sampling time for the control loops
G_i	Gain of the inverter

CHAPTER 1

INTRODUCTION

The development of the first induction machine by Nikola Tesla in 1888, marked a revolution in electrical engineering. The simple structure and robustness of the induction machine made it the most preffered machine for industrial applications. However, when directly operated from the 50 Hz AC grid, this machine operates only at speeds near sychronous speed. Thus for applications requiring the speed to vary in wide range, the dc machine continued to be the machine of choice. Later, with the advent of power electronic devices, new control techniques were developed for speed control for both AC and DC machines. Most of these earlier induction motor drives were based on keeping a constant voltage/frequency (V/f) ratio in order to maintain a constant flux inside the machine. While the V/f control of induction motor is relatively simple, the dynamic performance is extremely poor. Thus separately excited DC machines continued to dominate in applications requiring good dynamic performance. It was the development of the field oriented control technique that gave the decisive impulse to the induction machine drives to compete with separately excited DC machines in high performance applications.

1.1 Vector Control

The principle of Vector Control or Field Oriented Control (FOC) was originally developed by F. Blaschke and K. Hasse in Germany by the late 1960s. In a separately excited DC machine, the flux producing current and the torque producing current are supplied to two separate windings. Because of this fact, the speed control of DC machines can be easily achieved as these two components can be independently controlled. However, in induction machines there is only a three phase winding excited by a three phase source. Hence it is difficult to separate the two componenets of the input current. In vector control technique, the flux producing component and the torque producing component of the input current is

identified and controlled separately in a similar fashion to that of a separately excited DC machine. This is done by transforming the instantaneous stator currents to a rotating frame of reference aligned with the rotor flux axis. This requires accurate information about the instantaneous position of the rotor flux. Blaschke[8] used Hall sensors embedded in the stator to measure the air gap flux and obtain the angular position. This method wherein the flux is directly measured is called Direct Field Orientation (DFO). Hasse used the rotor speed information in the rotor dynamic equations of the machine to calculate the flux position. This method is known as the Indirect Field Orientation (IFO). Both IFO and DFO uses the information about flux position to transform the stator currents to the rotating d-q frame aligned to the rotor flux. The direction of the instantaneous rotor flux is taken as the d-axis direction. The direction of q-axis is taken to be 90° leading the d-axis. IFO is generally preferred to DFO as DFO requires a specially modified machine and also the use of Hall sensors makes the machine less robust.

Though the technique of vector control was developed as early as the 1970's it could not be readily applied, as the method is computationally intensive. However, with the advances in the area of microelectronics, powerful digital signal processors are available today that can easily implement vector control algorithms.

1.1.1 Speed sensor-less vector control

The use of vector controlled induction motor drives provides several advantages over DC machines in terms of robustness, size, lack of brushes, and reduced cost and maintenance. The most important part of the vector control technique is an accurate alignment of the d-q reference frame to the rotor flux vector. In a typical vector controlled drive this is achieved by using an accurate shaft encoder, which outputs a fixed number of pulses for every rotation. However, the use of such an encoder requires additional circuitry like level shifters and differential recievers for proper interfacing with the controller, additional wiring from the encoder to the drive, and careful and precise mounting to avoid vibrations. Also these can be used only with motors that have a shaft extension at the non-driving end. Also precise encoders are expensive and in the low power ranges, the cost of the encoder can be about the same as that for the motor. These factors makes the drive less robust

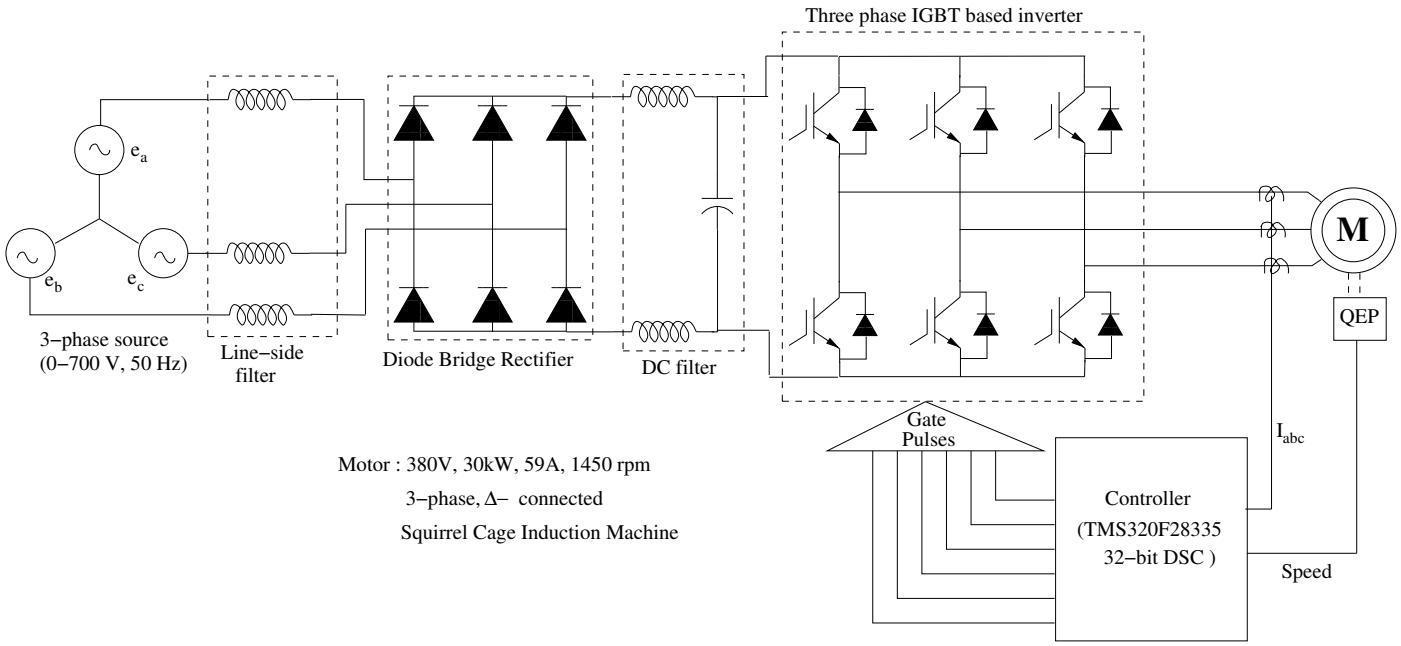

Figure 1.1: Power structure of the drive

and offsets its advantages over the DC machine. Therefore a control strategy that avoids the use of speed sensor is clearly advantageous. Such a scheme of control that does not require a speed sensor for its operation is called the sensorless vector control. In sensorless vector control scheme, the rotor flux position is estimated using the sensed values of motor line currents and the inverter DC bus voltage.

Speed feedback is essential in any drive for performing speed control. In sensorless vector controlled drives, speed estimation techniques that utilise the dynamic model of the induction machine are generally used. In such drives, speed is obtained from the measured instantaneous values of the phase currents and phase voltages. The accuracy of control depends on the accuracy of estimated flux position. These drives generally have good performance at high speeds. However, sensorless drives that use stator voltage integration techniques have poor performance at low speeds due to drift problems associated with the integrator.

1.2 Power structure of the drive

The power structure of the drive used is as shown in Fig. 1.1. The three phase balanced supply from the regulating transformer is rectified by a three phase diode bridge rectifier to obtain the required DC bus voltage. A precharging circuit con-

sisting of a resistor in parallel with a relay is used to prevent large inrush currents that may damage the DC bus capacitor. The relay bypasses the resistor from the circuit when the capacitor voltage has built up to a large enough value. The rectifier normally draws distorted and peaky currents from the supply and hence an inductance is used in series with the line to make the currents smoother. The rectified output is then given to the inverter whose switching signals are controlled suitably to obtain the required voltage. Wide bandwidth, high precision, Hall effect sensors are used to sense the instantaneous line currents for feedback. The DC bus voltage is also sensed by using a precision Hall effect sensor. A quadrature encoder connected to the shaft at the non-driving end is used to obtain the speed information of the machine for sensored control. The controller is a 32-bit floating point Digital Signal Controller(DSC), from Texas Instruments. The control algorithm running on the processor senses the feedback signals through the built-in Analog-Digital Converter(ADC) on the controller and processes these information to generate the required switching pulses.

1.3 Organisation of Thesis

Chapter 2 presents a detailed description on the theory of space phasors and induction machine modelling. The space phasor model of the induction machine is presented and the dynamic equations of the machine in the rotor flux frame of reference is obtained. The theory of Field Oriented Control (FOC) is presented along with the relevant equations.

Chapter 3 deals with the hardware organisation for the implementation of vector control on a 30 kW laboratory prototype. Some of the basic capablilities and features of the control platform based on the TMS320F28335 Digital Signal Controller (DSC), from Texas Instruments, that are used in the control implementation, are also discussed. Also the additional circuitry developed for interfacing the sensed signals with the controller, and the protection and delay card that acts as the interface between the controller and the inverter are discussed.

Chapter 4 describes the digital implementation of the vector control system. The design of current controllers and speed controllers used in the vector control scheme are presented. The per unitisation and discretisation of all the algorithms

used in sensored and sensorless vector control are also presented along with other control blocks like low pass filters and the space vector modulator for the inverter.

Chapter 5 discusses the results obtained from the simulation for the 1 MW induction motor drive as well as that from the actual hardware implementation on the 30 kW induction motor.

Chapter 6 presents the summary of the work done and the future scope for improving the work.

CHAPTER 2

SPACE PHASOR MODELLING AND FIELD ORIENTED CONTROL OF INDUCTION MACHINES

2.1 Introduction

The basic theoretical framework of the Field Oriented Control is derived from the space phasor modelling of induction machines. In this approach, three-phase voltages, currrents and fluxes of the machine are analysed in terms of complex space vectors. The control then uses coordinate reference frame transformations that transform a three phase time and speed dependent system to a two coordinate time invariant system. Thus a clear understanding of the idea of space phasor modelling of the induction machine as well as the various coordinate transformations is important for understanding the vector control of induction machine.

In this chapter the basic theory of FOC is presented from the dynamic space phasor model of the induction machine. All the relevant equations for control are derived and the basic scheme for control is presented. The mathematical equations for different coordinate transforms used in vector control are also presented. These include transformations between the natural reference frame, the $\alpha\beta 0$ reference frame and the $dq0$ reference frame.

2.2 Space Phasors

The concept of space phasors[1] can be understood by considering the mmf due to currents flowing in a three phase distributed winding such as that in an induction machine. The three windings each having N_s equivalent number of turns are displaced by 120° as shown in Fig. 2.1 The mmf distribution is assumed to be

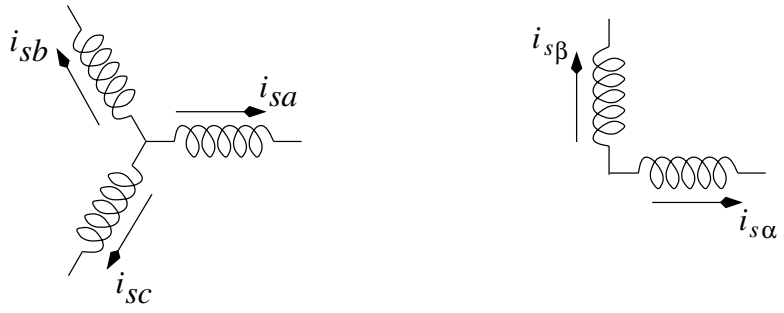

(a) (b)

Figure 2.1: Winding arrangement

sinusoidal and the neutral point is assumed to be isolated so that the currents in the three phases adds to zero at all instants of time.i.e.

$$i_{sa}(t) + i_{sb}(t) + i_{sc}(t) = 0 \tag{2.1}$$

where $i_{sa}(t)$, $i_{sb}(t)$ and $i_{sc}(t)$ denote the instantaneous values of the currents flowing into the a, b and c phase stator windings respectively. Taking the a-phase axis as the reference, the net mmf produced by all 3 coils is obtained by vectorially adding the individual coil mmfs.This net mmf is then given as

$$\begin{aligned} mmf_{3-\phi} &= N_s[i_{sa}(t) + i_{sb}(t)e^{j(2\pi/3)} + i_{sc}(t)e^{j(4\pi/3)}] \\ &= mmf_\alpha + jmmf_\beta \end{aligned}$$

where

$$\begin{aligned} mmf_\alpha &= N_s[i_{sa}(t) + i_{sb}(t)\cos(2\pi/3) + i_{sc}(t)\cos(4\pi/3)] \\ &= N_s[i_{sa}(t) - \frac{1}{2}i_{sb}(t) - \frac{1}{2}i_{sc}(t)] \qquad (2.2) \\ mmf_\beta &= N_s[i_{sb}(t)\sin(2\pi/3) + i_{sc}(t)\sin(4\pi/3)] \\ &= N_s[\frac{\sqrt{3}}{2}i_{sb}(t) - \frac{\sqrt{3}}{2}i_{sc}(t)] \qquad (2.3) \end{aligned}$$

Thus it is seen that the system of three coils can be replaced by an equivalent two coil system having the same number of turns N_s as the original set of coils and carrying currents $i_{s\alpha}(t)$ and $i_{s\beta}(t)$. Using the condition in 2.1, these currents can

be given as

$$i_{s\alpha}(t) = \frac{3}{2} i_{sa}(t) \tag{2.4}$$

$$i_{s\beta}(t) = \frac{\sqrt{3}}{2}[i_{sb}(t) - i_{sc}(t)] \tag{2.5}$$

The current space phasor is then defined as

$$\vec{i_s}(t) = i_{s\alpha}(t) + j i_{s\beta}(t) = i_s(t) e^{j\zeta(t)} \tag{2.6}$$

where

$i_s(t)$ - Instantaneous amplitude of the space phasor

$\zeta(t)$ - Instantaneous angle of the phasor w.r.t the reference

The space phasor can also be defined in terms of the actual 3-ϕ currents as

$$\vec{i_s}(t) = i_{sa}(t) + i_{sb}(t) e^{j(2\pi/3)} + i_{sc}(t) e^{j(4\pi/3)} \tag{2.7}$$

Similarly space phasors can be defined for other quantities suach as voltages and flux linkages associated with a three phase distributed winding.

2.3 Space Phasor model of the Induction machine

The three phase squirrel cage induction motor has a symmetrical, distributed three phase winding on the stator. The rotor has a cage structure, with conducting bars along the rotor axis, shorted at both ends by thick metallic rings. The stator, when supplied from a balanced three phase supply sets up the rotating magnetic field in the airgap of the machine. This field induces currents in the short ciruited rotor. These currents produce the rotor magnetic field which interacts with the stator magnetic field, and produces electromagnetic torque.

The squirrel cage rotor can be considered as equivalent to a three phase distributed winding. Thus the stator and rotor can then be represented by two sets of equivalent two phase coils as discussed in the previous section. This is shown in Fig. 2.2

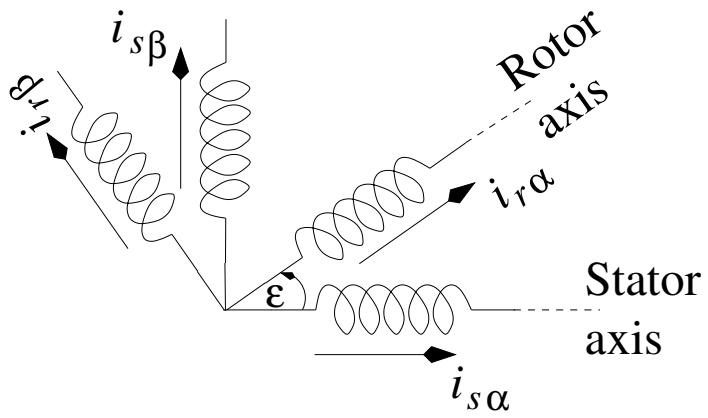

Figure 2.2: Equivalent coils for the stator and rotor circuit

The current space phasor for the stator and rotor currents can be written as,

$$\vec{i_s}(t) = i_{s\alpha}(t) + ji_{s\beta}(t) \tag{2.8}$$

$$\vec{i_r}(t) = i_{r\alpha}(t) + ji_{r\beta}(t) \tag{2.9}$$

where $\vec{i_s}$ is defined w.r.t stator coordinates and $\vec{i_r}$ is defined w.r.t rotor coordinates. The flux linkages of the stator and rotor coils as a function of time t, can then be written as

$$\psi_{s\alpha}(t) = L_s i_{s\alpha}(t) + L_m i_{r\alpha}(t)\cos\epsilon(t) - L_m i_{r\beta}(t)\sin\epsilon(t) \tag{2.10}$$

$$\psi_{s\beta}(t) = L_s i_{s\beta}(t) + L_m i_{r\alpha}(t)\sin\epsilon(t) + L_m i_{r\beta}(t)\cos\epsilon(t) \tag{2.11}$$

$$\psi_{r\alpha}(t) = L_r i_{r\alpha}(t) + L_m i_{s\alpha}(t)\cos\epsilon(t) + L_m i_{s\beta}(t)\sin\epsilon(t) \tag{2.12}$$

$$\psi_{r\beta}(t) = L_r i_{r\beta}(t) - L_m i_{s\alpha}(t)\sin\epsilon(t) + L_m i_{s\beta}(t)\cos\epsilon(t) \tag{2.13}$$

Then the stator and rotor flux space phasors can be written as

$$\begin{aligned} \vec{\psi_s}(t) &= \psi_{s\alpha}(t) + j\psi_{s\beta}(t) = L_s\vec{i_s}(t) + L_m\vec{i_r}(t)e^{j\epsilon(t)} \\ \vec{\psi_r}(t) &= \psi_{r\alpha}(t) + j\psi_{r\beta}(t) = L_r\vec{i_r}(t) + L_m\vec{i_s}(t)e^{-j\epsilon(t)} \end{aligned} \tag{2.14}$$

where

L_s - Self inductance of the stator coils

L_r - Self inductance of the rotor coils

L_m - Maximum value of mutual inductance between stator and rotor

The voltage equations of the machine can now be obtained in the space phasor

form by writing the voltage equations of the individual coils and adding them vectorially. The voltage equations for the individual coils as a function of time, t are given as

$$v_{s\alpha}(t) = R_s i_{s\alpha} + \frac{d\psi_{s\alpha}(t)}{dt} \tag{2.15}$$

$$v_{s\beta}(t) = R_s i_{s\beta} + \frac{d\psi_{s\beta}(t)}{dt} \tag{2.16}$$

$$v_{r\alpha}(t) = R_r i_{r\alpha} + \frac{d\psi_{r\alpha}(t)}{dt} \tag{2.17}$$

$$v_{r\beta}(t) = R_r i_{r\beta} + \frac{d\psi_{r\beta}(t)}{dt} \tag{2.18}$$

where R_s and R_r denote the resistances of the stator and rotor respectively. The stator and rotor voltage space vectors are then obtained as

$$\begin{aligned} \vec{v}_s(t) &= R_s \vec{i}_s(t) + \tfrac{d\vec{\psi}_s(t)}{dt} \\ \vec{v}_r(t) &= R_r \vec{i}_r(t) + \tfrac{d\vec{\psi}_r(t)}{dt} \end{aligned} \tag{2.19}$$

Using Eq. (2.14) in Eq. (2.19), the voltage space phasor equations can be written as

$$\vec{v}_s(t) = R_s \vec{i}_s(t) + L_s \frac{d\vec{i}_s(t)}{dt} + L_m \frac{d}{dt}[\vec{i}_r(t) e^{j\epsilon(t)}] \tag{2.20}$$

$$\vec{v}_r(t) = R_r \vec{i}_r(t) + L_r \frac{d\vec{i}_r(t)}{dt} + L_m \frac{d}{dt}[\vec{i}_s(t) e^{-j\epsilon(t)}] \tag{2.21}$$

These two complex space phasor equations defines the electrical behaviour of the machine. In a Squirrel cage induction machine, the rotor consists of short ciruited bars and hence $\vec{v}_r(t)$ is set to zero. The above equations can also be represented in the form of an equivalent circuit as shown in Fig.2.3. Here, all quantities are referred to the stator coordinate axes. It is interesting to note that the structure

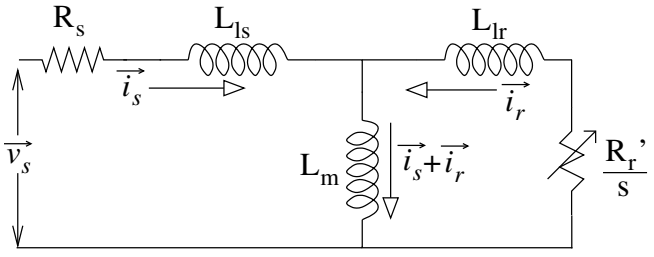

Figure 2.3: Space phasor equivalent circuit of the Induction machine

of the circuit is the same as that of the normal per phase equivalent circuit used for steady state analysis of the induction machine.

Expression for the developed electromagnetic torque An expression for the electromagnetic torque developed in the machine in terms of the space phasor quantities will now be derived. The voltage equations of the induction machine expressed in terms of machine variables[5] referred to stator windings may be written as

$$\begin{bmatrix} \boldsymbol{v}^s_{abc} \\ 0 \end{bmatrix} = \begin{bmatrix} \boldsymbol{r}_s + \mathrm{p}\boldsymbol{L}_s & p\boldsymbol{L}_{sr} \\ (\boldsymbol{L}_{sr})^T & \boldsymbol{L}_r \end{bmatrix} \begin{bmatrix} \boldsymbol{i}^s_{abc} \\ \boldsymbol{i}^r_{abc} \end{bmatrix}$$

where $\begin{bmatrix} \boldsymbol{v}^s_{abc} \end{bmatrix} = \begin{bmatrix} \mathrm{v}_{sa} & \mathrm{v}_{sb} & \mathrm{v}_{sc} \end{bmatrix}^T$ denotes the vector of stator phase voltages, $\begin{bmatrix} \boldsymbol{i}^s_{abc} \end{bmatrix} = \begin{bmatrix} \mathrm{i}_{sa} & \mathrm{i}_{sb} & \mathrm{i}_{sc} \end{bmatrix}^T$ is the stator current vector and $\begin{bmatrix} \boldsymbol{i}^r_{abc} \end{bmatrix} = \begin{bmatrix} \mathrm{i}_{ra} & \mathrm{i}_{rb} & \mathrm{i}_{rc} \end{bmatrix}^T$ is the rotor current vector. $\boldsymbol{r}_s$ and $\boldsymbol{r}_r$ are diagonal matrices of the stator and rotor resistances referred to the stator. Also, the inductance matrices are given as

$$\boldsymbol{L}_s = \begin{bmatrix} L_{ls} + L_{ms} & -\frac{1}{2}L_{ms} & -\frac{1}{2}L_{ms} \\ -\frac{1}{2}L_{ms} & L_{ls} + L_{ms} & -\frac{1}{2}L_{ms} \\ -\frac{1}{2}L_{ms} & -\frac{1}{2}L_{ms} & L_{ls} + L_{ms} \end{bmatrix}$$

$$\boldsymbol{L}_r = \begin{bmatrix} L_{lr} + L_{ms} & -\frac{1}{2}L_{ms} & -\frac{1}{2}L_{ms} \\ -\frac{1}{2}L_{ms} & L_{lr} + L_{ms} & -\frac{1}{2}L_{ms} \\ -\frac{1}{2}L_{ms} & -\frac{1}{2}L_{ms} & L_{lr} + L_{ms} \end{bmatrix}$$

$$\boldsymbol{L}_{sr} = L_{ms} \begin{bmatrix} \cos\epsilon & \cos(\epsilon + \frac{2\pi}{3}) & \cos(\epsilon - \frac{2\pi}{3}) \\ \cos(\epsilon - \frac{2\pi}{3}) & \cos\epsilon & \cos(\epsilon + \frac{2\pi}{3}) \\ \cos(\epsilon + \frac{2\pi}{3}) & \cos(\epsilon - \frac{2\pi}{3}) & \cos\epsilon \end{bmatrix}$$

where

L_{ls} - Stator leakage inductance.

L_{lr} - Rotor leakage inductance referred to stator.

L_{ms} - Stator magnetising inductance.

ϵ - electrical angle between the stator and the rotor axes.

The stored energy in the coupling field, W_f can now be written as

$$W_f = \frac{1}{2}[\boldsymbol{i}^s_{abc}]^T[\boldsymbol{L}_s - L_{ls}\boldsymbol{I}][\boldsymbol{i}^s_{abc}] + [\boldsymbol{i}^s_{abc}]^T[\boldsymbol{L}_{sr}][\boldsymbol{i}^r_{abc}] + \frac{1}{2}[\boldsymbol{i}^r_{abc}]^T[\boldsymbol{L}_r - L_{lr}\boldsymbol{I}][\boldsymbol{i}^r_{abc}] \quad (2.22)$$

where $\mathbf{I}$ denotes the identity matrix. Neglecting saturation effects and assuming a linear magnetic system, the field energy is equal to the co-energy, W_c. The torque is obtained as the partial derivative of the co-energy with the mechanical angle. Thus torque can be written as

$$M_d = \frac{\partial Wc(\boldsymbol{i}, \epsilon)}{\partial \theta_m} \quad (2.23)$$

where $\theta_m = \frac{2}{P}\epsilon$ denotes the mechanical angle of the rotor axis with the stator axis. Since the first and third terms in Eq.(2.22) are independent of θ_m, their partial derivatives with respect to θ_m go to zero. Hence only the second term needs to be considered in calculating the torque using Eq.(2.23). Evaluating the derivative of $\boldsymbol{L}_{sr}$ and substituting in Eq.(2.23) gives

$$M_d = -\frac{P}{2}L_{ms}[\boldsymbol{i}^s_{abc}]^T \begin{bmatrix} \sin\epsilon & \sin(\epsilon + \frac{2\pi}{3}) & \sin(\epsilon - \frac{2\pi}{3}) \\ \sin(\epsilon - \frac{2\pi}{3}) & \sin\epsilon & \sin(\epsilon + \frac{2\pi}{3}) \\ \sin(\epsilon + \frac{2\pi}{3}) & \sin(\epsilon - \frac{2\pi}{3}) & \sin\epsilon \end{bmatrix} \begin{bmatrix} \mathrm{i}_{ra} \\ \mathrm{i}_{rb} \\ \mathrm{i}_{rc} \end{bmatrix} \quad (2.24)$$

Substituting for sine terms using the formula, $\sin\theta = \frac{e^{j\theta} - e^{-j\theta}}{2j}$ and simplifying gives,

$$M_d = -\frac{1}{2j}\frac{P}{2}L_{ms}[\vec{i_r}\vec{i^*_s}e^{j\epsilon} - \vec{i^*_r}\vec{i_s}e^{-j\epsilon}] \quad (2.25)$$

where

$$\vec{i_r} = i_{ra} + i_{rb}e^{j(\frac{2\pi}{3})} + i_{rc}e^{-j(\frac{2\pi}{3})} \quad (2.26)$$

is the rotor current space vector. Eq.(2.25) can then be written as

$$\begin{aligned} M_d &= \frac{1}{2j}\frac{P}{2}L_{ms}[\vec{i^*_r}\vec{i_s}e^{-j\epsilon} - \vec{i_r}\vec{i^*_s}e^{j\epsilon}] \\ &= \frac{1}{2j}\frac{P}{2}L_{ms}[(\vec{i_s}\vec{i^*_r}e^{-j\epsilon}) - (\vec{i_s}\vec{i^*_r}e^{-j\epsilon})^*] \\ &= \frac{P}{2}L_{ms}\{Im[\vec{i_s}(\vec{i_r}e^{j\epsilon})^*]\} \end{aligned}$$

The stator magnetising inductance, L_{ms} can be related to the three phase magnetising inductance, L_m as $L_m = \frac{3}{2}L_{ms}$. Substituting this value of L_{ms} in the above equation gives the expression for developed electromagnetic torque of the machine as

$$M_d = \frac{2}{3}\frac{P}{2}L_m\{Im[\vec{i_s}(\vec{i_r}e^{j\epsilon})^*]\} \tag{2.27}$$

Here, *Im* represents the imaginary part and * represents the complex conjugate. In this equation, $\vec{i_s}$ is defined in stator coordinates while $\vec{i_r}$ is defined in rotor coordinates.

Alternately, the torque equation can also be derived from the power balace approach as follows. The instantaneous power input to the machine can be written as the sum of the power input to the stator coils and the rotor coils. Thus if P denotes the instantaneous input power,

$$P = \frac{2}{3}Re\{\vec{v_s}\vec{i_s^*} + \vec{v_r}\vec{i_r^*}\} \tag{2.28}$$

where Re denotes the real part of the complex quantity. For a squirrel cage motor, $\vec{v_r} = 0$. Substituting for $\vec{v_s}$ from Eq.(2.20) and evaluating the derivative terms,

$$P = \frac{2}{3}Re\{R_s|\vec{i_s}|^2 + L_s\vec{i_s^*}\frac{d\vec{i_s}}{dt} + L_m\vec{i_s^*}\frac{d\vec{i_r}}{dt}e^{j\epsilon} + jL_m\vec{i_s^*}\vec{i_r}\omega e^{j\epsilon}\} \tag{2.29}$$

Only the terms containing ω contribute to the developed mechanical power. Thus the mechanical power developed, P_d can be written as

$$P_d = \frac{2}{3}Re\{jL_m\vec{i_s^*}\vec{i_r}\omega e^{j\epsilon}\} \tag{2.30}$$

$$= \frac{2}{3}\frac{P}{2}\omega_m Re\{jL_m\vec{i_s^*}\vec{i_r}e^{j\epsilon}\} \tag{2.31}$$

The developed torque can be obtained by dividing the developed mechanical power by the mechanical angular speed. Thus torque equation can be written as

$$M_d = \frac{2}{3}\frac{P}{2}Re\{jL_m\vec{i_s^*}\vec{i_r}e^{j\epsilon}\} = \frac{2}{3}\frac{P}{2}L_m Im\{-\vec{i_s^*}\vec{i_r}e^{j\epsilon}\}$$

The above equation can now be simplified to get the expression for developed torque given by Eq.(2.27) Thus the complete space phasor model of the induction

machine can be given as

$$\begin{aligned}
\vec{v}_s(t) &= R_s\vec{i}_s(t) + L_s\frac{d\vec{i}_s(t)}{dt} + L_m\frac{d}{dt}[\vec{i}_r(t)e^{j\epsilon(t)}] \\
0 &= R_r\vec{i}_r(t) + L_r\frac{d\vec{i}_r(t)}{dt} + L_m\frac{d}{dt}[\vec{i}_s(t)e^{-j\epsilon(t)}] \\
J\frac{d\omega_m}{dt} + B\omega_m &= \frac{2}{3}\frac{P}{2}L_m\{Im[\vec{i}_s(\vec{i}_r e^{j\epsilon(t)})^*]\} - M_{load} \\
\frac{P}{2}\omega_m &= \omega = \frac{d\epsilon(t)}{dt}
\end{aligned} \tag{2.32}$$

where

J - moment of inertia of the rotor

B - frictional loss coefficient

ω_m - speed of rotor in mechanical rad/sec

M_{load} - Mechanical load torque

ω - speed of rotor in electrical rad/sec

Eq.(2.32) defines the behaviour of the machine under transient and steady state conditions. However, it should be noted that, in these equations the stator and rotor space phasors are referred to their respective coordinate axes and not on a common reference frame.

2.4 Dynamics of the Induction Machine in the Rotor Flux reference frame

In this analysis, it will be assumed that the machine is operated from a current source that can impress desired 3-phase currents into the stator windings. Then it is not required to consider the stator equations, as these only serve to determine the stator voltage. The stator voltage dynamics will be considered in detail in section 2.6. Using Eq.(2.21), the rotor equation can be written as

$$R_r\vec{i}_r(t) + (1+\sigma_r)L_m\frac{d\vec{i}_r(t)}{dt} + L_m\frac{d}{dt}[\vec{i}_s(t)e^{-j\epsilon(t)}] = 0 \tag{2.33}$$

where

$\sigma_r = \frac{L_{lr}}{L_m}$ so that $(1+\sigma_r)L_m = L_r$.

The rotor flux space phasor in rotor coordinates is given as

$$\vec{\psi}_r(t) = L_m(1+\sigma_r)\vec{i}_r(t) + L_m\vec{i}_s(t)e^{-j\epsilon(t)} \tag{2.34}$$

The rotor flux space phasor in stator coordinates can be obtained by multiplying with $e^{j\epsilon(t)}$ as

$$\vec{\psi}_r(t)e^{j\epsilon(t)} = L_m[\vec{i}_s(t) + (1+\sigma_r)\vec{i}_r(t)e^{j\epsilon(t)}] = L_m\vec{i}_{mr}(t) \tag{2.35}$$

where

$$\vec{i}_{mr}(t) = \vec{i}_s(t) + (1+\sigma_r)\vec{i}_r(t)e^{j\epsilon(t)} \tag{2.36}$$

Then $\vec{i}_r(t)$ can be written in terms of $\vec{i}_{mr}(t)$ and $\vec{i}_s(t)$ as

$$\vec{i}_r(t) = \frac{\vec{i}_{mr}(t) - \vec{i}_s(t)}{(1+\sigma_r)}e^{-j\epsilon(t)} \tag{2.37}$$

Substituting for $\vec{i}_r(t)$ from Eq.(2.37) in Eq.(2.33) gives

$$\frac{R_r}{(1+\sigma_r)}[\vec{i}_{mr}(t) - \vec{i}_s(t)]e^{-j\epsilon(t)} + L_m\frac{d}{dt}\left[\{\vec{i}_{mr}(t) - \vec{i}_s(t)\}e^{-j\epsilon(t)}\right] + L_m\frac{d}{dt}[\vec{i}_s(t)e^{-j\epsilon(t)}] = 0 \tag{2.38}$$

Evaluating the derivative terms in Eq.(2.38) and simplifying gives

$$\frac{R_r}{(1+\sigma_r)}[\vec{i}_{mr}(t) - \vec{i}_s(t)]e^{-j\epsilon(t)} + [L_m\frac{d\vec{i}_{mr}(t)}{dt} - j\frac{d\epsilon(t)}{dt}\vec{i}_{mr}(t)L_m]e^{-j\epsilon(t)} = 0 \tag{2.39}$$

Note that Eq.(2.39) is still in terms of rotor coordinates. Multiplying by $e^{j\epsilon(t)}$ and recognising that $\frac{d\epsilon(t)}{dt}$ is the same as the speed of the rotor in electrical rad/sec gives the equation in stator coordinates as

$$L_m\frac{d\vec{i}_{mr}(t)}{dt} + \frac{R_r}{(1+\sigma_r)}\vec{i}_{mr}(t) - j\omega L_m\vec{i}_{mr}(t) - \frac{R_r}{(1+\sigma_r)}\vec{i}_s(t) = 0 \tag{2.40}$$

Eq.(2.40) can now be expressed in a reference frame fixed to the rotor flux. The rotor flux magnetising current space vector $\vec{i}_{mr}(t)$ can be written as

$$\vec{i}_{mr}(t) = i_{mr}(t)e^{j\rho(t)} \tag{2.41}$$

where $\rho(t)$denotes the instantaneous position of the rotor flux space vector w.r.t the real axis of the stator. Substituting Eq.(2.41) in Eq.(2.40) gives

$$L_m\frac{d}{dt}[i_{mr}(t)e^{j\rho(t)}] + \frac{R_r}{(1+\sigma_r)}i_{mr}(t)e^{j\rho(t)} - j\omega L_m i_{mr}(t)e^{j\rho(t)} - \frac{R_r}{(1+\sigma_r)}\vec{i}_s(t) = 0 \tag{2.42}$$

Evaluating the derivative terms in Eq.(2.42) and simplifying,

$$[L_m\frac{di_{mr}(t)}{dt} + j(\omega_{mr}-\omega)L_m i_{mr}(t) + \frac{R_r}{1+\sigma_r}i_{mr}(t)]e^{j\rho(t)} = \frac{R_r}{1+\sigma_r}\vec{i}_s(t) \tag{2.43}$$

where $\omega_{mr} = \frac{d\rho(t)}{dt}$ denotes the instantaneous angular speed of rotation of the rotor flux space phasor. Eq.(2.43) is in stator coordintes and can be transformed to rotor flux coordinates by multiplying by $e^{-j\rho(t)}$. This gives

$$L_m\frac{di_{mr}(t)}{dt} + j(\omega_{mr}-\omega)L_m i_{mr}(t) + \frac{R_r}{1+\sigma_r}i_{mr}(t) = \frac{R_r}{1+\sigma_r}i_s(t)e^{-j\rho(t)} \tag{2.44}$$

The right hand side of Eq.(2.44) is the stator current space phasor referred to the rotor flux coordinate system. Let i_{sd} and i_{sq} denote the components of the stator current phasor in the rotor flux coordinates. Then,

$$L_m\frac{di_{mr}(t)}{dt} + j(\omega_{mr}-\omega)L_m i_{mr}(t) + \frac{R_r}{1+\sigma_r}i_{mr}(t) = \frac{R_r}{1+\sigma_r}(i_{sd}(t) + ji_{sq}(t)) \tag{2.45}$$

Separating the real and imaginary parts of Eq.(2.45),

$$\begin{aligned} L_m\tfrac{di_{mr}(t)}{dt} + \tfrac{R_r}{1+\sigma_r}i_{mr}(t) &= \tfrac{R_r}{1+\sigma_r}i_{sd}(t) \\ (\omega_{mr}-\omega)L_m i_{mr}(t) &= \tfrac{R_r}{1+\sigma_r}i_{sq}(t) \end{aligned} \tag{2.46}$$

Defining the rotor time constant, $\tau_r = \frac{L_r}{R_r} = \frac{L_m(1+\sigma_r)}{R_r}$, Eq.(2.46) can be written as

$$\tau_r\frac{di_{mr}(t)}{dt} + i_{mr}(t) = i_{sd}(t) \tag{2.47}$$

$$\omega_{mr}(t) = \frac{d\rho}{dt} = \omega + \omega_{slip} = \omega + \frac{i_{sq}(t)}{\tau_r i_{mr}(t)} \tag{2.48}$$

Eq.(2.47) and Eq.(2.48) represents the dynamics of the machine in the rotor flux frame of reference. An expression for the developed electromagnetic torque of the machine in the rotor flux frame is also required to have a complete machine model.

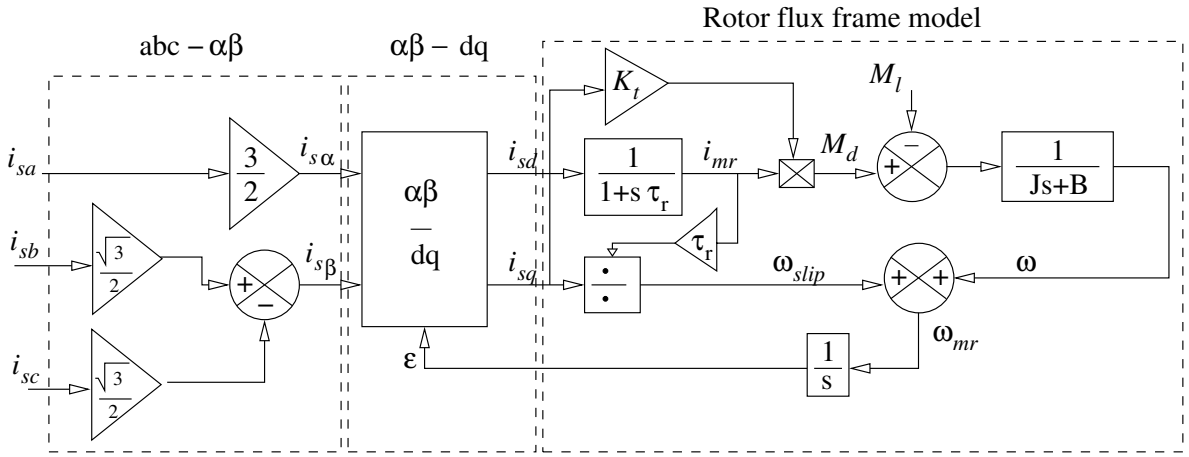

Figure 2.4: Block diagram of current fed induction motor in rotor flux frame

Substituting for $\vec{i}_r(t)$ from Eq.(2.37) into Eq.(2.27),

$$M_d = \frac{2}{3}\frac{P}{2}\frac{L_m}{1+\sigma_r}\{Im[\vec{i}_s(t)(\vec{i}_{mr}(t) - \vec{i}_s(t))^*]\} \tag{2.49}$$

Writing $\vec{i}_s(t)$ as $i_{sd}(t) + ji_{sq}(t)$,

$$M_d = \frac{2}{3}\frac{P}{2}\frac{L_m}{1+\sigma_r} i_{mr}(t) i_{sq}(t) = K_t i_{mr}(t) i_{sq}(t) \tag{2.50}$$

where $K_t = \frac{2}{3}\frac{P}{2}\frac{L_m}{1+\sigma_r}$ is a constant for a machine. Thus Eq.(2.47), (2.48) and (2.50) represents the complete set of dynamic equations of the induction machine in the rotor flux frame of reference.

From these expression, the following points are noted:

1) Steady state value of i_{mr} and i_{sd} is the same. This implies that, if the machine flux remains constant,i_{sd} will also be constant. Also i_{mr} follows i_{sd} in a first order response with a time constant equal to the rotor time constant.

2) The torque equation has the same form as that obtained for a separately excited DC machine. If i_{mr} is kept constant, torque can be controlled by controlling i_{sq} alone. Also the slip at which the machine operates,ω_{slip} is directly proportional to i_{sq} and inversely proportional to i_{mr}.

A block diagram model of the current fed induction motor in the rotor flux reference frame using the equations derived above is shown in Fig. 2.4.

The block diagram model has three sections. In the first section, three phase stator currents are transformed to equivalent two phase quantities. In the second section, the two phase stationary quantities are transformed to the rotating dq reference

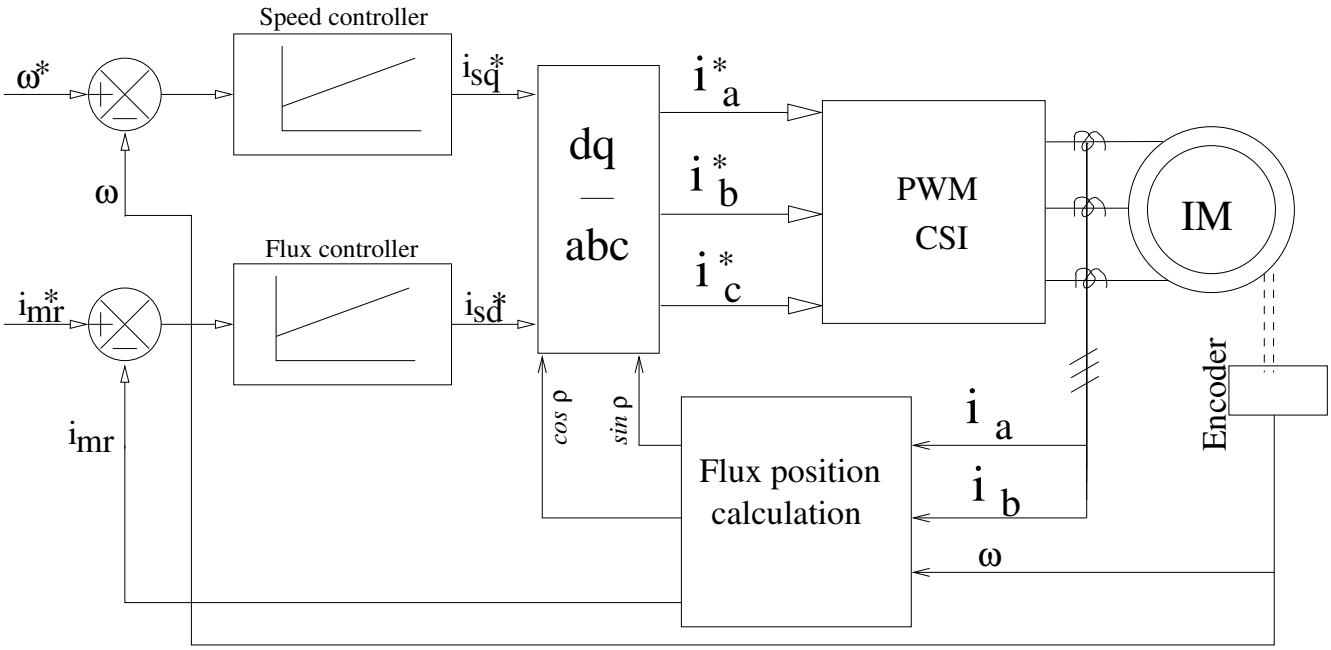

Figure 2.5: Basic Structure of FOC with a Current Source Inverter

frame fixed to the rotor flux space vector. This is done by using the information about the rotor flux position obtained from the machine model to implement the following equations.

$$i_{sd}(t) = i_{s\alpha}(t)\cos\rho(t) + i_{s\beta}(t)\sin\rho(t) \tag{2.51}$$

$$i_{sq}(t) = i_{s\beta}(t)\cos\rho(t) - i_{s\alpha}(t)\sin\rho(t) \tag{2.52}$$

where $\rho(t)$ denotes the instantaneous position of the rotor flux w.r.t the stator axis. The third section implements the dynamic equations of the machine in the dq frame, given by Eq.(2.47), (2.48) and (2.50).

2.5 Field Oriented Control of the Induction Motor

From the preceding discussion it is clear that, in order to achieve decoupled torque and speed control, the current components i_{sd} and i_{sq} needs to be controlled. Therefore, the basic structure of an induction motor drive with Field Oriented Control will be as shown in Fig.2.5

The current references calculated by the drive are translated to three phase reference currents for the PWM Current Source Inverter(CSI). This is done by trans-

forming the references from the rotating dq rotor flux frame to the stationary $\alpha\beta$ frame and then to the three phase stator reference frame. The relevant equations for the transformation are:

$$i^*_{sa} = \frac{2}{3}[i_{sd}\cos\rho(t) - i_{sq}\sin\rho(t)] \quad (2.53)$$

$$i^*_{sb} = -\frac{1}{3}[i_{sd}\cos\rho(t) - i_{sq}\sin\rho(t)] + \frac{1}{\sqrt{3}}[i_{sq}\cos\rho(t) + i_{sd}\sin\rho(t)] \quad (2.54)$$

$$i^*_{sc} = -\frac{1}{3}[i_{sd}\cos\rho(t) - i_{sq}\sin\rho(t)] - \frac{1}{\sqrt{3}}[i_{sq}\cos\rho(t) + i_{sd}\sin\rho(t)] \quad (2.55)$$

Thus if the command references from the controllers are to be properly translated into the reference phase currents for the inverter, an accurate knowledge about the position of the rotor flux is essential.

2.6 Stator dynamics of the induction machine in the rotor flux frame

In the previous discussion, it was assumed that the stator windings were impressed with the desired currents using the inverter. This could be done using a current source inverter. However at high speeds, the assumption of a constant current may not be valid when the inverter dc bus cannot force current against the back emf of the machine. Also, when voltage source inverters are used, the stator voltage dynamics needs to be considered. So now, the necessary equations representing the stator voltage dynamics in the rotor flux frame will be obtained.
The stator voltage equation from Eq.(2.32) is given as

$$\vec{v}_s(t) = R_s\vec{i}_s(t) + L_s\frac{d\vec{i}_s(t)}{dt} + L_m\frac{d}{dt}[\vec{i}_r(t)e^{j\epsilon(t)}] \quad (2.56)$$

Substituting for $\vec{i}_r(t)$ from Eq.(2.37) into Eq.(2.56),

$$\vec{v}_s(t) = R_s\vec{i}_s(t) + L_s\frac{d\vec{i}_s(t)}{dt} + \frac{L_m}{1+\sigma_r}\frac{d}{dt}[\vec{i}_{mr}(t) - \vec{i}_s(t)] \quad (2.57)$$

In the above equation, $\vec{i}_s(t)$, $\vec{v}_s(t)$ and $\vec{i}_{mr}(t)$ are in the stator coordinates. Multiplying $\vec{v}_s(t)$ by $e^{-j\rho(t)}$ transforms it to the rotor coordinates. The superscript r

will be used to denote quantities in the rotor flux frame. Thus the equations in the rotor coordinates can be written as,

$$\vec{v_s}(t)e^{-j\rho(t)} = \vec{v_s^r}(t) = v_{sd(t)} + jv_{sq(t)} \tag{2.58}$$

$$\vec{i_s}(t) = \vec{i_s^r}(t)e^{j\rho(t)} = [i_{sd}(t) + ji_{sq}(t)]e^{j\rho(t)} \tag{2.59}$$

Thus by multiplying Eq.(2.57) throughout by $e^{-j\rho(t)}$ gives

$$\begin{aligned} \vec{v_s^r}(t) &= R_s\vec{i_s^r}(t) + L_s\frac{d}{dt}[\vec{i_s^r}(t)e^{j\rho(t)}]e^{-j\rho(t)} + \frac{L_m}{1+\sigma_r}\frac{d}{dt}[\vec{i}_{mr}(t) - \vec{i_s^r}(t)e^{j\rho(t)}]e^{-j\rho(t)} \\ &= R_s(i_{sd}(t) + ji_{sq}(t)) + L_s\frac{d}{dt}[(i_{sd}(t) + ji_{sq}(t)e^{j\rho(t)}]e^{-j\rho(t)} \\ &+ \frac{L_m}{1+\sigma_r}\frac{d}{dt}[(i_{mr}(t) - i_{sd}(t) - ji_{sq}(t))e^{j\rho(t)}]e^{-j\rho(t)} \end{aligned} \tag{2.60}$$

Noting that all voltages and currents in the above equations are functions of time, the suffix *(t)* can be dropped. Evaluating the derivative terms and substituting $\frac{d\rho(t)}{dt} = \omega_{mr}$ gives

$$\begin{aligned} v_{sd} + jv_{sq} &= R_s(i_{sd} + ji_{sq}) + L_s\Big[\Big(\frac{di_{sd}}{dt} + j\frac{di_{sq}}{dt}\Big) + ji_{sd}\omega_{mr} - i_{sq}\omega_{mr}\Big] + \frac{L_m}{1+\sigma_r} \\ &\Big[\frac{d}{dt}(i_{mr} - i_{sd}) - j\frac{di_{sq}}{dt} + j\omega_{mr}(i_{mr} - i_{sd}) + i_{sq}\omega_{mr}\Big] \end{aligned} \tag{2.61}$$

Separating out the real and imaginary terms and simplifying,

$$v_{sd} = R_si_{sd} + \sigma L_s\frac{di_{sd}}{dt} - \sigma L_si_{sq}\omega_{mr} + (1-\sigma)L_s\frac{di_{mr}}{dt} \tag{2.62}$$

$$v_{sq} = R_si_{sq} + \sigma L_s\frac{di_{sq}}{dt} + \sigma L_si_{sd}\omega_{mr} + (1-\sigma)L_s\omega_{mr}i_{mr} \tag{2.63}$$

where $\sigma = 1 - \frac{L_m^2}{L_sL_r}$ is called the leakage factor.

Eq.(2.62) and Eq.(2.63) are the required expressions that represent the stator voltage dynamics of the machine in the rotor flux frame. These can now be used to calculate the required values of the d and q axis stator voltages which are then realised using a pulse width modulated Voltage Source Inverter(VSI). Feed forward can be used to improve the response of the d and q axis currents to the

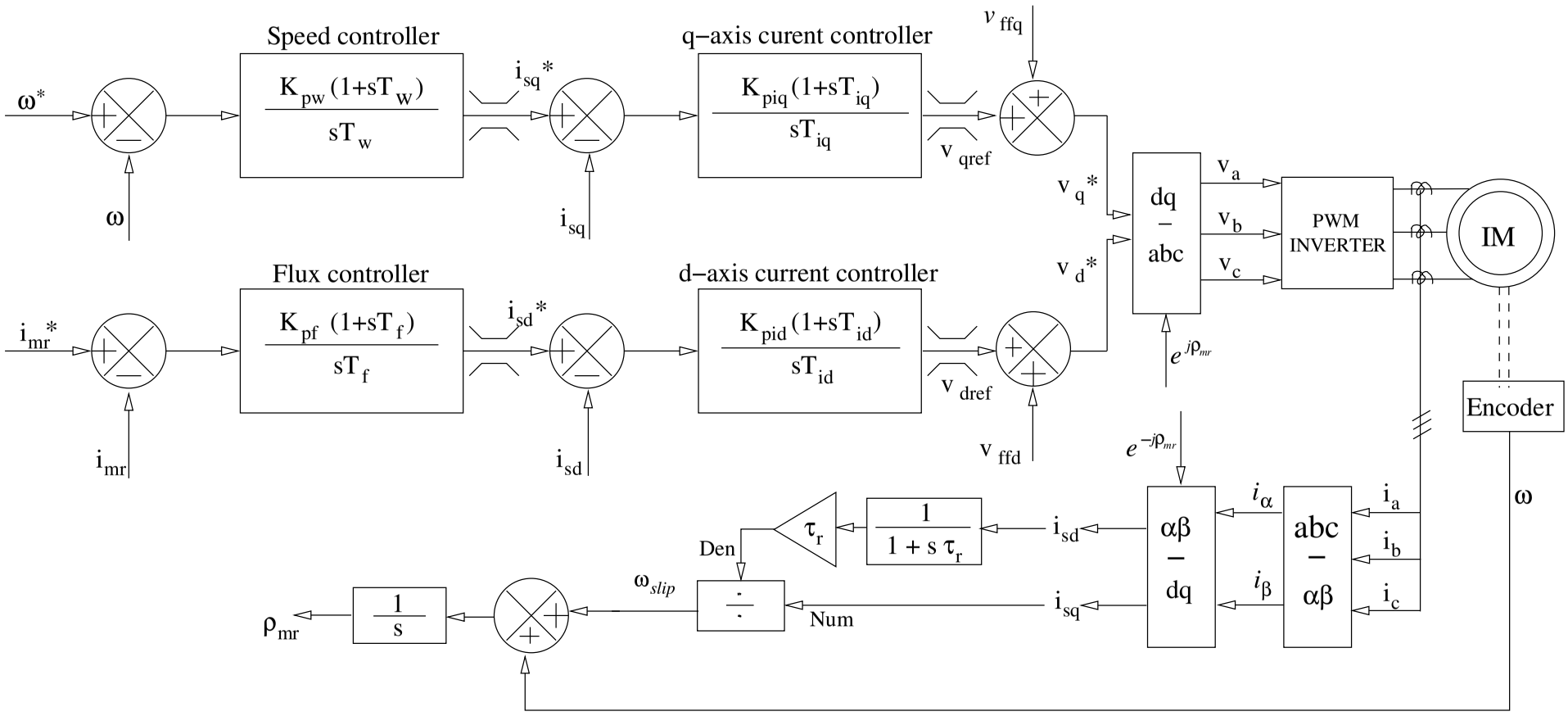

Figure 2.6: Block diagram for sensored vector control

respective voltages. The feed forward terms are given as,

$$v_{ffd} = -\sigma L_s i_{sq} \omega_{mr} + (1-\sigma) L_s \frac{di_{mr}}{dt} \tag{2.64}$$

$$v_{ffq} = \sigma L_s i_{sd} \omega_{mr} + (1-\sigma) L_s \omega_{mr} i_{mr} \tag{2.65}$$

where v_{ffd} denotes the d-axis feed forward term and v_{ffq} denotes the q-axis feed forward term. The addition of these terms to the ouput of the d axis and q axis current controllers respectively gives a first order response of the dq axis currents to the respective dq axis voltages. The complete block diagram for the VSI fed, vector controlled induction motor drive is shown in Fig. 2.6.

2.7 Speed and Flux estimation for Sensorless FOC

It is clear from the preceding discussion that accurate information about the rotor flux position is critical for proper decoupled control. Also speed control of the drive requires a feedback of the instantaneous speed of the rotor. In a typical sensored FOC scheme, an encoder is used to obtain these informations. However, the use of an encoder has certain drawbacks as mentioned in Chapter 1. Hence a sensorless scheme is preferred. In a sensorless FOC scheme, the speed and the flux position needs to be estimated. The dynamic performance of the sensorless vector controlled drive depends on the accuracy of the estimators.

The most basic approach towards estimating the rotor flux is by integrating the stator voltage to estimate the stator flux and then calculating the rotor flux from the stator flux. From the equivalent circuit in Fig. 2.7, the stator voltage can be written as

$$\vec{v_s} = R_s \vec{i_s} + \frac{d\vec{\psi_s}}{dt} \tag{2.66}$$

Therefore the stator flux space vector can be obtained by simply integrating the backemf. This is represented as

$$\vec{\psi_s} = \int (\vec{v_s} - R_s \vec{i_s}) dt \tag{2.67}$$

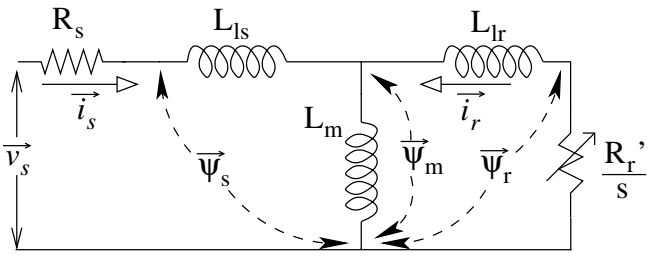

Figure 2.7: Equivalent circuit showing various fluxes

Also from the equivalent circuit,

$$\vec{\psi_s} = L_s\vec{i_s} + L_m\vec{i_r} \tag{2.68}$$

$$\vec{\psi_r} = L_r\vec{i_r} + L_m\vec{i_s} \tag{2.69}$$

Therefore, substituting for $\vec{i_r}$ from Eq. (2.68) into Eq. (2.69),

$$\vec{\psi_r} = \frac{L_r}{L_m}\vec{\psi_s} - \frac{L_sL_r - L_m^2}{L_m}\vec{i_s} \tag{2.70}$$

Eq. (2.70) can be written in terms of their $\alpha\beta$ components as

$$\vec{\psi_{r\alpha}} = \frac{L_r}{L_m}\vec{\psi_{s\alpha}} - \frac{L_sL_r - L_m^2}{L_m}\vec{i}_{s\alpha} \tag{2.71}$$

$$\vec{\psi_{r\beta}} = \frac{L_r}{L_m}\vec{\psi_{s\beta}} - \frac{L_sL_r - L_m^2}{L_m}\vec{i}_{s\beta} \tag{2.72}$$

Knowing the α and β components of the rotor flux, the instantaneous angular position $\rho(t)$ and the flux speed ω_{mr} can be estimated as

$$\rho(t) = \tan^{-1}\left(\frac{\psi_{r\beta}}{\psi_{r\alpha}}\right) \tag{2.73}$$

$$\omega_{mr} = \frac{d\rho(t)}{dt} \tag{2.74}$$

The actual rotor speed can now be estimated by using Eq.(2.48). A block diagram of the basic structure of the estimator is shown in Fig.2.9. A complete block diagram of the VSI fed, sensorless vector controlled drive is shown in Fig.2.8.

Although the structure of the estimator looks relatively simple, there are some problems associated with a practical implementation. Any practical implementation of an integrator will have some offset at the input which causes the output

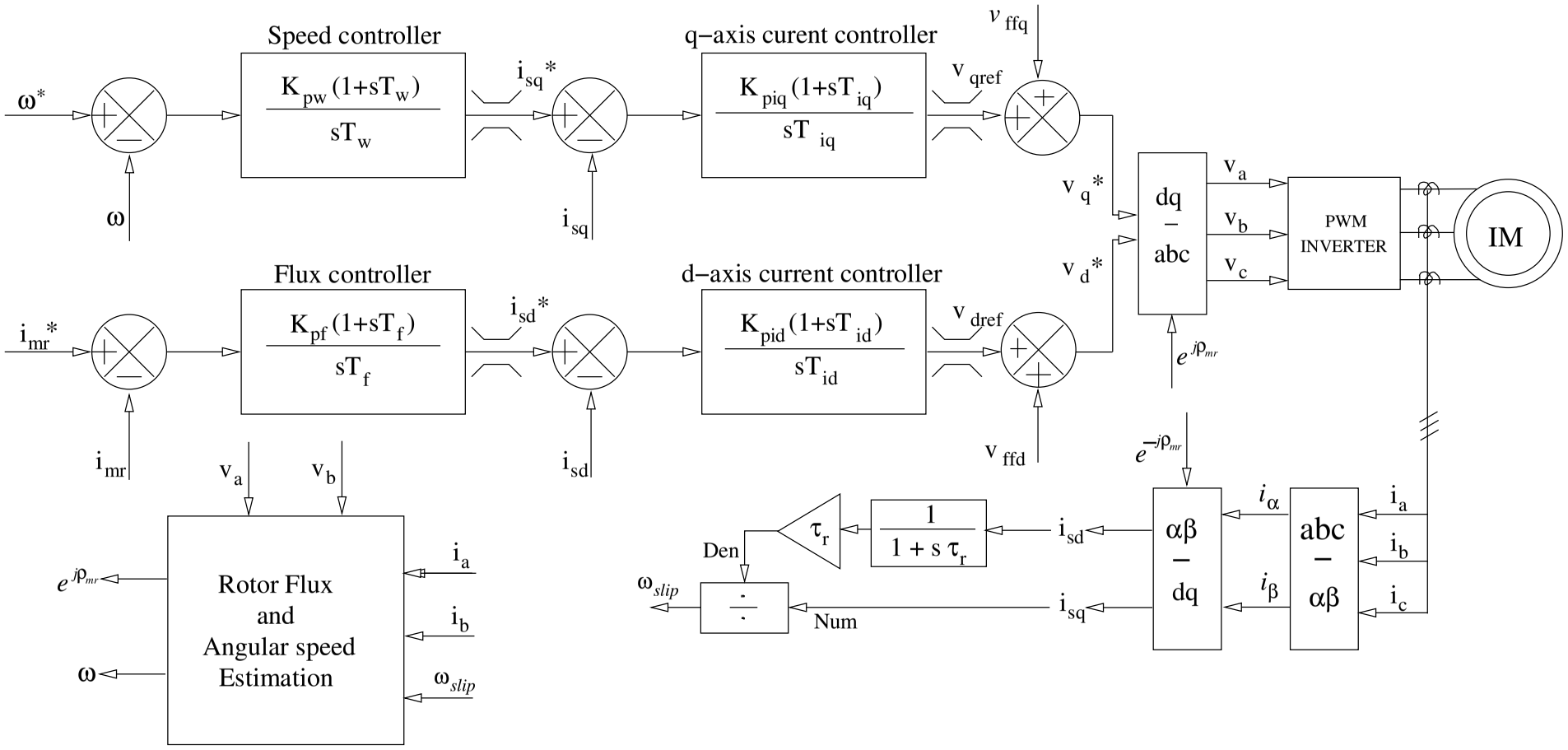

Figure 2.8: Block diagram for sensorless vector control

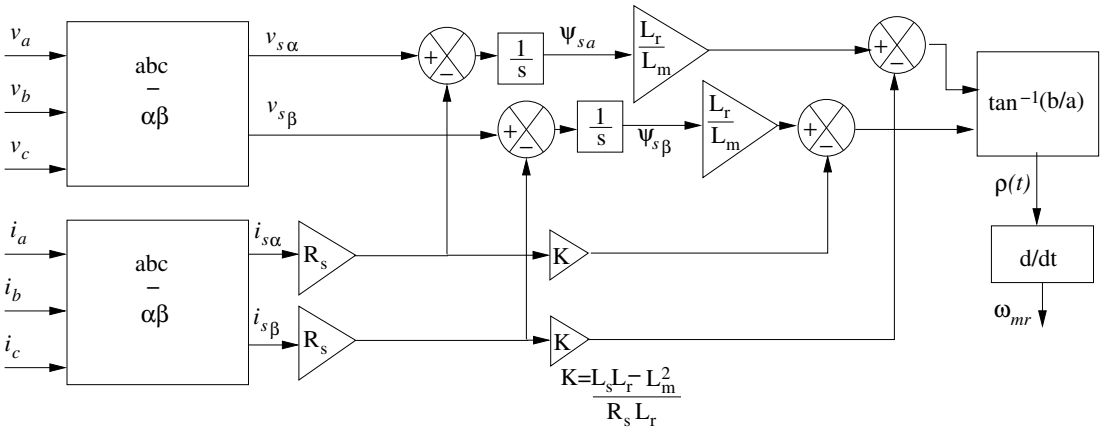

Figure 2.9: Block diagram for a basic flux estimator

to drift away with time. This problem is mitigated to some extent by using a low pass filter with a very low cutoff frequency, instead of a pure integrator. This scheme works well at high speeds, but at low speeds the low pass filter causes significant phase and magnitude errors. Also if there is a slight error in the stator resistance value used in the estimator, then at low frequencies the error in estimated resistive drop becomes comparable to the voltage applied to the motor. This causes significant errors in the estimated flux magnitude and position at low frequencies. Also a direct differentiation of the estimated angle causes large spikes in the estimated speed due to the presence of noise in the estimated value. Thus the basic estimator scheme needs to be modified to achieve good performance over a wide speed range. Two schemes for flux estimation that have been tested in this project will be described in the following subsections.

2.7.1 Flux estimation scheme-I

In flux estimation scheme-I[11], the pure integrator is replaced by an integrator with a small amount of negative feedback. Without any negative feedback, the flux estimate obtained from Eq.(2.67) by a using pure integrator can be destabilised due to a variety of errors that may become particularly detrimental at low stator frequencies. These include measurement noise, parameter detuning and input dc offsets. The effect of the feedback is to stabilise the integrator output against these errors, particularly the DC offset errors which can lead to integrator saturation. The structure of the modified integrator with negative feedback used in the flux

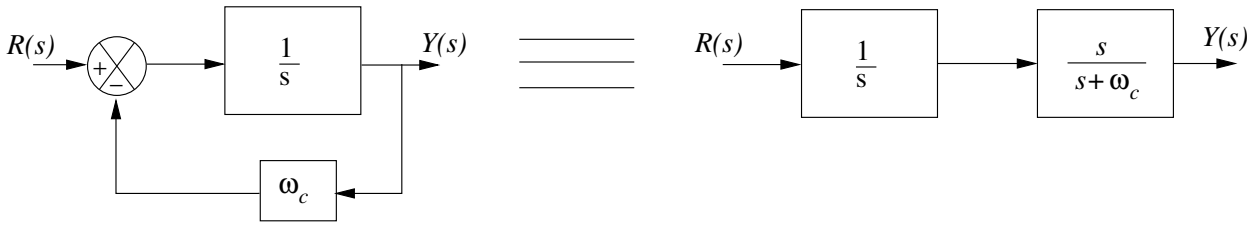

Figure 2.10: Modified Integrator with feedback

estimation scheme-I is as shown in Fig.2.10 The modified scheme can be shown to be essentially equivalent to a pure integrator followed by a high pass filter. The structure thus has a low pass filter characteristic with the pole close to zero. The transfer function is given as

$$H(s) = \frac{Y(s)}{R(s)} = \frac{1}{s + \omega_c}$$

The feedback gain ω_c turns out to be the cutoff frequency of the high pass filter after the integrator. This should be chosen low enough to provide good integration stability and low speed performance. This scheme provides good accuracy and integration stability for speeds from rated and down to about 3 Hz stator frequency. Below 3 Hz, the phase and magnitude errors introduced by the low pass filter becomes significant and degrades the performance.

2.7.2 Flux estimation scheme-II

Flux estimation scheme-II[17] uses an error correction scheme to continuously correct the error in estimation. In the previous discussion, it was found that a small amount of negative feedback is required for the integrator to stabilise the integration against dc offsets. However this feedback gives the estimator a low pass filter characteristic. This means that there will be a considerable phase and magnitude error in the integrator output at frequencies close to the corner frequency, thus degrading the low speed performance of the drive.

Estimation scheme-II overcomes the problem of the steady state phase and magnitude errors by using a feedback mechanism that provides integration stability similar to that of a Low Pass Filter(LPF), and at the same time compensate for

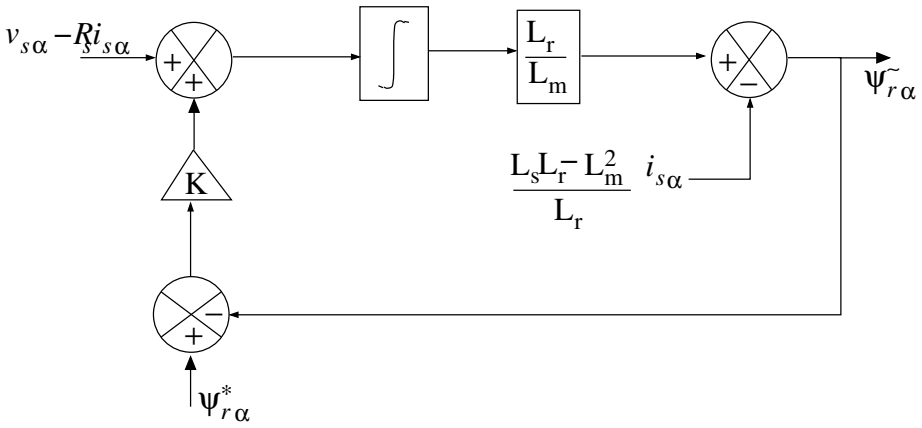

Figure 2.11: Flux Estimation Scheme-II

phase and magnitude errors. This is done by using another source of estimated flux magnitude to identify and compensate for drift occuring at the integrator output. The structure of such a flux estimation scheme is given in Fig 2.11.

From the output of the estimator, the angle can be calculated as

$$\cos\rho^{\sim} = \frac{\psi_{r\alpha}^{\sim}}{\sqrt{(\psi_{r\alpha}^{\sim})^2 + (\psi_{r\beta}^{\sim})^2}} \tag{2.75}$$

$$\sin\rho^{\sim} = \frac{\psi_{r\beta}^{\sim}}{\sqrt{(\psi_{r\alpha}^{\sim})^2 + (\psi_{r\beta}^{\sim})^2}} \tag{2.76}$$

Now the values of $\psi_{r\alpha}^{*}$ and $\psi_{r\beta}^{*}$ needs to be calculated for the error correcting feedback. These are obtained as $\psi_{r\alpha}^{*} = \psi_r^{*}\cos\rho^{\sim}$ and $\psi_{r\beta}^{*} = \psi_r^{*}\sin\rho^{\sim}$, so the issue is to obtain the value of ψ_r^{*}. Utilising the steady state equations of the rotor current model of the induction motor, and noting that the rotor flux phasor and the rotor current phasor are orthogonal to each other at steady state, an estimate of the magnitude of the rotor flux, $|\psi_r^{*}|$ can be obtained as

$$|\psi_r^{*}| = \sqrt{L_m(i_{s\alpha}\psi_{r\alpha}^{\sim} + i_{s\beta}\psi_{r\beta}^{\sim})} \tag{2.77}$$

Thus the final equations to be implemented for flux estimation are given as:

$$\psi_{r\alpha}^{\sim} = \frac{L_r}{L_m}\int\Big[(v_{s\alpha} - R_s i_{s\alpha}) + K(\psi_{r\alpha}^{\sim} - \psi_{r\alpha}^{*})\Big]dt - \frac{L_s L_r - L_m^2}{L_m} i_{s\alpha} \tag{2.78}$$

$$\psi_{r\beta}^{\sim} = \frac{L_r}{L_m}\int\Big[(v_{s\beta} - R_s i_{s\beta}) + K(\psi_{r\beta}^{\sim} - \psi_{r\beta}^{*})\Big]dt - \frac{L_s L_r - L_m^2}{L_m} i_{s\beta} \tag{2.79}$$

Here K is the correction gain. At steady state, $\psi_{r\alpha}^{\sim} - \psi_{r\alpha}^{*} = 0$, and the integrator is a pure integrator. However, during transients and disturbances, there exists an error between the * variable and the $\sim$ variable. This brings the error decay mechanism into play. Thus this scheme provides good integration stability similar to a low pass filter and at the same time, avoids the problems due to magnitude and phase errors at low frequency operation.

However, a minor disadvantage of this scheme is that the esimtated magnitude of flux, $|\psi_r^*|$ is dependent on the value of machine parameter L_m. Thus an error in estimating L_m will lead to a steady state error between the * variable and the $\sim$ variable. This can cause an error in the estimated flux position. Thus the value of L_m needs to be known accurately.

2.7.3 Speed estimation scheme

The information about the instantaneous speed of the machine is essential for doing speed control. In sensorless vector control, the speed is estimated using the dynamic model equations of the induction machine in the rotor flux frame of reference. The synchronous speed, ω_{mr} is estimated from the estimated values of $\sin\rho$ and $\cos\rho$ obtained from the flux estimation scheme, thereby avoiding the need for an inverse tan operation and direct differentiation of the angle $\rho(t)$. The actual speed is then calculated from the current model using Eq. Eq.(2.48). The

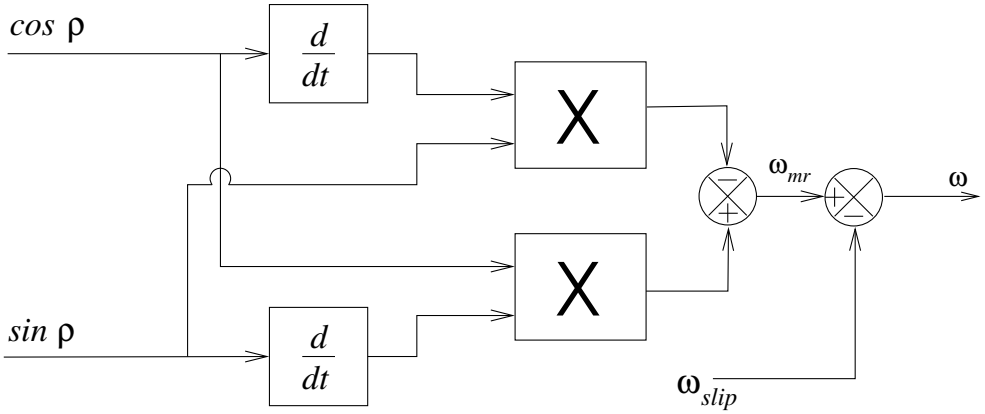

Figure 2.12: Block diagram of the speed estimator

relevant equations are given as,

$$\begin{aligned}\omega_{mr} &= \frac{d\rho}{dt} = \frac{d\rho}{dt}[\cos^2\rho + \sin^2\rho] \\ &= \cos\rho\Big(\cos\rho\frac{d\rho}{dt}\Big) + \sin\rho\Big(\sin\rho\frac{d\rho}{dt}\Big) \qquad (2.80) \\ &= \cos\rho\frac{d}{dt}[\sin\rho] - \sin\rho\frac{d}{dt}[\cos\rho] \qquad (2.81)\end{aligned}$$

Then the rotor speed in electrical rad/sec is given as

$$\omega = \omega_{mr} - \omega slip = \omega mr - \frac{isq}{\tau_r i_{mr}} \qquad (2.82)$$

The block diagram of the speed estimator is as shown in Fig.2.12. It should be noted that the speed estimation still involves a digital differentiation of the quantities, $\sin\rho$ and $\cos\rho$. Thus it may be required to filter the estimated values of $\sin\rho$ and $\cos\rho$ using low pass filters of appropriate cut off frequency so as to reduce the effect of differentiating the noise. Also the estimated speed might need low pass filtering before giving it as a speed feedback, depending on the bandwidth of the speed controller. In this project, digital filters of cutoff frequency 500 Hz were used for filtering the estimated values of $\sin\rho$ and $\cos\rho$ and 5 Hz for filtering the estimated speed.

2.8 Ride-through and On-the-fly starting

AC drives have been very widely used in the industry in crucial production process applications. Interruptions in such critical industrial processes can result in significant loss in revenue and costly downtimes. For example, in continuous process systems like paper machines, winders etc., any interruptions can halt the entire manufacturing flow, with extremely costly implications. Thus the drives are required to run smoothly inspite of momentary power interruptions or voltage dips. Also, the drive should be able to continue operation when the supply is restored. This feature of the drive is known as ride-through with 'on-the-fly' capability.

When the drive is in operation, there is some amount of energy stored in the DC link capacitor and some mechanical energy stored in the inertia of the drive.

When a supply interruption occurs, this stored energy is used up in supplying the losses as well as the load torque. The major losses that occur in the machine are the mechanical losses consisting of the friction and windage losses, and the electromagnetic losses consisting of the core loss, hysteresis loss and the conduction loss. Apart from these losses the switching of the IGBT's in the inverter also cause losses in the system. Thus when a supply interruption occurs, the speed of the motor as well as the DC capacitor voltage starts decreasing. The rate of drop of speed depends on the amount of loss occuring.

An important factor that needs to be considered in the implementation of a ride through scheme is the effect of the precharge circuit. This ciruit is used to prevent large inrush currents from flowing into the capacitor and causing damage. For the drive configuration used in this work, the precharge circuit consists of a current limiting resistor with a bypass relay, connected in series with the capacitor charging path. The resistance is bypassed when the capacitor voltage exceeds the under voltage limit. It again comes back to circuit when the voltage falls back to below the under-voltage limit. With this method of precharging, the inverter cannot supply any output power, when the charging resistor is in the circuit. Thus the time of ride through should be such that the DC bus voltage does not go below the under-voltage limits.

In this project, a simple method for a ride-through scheme is implemented by switching off the gate pulses to the inverter upon sensing a power interruption. The power interruption is sensed by sensing the line voltages at the input side of the rectifier using Hall effect voltage sesors. Thus all the mechanical losses and the load torque, during the period of interruption will be supplied only by the stored energy in the inertia of the shaft. In this way, the DC bus capacitor voltage can maintain its value during the period of power interruption and the drive can therefore start on-the-fly when supply is restored.

2.9 Dead time compensation for the inverter

The switches used in the inverter are IGBT's that have a finite turn on and turn off time. Due to this a set of complementary pulses applied to the switches on the

same leg will result in both the switches conducting for a short period of time. Such a condition is to be avoided as it will short circuit the DC bus. Therefore a finite time is usually provided between the turn off pulse for a switch and the turn on pulse for the other switch. This time delay given for the rising edge of the switching pulse is called the dead time. The effect of the dead time is to cause a drop in the fundamental output voltage of the inverter and an increase in the lower order harmonics, as compared to the ideal operation without dead time. Thus a technique which can compensate for these effects of the dead time can improve the performance of the drive.

In this project, a reference wave modification technique[20] for compensating the dead time effect has been studied. In this scheme the, compensation of dead time is simply achieved by modifying the reference wave according to the direction of the load current. The average voltage deviation in the pole voltage,ΔV due to dead time effect over a half cycle can be given as

$$\Delta V = MV_d\frac{T_d}{T} \tag{2.83}$$

where

M - number of switchings per cycle.

V_d - DC link voltage.

T_d - dead time in seconds.

T - length of a cycle.

This deviation in pole voltage of a phase occurs in such a manner as to reduce the voltage if the load current is positive and increase the voltage if the load current is negative. Thus the effect of the dead time can be nullified by adding a square wave of magnitude equal to ΔV with a suitable polarity. This means that the reference is to be made more positive when when current flows towards the motor and more negative when current flows away from the motor. Since the magnitude of V_d is fixed for a fixed value of the dead time and switching frequency, the effect of this deadband becomes predominant at low frequencies of drive operation when the phase voltage is also low. The simulated waveforms of the reference and the phase current for the 1 MW, sensored vector controlled drive with a dead time of 4 μs at a low speed operation of 3 Hz is shown in Fig.2.13.

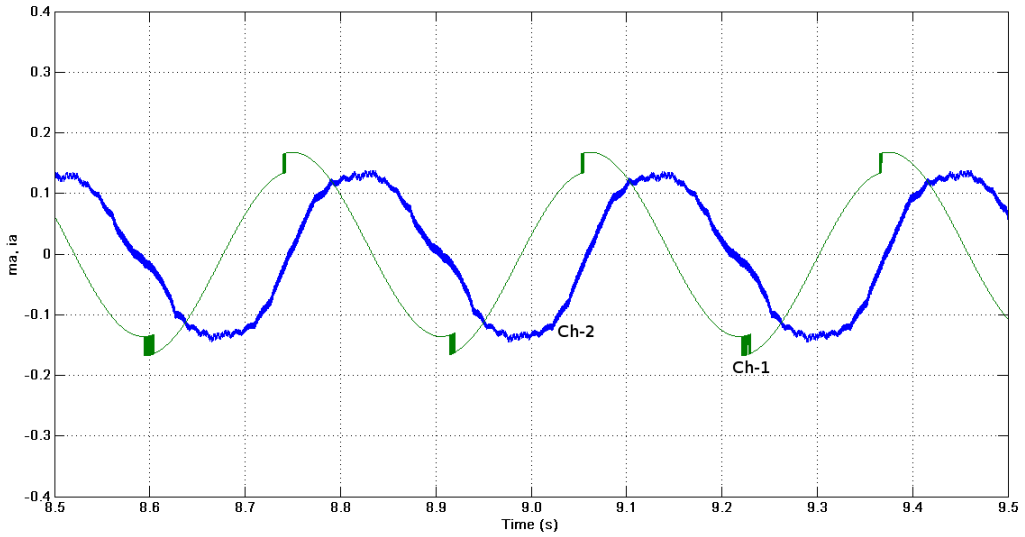

Figure 2.13: Simulated waveforms of R-phase modulating waveforms and R-phase current for low speed operation of 3 Hz with a deadtime of 4μs. *(Ch1- R-phase modulating waveform, Ch2- R-phase current waveform Scale: X-axis: 100 ms/div, Y-axis: Ch1- 0.1/div, Ch2- 300A/div)*

This method of compensating the reference has a slight disadvantage that the range of linear modulation gets reduced due to the increase in the peak value of the reference wave. However, it is a very simple method that can give a good performance in compensating the dead time effects.

2.10 Conclusion

This chapter introduced the concept of space phasors and derived the dynamic equations of the space phasor model of the induction machine. The basic ideas of vector control were discussed and the complete control block diagram for vector control was presented. The idea of flux estimation using the voltage model for sensorless control was discussed along with two such estimation algorithms that are used in this project. The hardware setup for the implementation will be discussed in the next chapter.

CHAPTER 3

HARDWARE ORGANISATION FOR VECTOR CONTROL IMPLEMENTATION

3.1 Introduction

The Field Oriented Control scheme for an induction machine is a computationally intensive scheme involving large number of multiplication, division and trigonometric operations. An analog implementation using multipliers, function generators etc becomes too expensive and lacks flexibility of control. Therefore, a digital implementation is the only practical and feasible approach. Moreover, digital implemenation has the advantages of having standardised harware and complete flexibility in parameter selection and control.

In this project work, vector control has been implemented on a TMS320F28335, 32-bit floating point Digital Signal Controller from Texas Instruments. In this chapter, the features of this processor and the various peripheral capabilities that help in implementing vector control will be explained. The additional circuitry developed for proper interfacing and protection will also be discussed.

3.2 Brief Overview of the TMS320F28335

The computing unit of the TMS320F28335 is a 32-bit DSP core with a modified Harvard architecture, and also includes a single precision IEEE 754 floating point unit(FPU) and a 32x32 hardware multiplier. The FPU enables floating point computations to be performed in hardware. It also has an 8 stage protected pipeline with pipelined memory access. The memory bus architecture has a program read bus, data read bus and data write bus. The on-chip physical memory consists of a $34K$x16 SARAM, $256K$x16 FLASH, $8K$x16 ROM, $1K$x16 OTP and the registers.

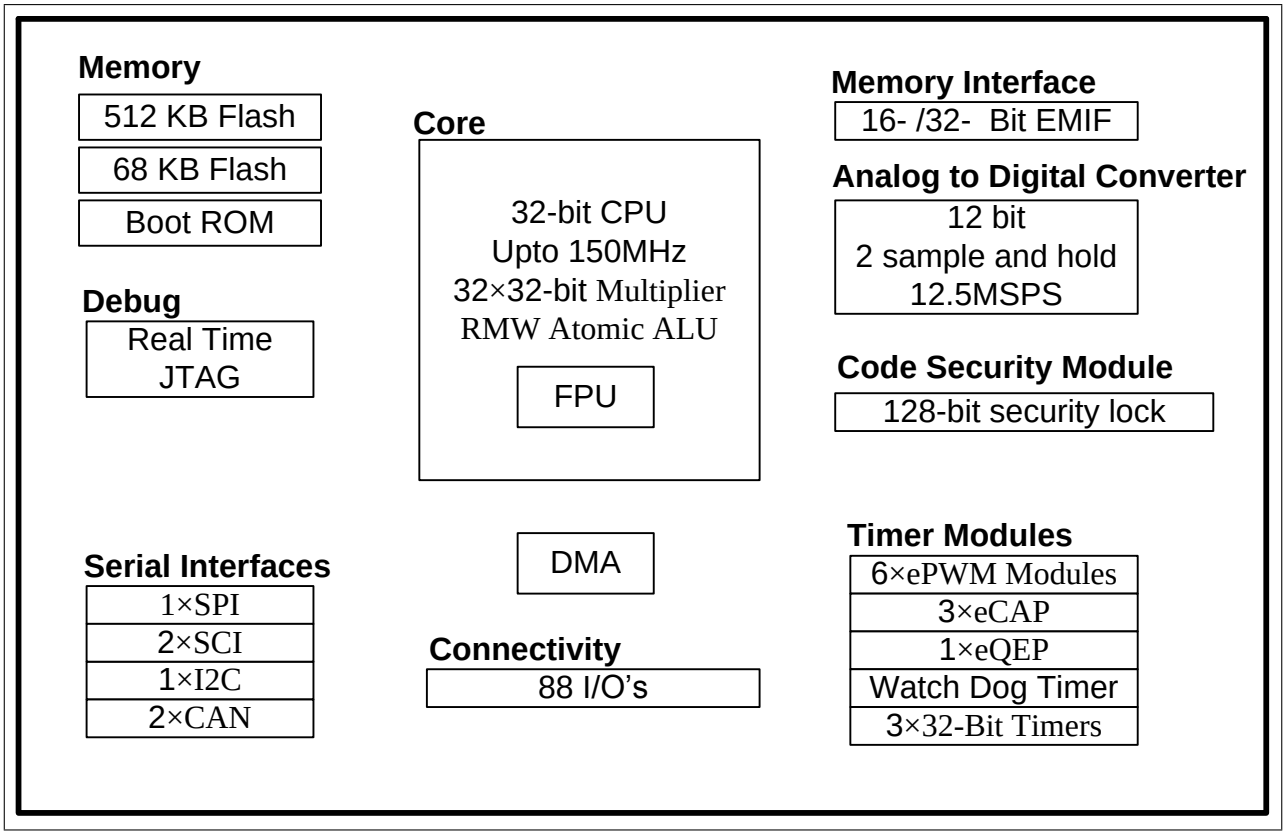

Figure 3.1: Block diagram of the TMS320F28335.

The ROM comes preprogrammed with bootloading software from the manufacturer. The device has an on-chip oscillator with a PLL for clock scaling. It also has 88 GPIO pins multiplexed with a variety of other peripherals like PWM, capture unit, Quadrature Encoder Interface, ADC etc. The controller also has standard communication interfaces like SCI, SPI, I^2C and CAN that enables it to connect with other slave devices. 96 external interrupts are supported, which are governed by the Peripheral Interrupt Expansion(PIE) unit. The DMA bus allows data to be transferred from one part of the DSP to another without intervention by the CPU. The real-time JTAG interface helps in real-time debugging and along with the Code Composer Studio(CCS) from TI is an invaluable tool during the development stage. Fig. 3.1 shows a block diagram of the TMS320F28335 controller with all peripherals.

In this project, a Peripheral Explorer Kit(PEK) and the 28335 control card available from Texas Instruments has been used. The PEK is a development platform for the TMS320F28335 with all the peripherals brought out onto pin

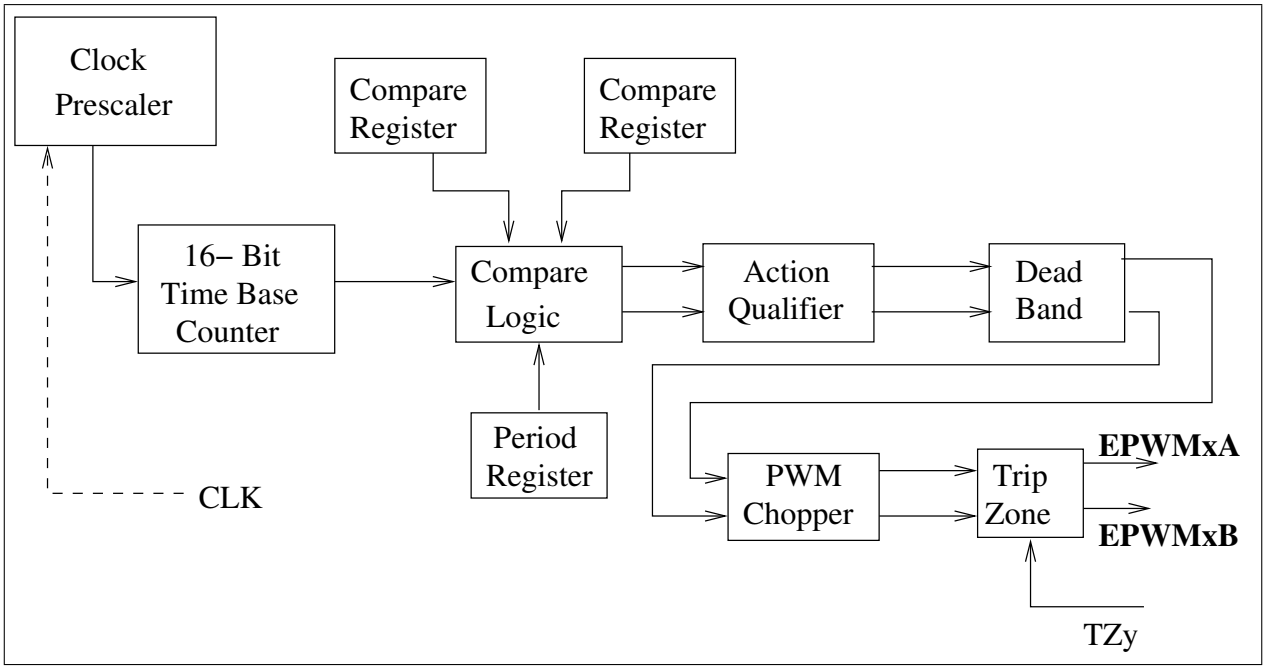

Figure 3.2: ePWM Block diagram

headers. In the next sections, the following peripherals of the DSC which are used for implementing the vector control algorithm will be discussed:

a) ePWM module

b) ADC module

c) Capture module

3.3 ePWM Module

The TMS320F28335 has six enhanced PWM modules[21] included. These are called 'enhanced' since they can generate complex PWM waveforms with minimum CPU intervention. Each ePWMx module has two output channels: ePWMxA and ePWMxB. Each PWM modules has seven submodules that perform various functions in generating the PWM waveforms. The structure of a single ePWM module is shown in Fig. 3.2. All the submodules except the PWM chopper have been used in this project and will be discussed in the following sections.

3.3.1 Time base submodule

The function of the time base module is to generate the high frequency triangular carrier signal for PWM. It consists of a clock prescaler, a 16 bit time base counter and a 16 bit period register. In this project, a 30MHz crystal oscillator has been used and the PLL is configured such that the core runs at a frequency of 150MHz. This clock signal forms the input to the time base module.

The clock prescaler is used to reduce the incoming frequency to a desired value. The time base counter is a 16 bit timer with the prescaler output as its clock signal.The period register defines the length of a period of the counter output in multiples of the time period of the prescaler output. The timer can be configured to run in either up, down or up-down mode. The up mode and down mode produces asymmetric sawtooth waveform while the up-down mode produces a symmetrical triangular waveform. In this project, the counter has been set up to operate in the up-down mode to generate a triangular carrier waveform of 2kHz frequency.

3.3.2 Counter compare submodule

The state of the output PWMs are determined by comparing the high frequency carrier signal with a modulating wave. In the ePWM module, this is done by comparing the timer output from the time base modules with the values in the compare registers. The job of the Counter compare(CC) module is to generate events by comparison. The action qualifier unit, discussed in the next section, then takes actions predefined for each of these events. The CC submodule has two registers: CMPA and CMPB which stores the values that are compared with the time base counter to generate the events.

3.3.3 Action Qualifier submodule

The action qualifier decides the action to be taken upon recieving the events from the previous modules. The fucntionality is based on two registers,AQCTLA and AQCTLB for the two channels of the PWM unit. For each event occuring, the

corresponding line can be set high or set low or toggled or no action taken. It also features a software force option, which allows the programmer to set these lines to a certain level by executing a software instruction. In this project, the action qualifier module is configured so as to produce complementary signals on the two channels.

3.3.4 Dead band submodule

The purpose of the Dead band submodule is to provide a required delay between the falling edge on one channel and the rising edge on the other channel of an ePWM. This required to prevent shoot through in the inverter. The hardware dead band module on the ePWM units can act to provide either a rising edge delay or a falling edge delay. In this project, a Protection and Delay card has been used for interfacing to the inverter, which provides a hardware delay of $2\mu s$. Additionally, however the dead band module is also used to provide a delay time of $2\mu s$.

3.3.5 Event Trigger submodule

The event trigger(ET) submodule can be used to request interrupts or take some action on the occurence of a compare or timebase event. In this project it has been used to trigger the starting of ADC conversion. If the ADC samples a current waveform at the instant of switching, it can cause aliasing due to current ripple. If the inverter modulating signal is limited to the linear modulation range, the compare register value will always be greater than zero and there will be no switching at the instant when the counter is zero. So the ET module is configured to request the ADC to start conversion on the occurence of a 'timer counter equals zero' event.

3.3.6 Trip zone submodule

Each ePWM module is connected to six trip zone signals that are multiplexed with GPIOs. These are used to indicate external fault or trip conditions and the trip

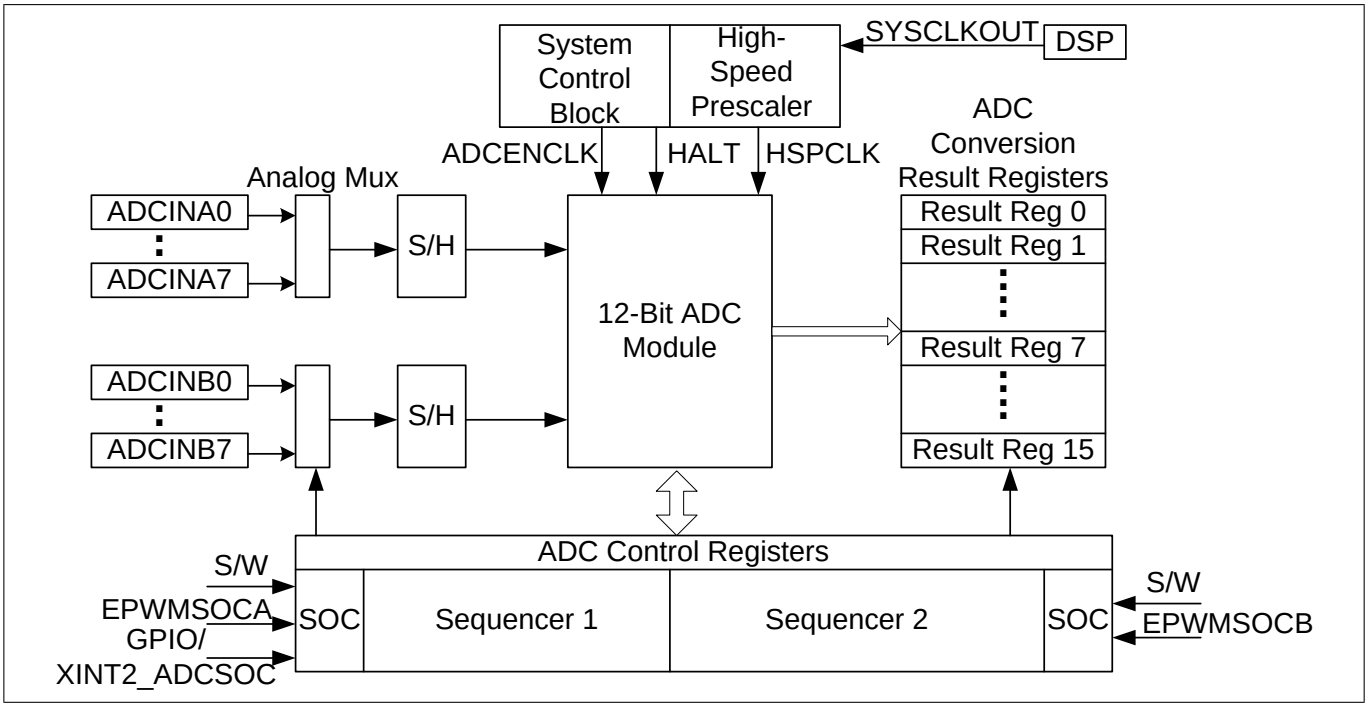

Figure 3.3: ADC Block diagram

zone module then takes actions accordingly. The ePWM channels can be forced to either high or low or high impedance state. In this project, the trip zone signal TZ6 is connected to a manual push button to trip the DSP signals manually. This is in addition to the protection tripping provided on the PD card.

3.4 ADC Module

The TMS320F28335 has a built in 12-bit 16 channel ADC[24] with a reference voltage of 3V. Thus it has a resolution of 0.732 mV per bit. A block diagram of the ADC module is shown in Fig. 3.3

The 16 analog channels are arranged in groups of eight, connected to two 8x1 multiplexers. The outputs of MUX-1 and MUX-2 are connected to two sample and hold circuits, S/H-A and S/H-B. Thus two analog signals can be sampled simultaneously. After sampling, the ADC module converts the sample data into a 12-bit digital value and saves it into one of the result registers from where the processor can access the data. The number of channels to be sampled and the order in which they are to be sampled are determined by the sequencer registers.

The address of the channels to be converted are placed in the sequencer in an appropriate order. For each sequencer maximum eight channels could be selected. In order to start a conversion, a Start of Conversion(SOC) signal is needed. This could be obtained from the PWM module or from software or from an external signal through a GPIO pin. Once the configured channels are converted, the ADC stops and waits for the next SOC signal. The time taken by a conversion is decided by the ADC clock frequency which is obtained by prescaling the system clock. However, using a very high ADC clock will result in non-linearity error in the results.

In this project, two channels in sequencer-1 and one channel in sequencer-2 have been used. The current signals are sampled simultaneously and the DC bus voltage of the inverter is sampled in sequencer-1. The SOC signal is obtained from the event trigger submodule of ePWM1. The highest ADC clock frequency that Texas Instruments recommends, 12.5 MHz is used as the clock signal frequency for the ADC.

3.5 Capture Module

The TMS320F28335 features two enhanced QEP modules(eQEP) as well as four enhanced Capture(eCAP)[26] modules for speed measurement. The motor has a quadrature encoder fitted on the shaft for speed measurement. However, the QEP pins are not available on headers on the Peripheral Explorer Kit used. Hence, only the capture units have been used for speed measurement in this project.

The eCAP module allows time based logging of external logic level signal transitions on its pins. Thus it can be used to measure speed by measuring the time interval between the pulses from one channel of the encoder.The basic block diagram of a capture unit on the TMS320F28335 is shown in Fig. 3.4. Each capture unit is associated with a capture pin and an event prescaler that reduces the input signal frequency. Polarity select bit fields can be used to configure rising or falling edge as the trigger. The system clock increments a 32-bit time stamp counter. When a trigger occurs, the current value of the counter is saved in the capture register and the counter is reset. Then this value is used in speed calculation.

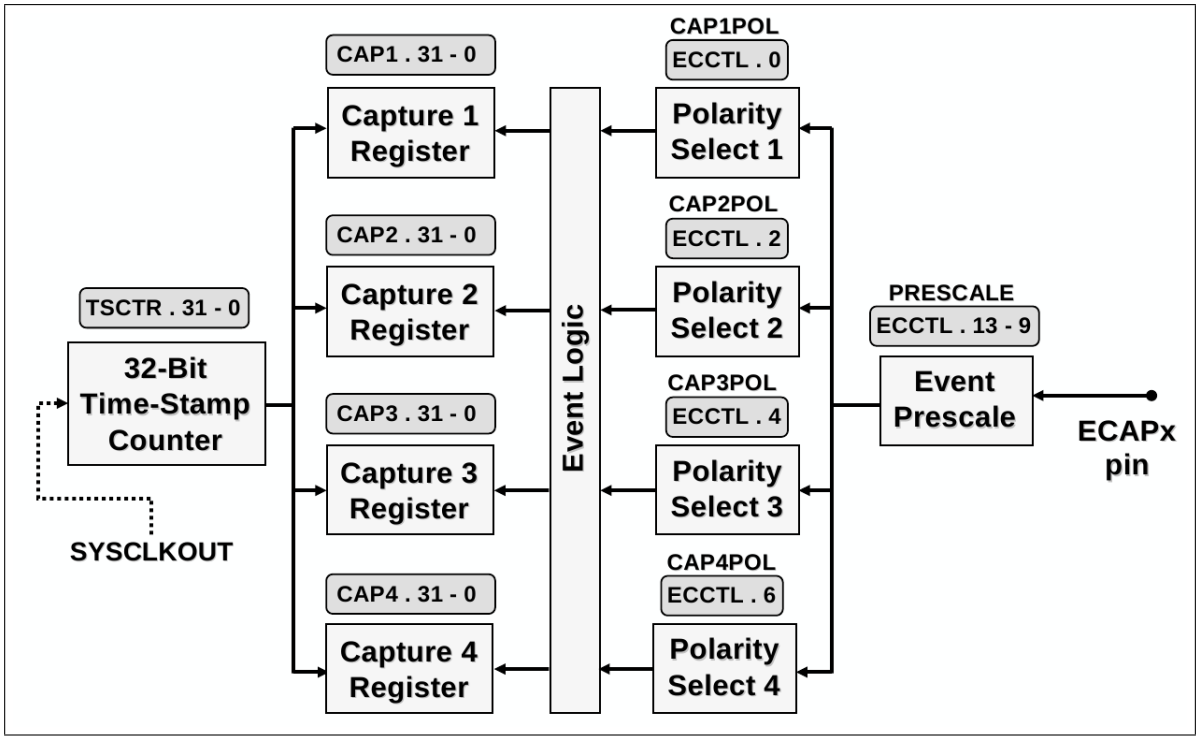

Figure 3.4: eCAP Module Block diagram
Source:28335 eCAP Reference Guide, Texas Instruments

One disadvantage of using the eCAP module for speed sensing is that, unlike the QEP, it cannot detect the direction of rotation. Thus a speed reversal operation in sensored vector control cannot be done by using a capture unit for speed sensing.

3.5.1 Speed Measurement using eCAP

The typical structure of the shaft encoder and the pulses produced by it are as shown in 3.5 (a) and 3.5(b). The shaft has a number of equally spaced projections mounted along the circumference of a circular disc. Light sources and sensors are mounted on either side of the disc such that for every projection on the disc, a pulse is produced at the output. Thus the frequency of the pulses then becomes directly proportional to the speed of rotation. The time duration between any two pulses is also an indicator of the speed of rotation. Thus the speed can be calculated based on either a pulse counting technique or a time measurement technique.

In this project, the capture units are used to measure the time between the pulses to calculate the speed of rotation. At every rising edge of a pulse, the

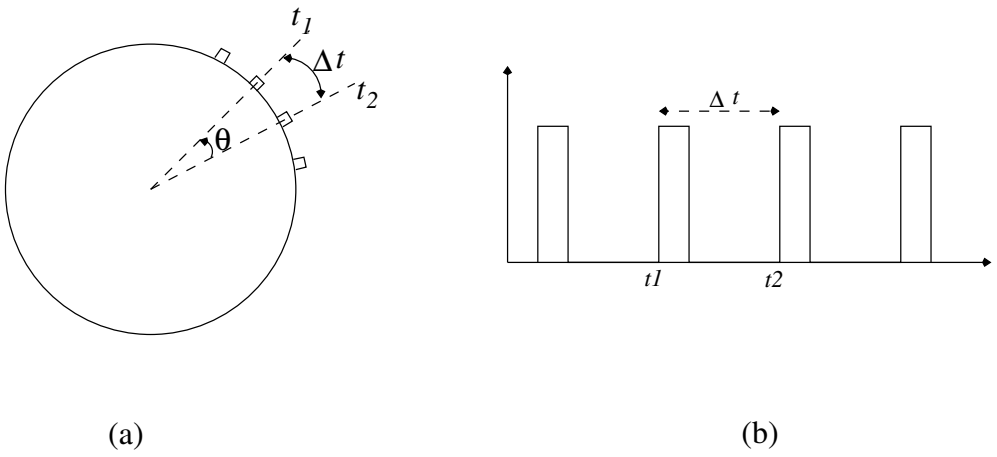

Figure 3.5: Speed measurement using a shaft encoder

counter timestamp value is captured and the timer is reset. Thus the number of clock cycles elapsed between two rising edges can be given as

$$\Delta = Timestamp_{new} - Timestamp_{old} \tag{3.1}$$

Then the time in seconds between two pulses can be obtained as

$$\Delta t = t_2 - t_1 = T_{CLK}\Delta \tag{3.2}$$

where T_{CLK} denotes the time period of the clock input to the capture unit.
Also, if there are n pulses per revolution,

$$\theta = \frac{2\pi}{n} \implies \omega = \frac{\theta}{\Delta t} = \frac{2\pi}{n \times T_{CLK} \times \Delta} \tag{3.3}$$

Maximum value of ω that can be measured corresponds to $\Delta = 1$.

$$i.e\ \omega_{max} = \frac{2\pi}{n \times T_{CLK}} \implies Normalised\,speed = \frac{1}{\Delta} \tag{3.4}$$

Thus if the base speed is chosen to be ω_b, then

$$\text{Speed in p.u} = \frac{\omega_{max}}{\omega_b} \times \frac{1}{\Delta}$$

3.6 Current and voltage sensing

The feedbacks required for vector control are the line currents and the DC bus voltage. Current and voltage sensor cards based on Hall effect sensors are used to obtain these signals. Apart from providing feedbacks, these signals are also used for providing protection to the inverter against possible overcurrent and overvoltages. In this work, the LA100P sensor has been used for current sensing and the LV25P sensor for sensing the DC bus voltage. The burden resistors are selected so as to get an output voltage of 5V, corresponding to 100A for the current sensor and 1000V for the voltage sensor.

3.7 Three phase inverter module

A three phase 2-level Voltage Source Inverter(VSI) from Semikron is used in this project for obtaining the input voltage to the motor terminals. The inverter uses 1200V, 100A IGBT modules as the power switches with each module forming one leg of the inverter. The inverter has a front end diode bridge rectifier for energising the DC bus from an input three phase supply. A pre-charging circuit consisting of resistors in parallel with relays, is connected in series with each line to prevent large inrush currents into the capacitor during energising. The rectifier and the modules are mounted on the heat sink and connected to the DC bus capacitor by conducting sheets. Three Gate driver cards are mounted on the module for giving proper isolation and gate drive for the IGBT gate terminals.

Apart from the basic inverter module, a Protection and delay card has been used for proper interfacing and protection. This will be discussed in the following subsection.

3.7.1 Protection and Delay card

The function of the Protection and Delay(PD) card is to provide protection against faults and also to generate complementary signals with proper rising edge delay. The three top switch PWM signals from the DSP are level shifted and fed to

the PD card. It generates the complementary signals with proper delay using RC circuits and logic gates. These are then given to the gate driver inputs of the inverter module. The outputs of the Hall sensors are also connected to the PD card where they are buffered and fed to high speed opamp comparators. The protection references to the comparators can be set using potentiometers. The output of the comparators indicate fault conditions and are fed to an RS latch using a wired AND logic. The PD card has provision to provide protection for six sensed currents and two DC bus voltages. Also the circuitry for generating delayed complementary signals can be completely disabled by setting the jumpers provided. In this case, the delay has to be generated in software using the deadband module and all the six PWMs can then be directly fed from the DSP. LEDs provided on board are used for fault annunciation. The PD card also has provisions to transmit and recieve the PWMs in either differential or single ended fashion by setting appropriate jumpers. It also controls the relays of the pre-charging circuit thereby protecting the capacitors from large inrush currents.

3.8 Analog Conditioning card

The Analog Conditioning card acts as an interface between the DSP controller and the PD card. It has level shifting circuitry that converts the 3.3V level signals from the DSP to 15V level signals which are given to the PD card. It also has differential transmitting and recieving circuitry on board, so that the PWM signals can be transmitted noise free over longer distances. It also has an on board signal conditioning for the ADC interface which includes filtering, attenuating and level shifting circuitry that converts the bipolar +/-10V level signals from the Hall sensor output to the 0-3V level signal required at the ADC input. It also has a quadrature encoder interface which will recieve the differential 5V level pulses from the encoder and convert it to 3.3V level pulses required by the eCAP unit. Also, a 12-bit, 4-channel serial DAC with an I^2C interface is provided to view the control variables calculated by the DSP. This can be connected to the I^2C interface on the TMS320F28335.

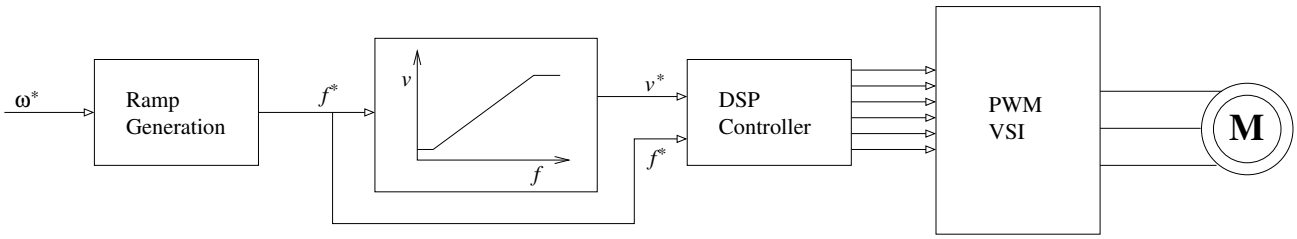

Figure 3.6: Structure of an open loop V/f control

3.9 Testing the Hardware

Before doing a closed loop control, a simple open loop V/f control was run on the built hardware. In this way, the proper operation of all the different modules was verified. Also the working of the estimation algorithms were tested by running the machine in open loop and checking the estimated values.

3.9.1 V/f Control

The block diagram representation for a simple open loop V/f control[1] is shown in Fig. 3.6. The objective of V/f control is to keep the air gap flux inside the machine to a constant value. The speed reference generates a slow ramp which rises upto the reference value. Correspondingly, a V/f profile is used to generate the value of the reference voltage, v^*. In the low speed region, where the stator resistance drop cannot be neglected, a small constant value of v^* is used to overcome the effect of this drop. The reference values of voltage and frequency are the inputs to the DSP controller which generates the appropriate switching pulses to generate these reference values.

Table 3.1: Ratings for the 30kW motor

Parameter	**Value**
Power	30kW
Voltage	380V
Current	59A
Power factor	0.88
Connection	Δ
Speed	1450 rpm
Rotor type	Squirrel Cage

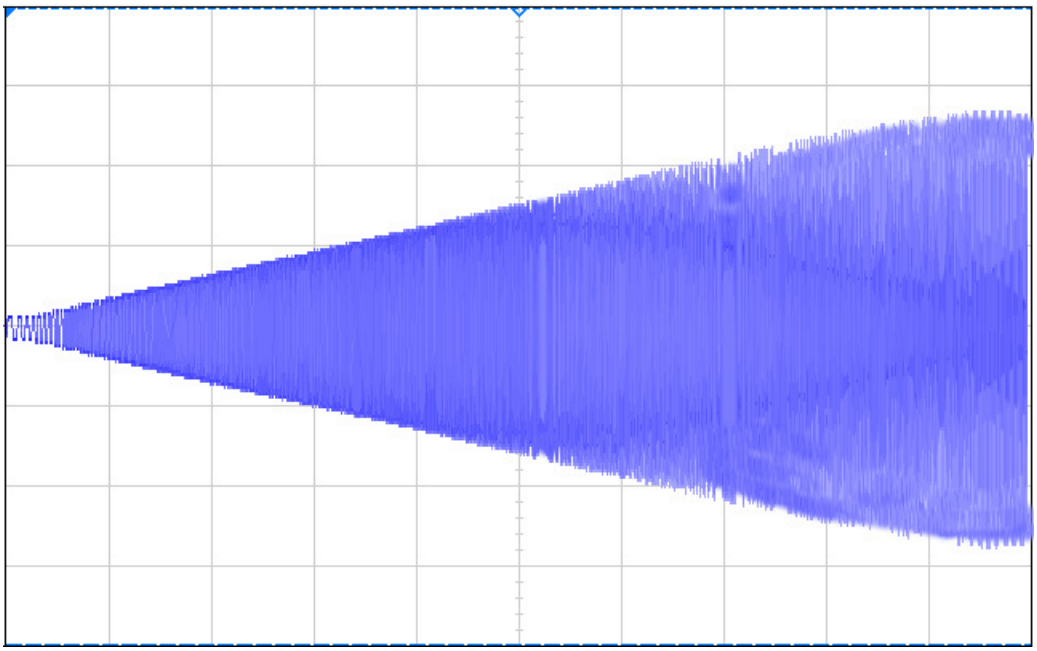

Figure 3.7: R-phase modulating signal.
(X axis: 7.0 s/div, Y axis: .5 pu/div)

In this project, the V/f ratio was calculated so as to keep the flux inside the machine to half the rated value. The ratings of the machine are given in Table 3.1 A speed command of full rated value was given and the ramp rate was adjusted so that a reference of 5 Hz is given for the first 5 seconds and full speed is reached in 65 seconds. A space vector PWM(SVPWM) scheme was adopted to realise the necessary voltage from the inverter. The implementation of this scheme is discussed in section 4.3. The peak value of phase voltage required for operation at half the rated flux is given as

$$V_{ph} = \frac{380}{2} \times \frac{1}{\sqrt{3}} \times \sqrt{2} = 155.13V \tag{3.5}$$

For a given modulation index m, the peak value of the phase voltage in SVPWM switching is given as

$$V_{pk} = 1.15 \times m \times \frac{V_{dc}}{2} \tag{3.6}$$

Assuming a maximum modulation index of 0.9 at 50Hz frequency, the required DC bus voltage can be calculated as

$$1.15 \times 0.9 \times \frac{V_{dc}}{2} = 155.13 \tag{3.7}$$

$$\implies V_{dc} = \mathbf{300V} \tag{3.8}$$

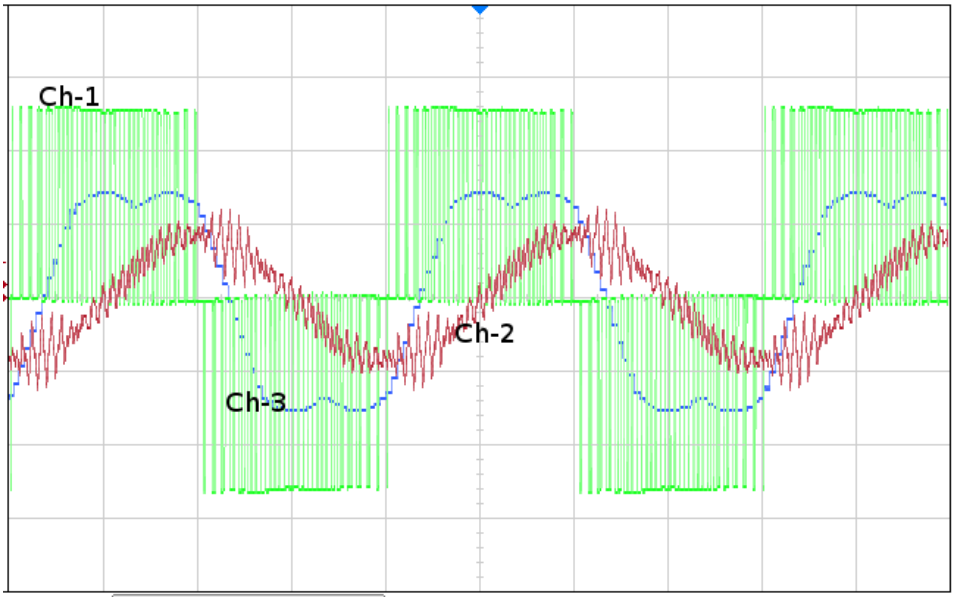

Figure 3.8: R-Y Line voltage, R-phase current and R-phase Modulating signal. *(Ch1- Y axis: 100 V/div, Ch2- Y axis: 20 A/div, Ch3- Y axis: 0.5 pu/div, X-axis: 5ms/div)*

The waveforms of the ramp profile for the modulating signal used in the V/f control is shown in Fig. 3.7. The waveform of the line voltage and current obtained with the calculated values for operation at half the rated flux is shown in Fig.3.8.

3.10 Hardware Setup

The vector control algorithms discussed are implemented on a 30 kW laboratory prototype. Some photographs of the drive setup and the various additional circuitry built for interfacing will be presented in this section.

Figure 3.9: Machine setup for implementing vector control

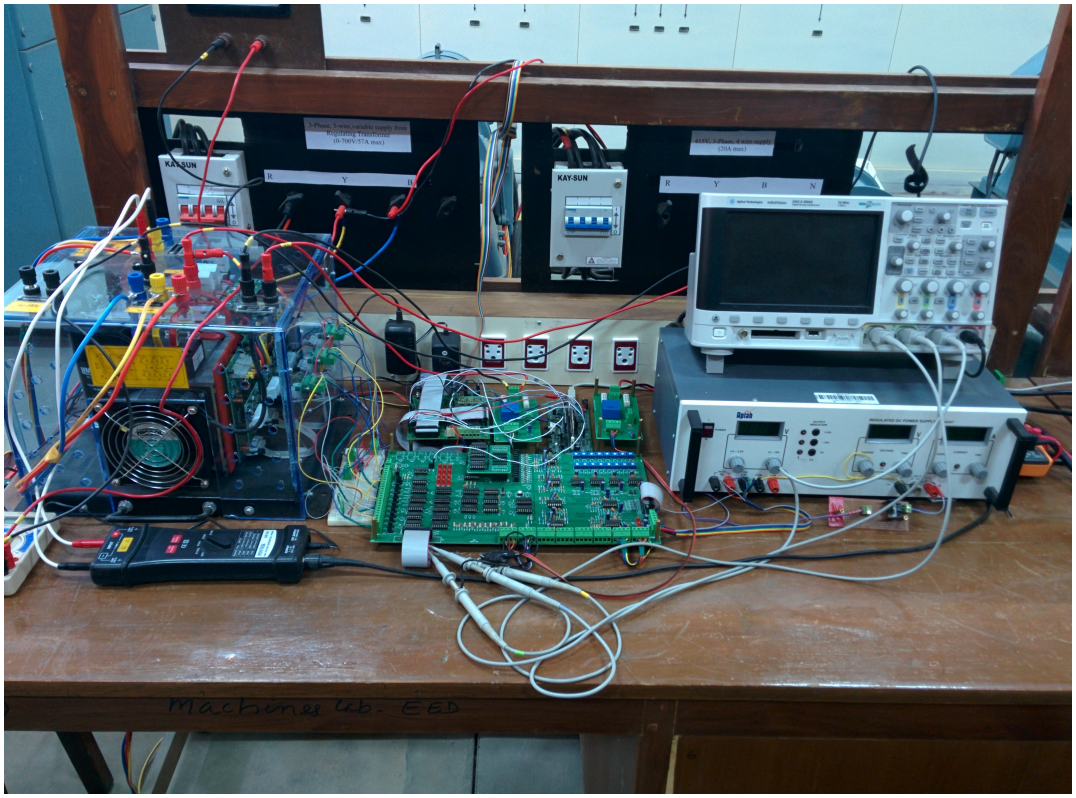

Figure 3.10: Inverter and control hardware

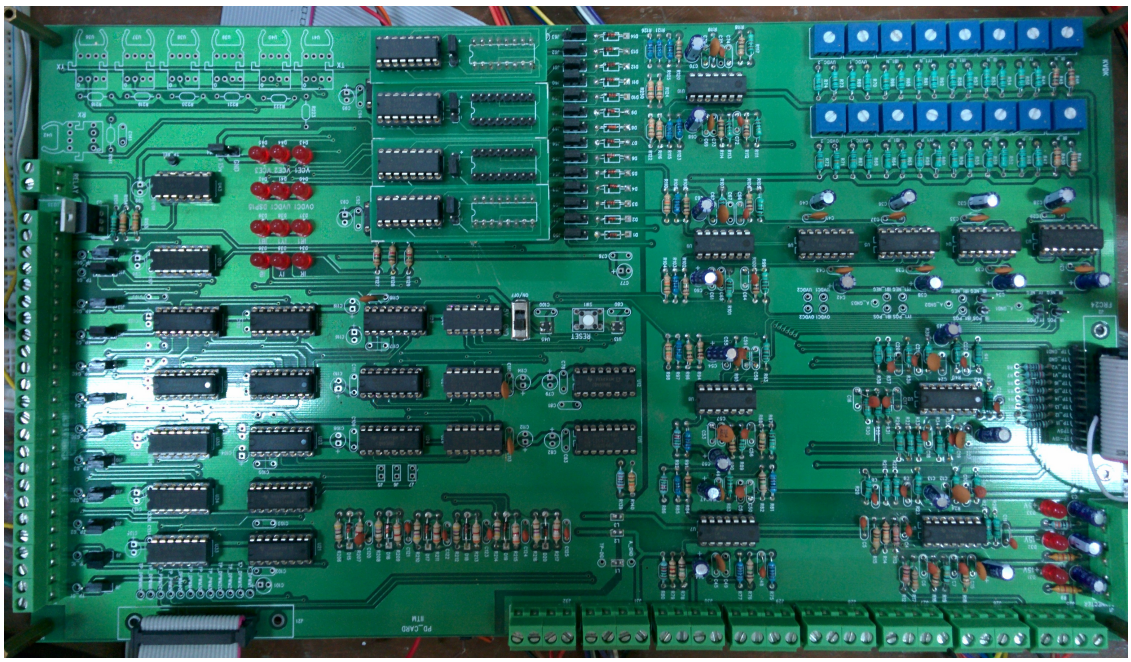

Figure 3.11: Protection and delay card

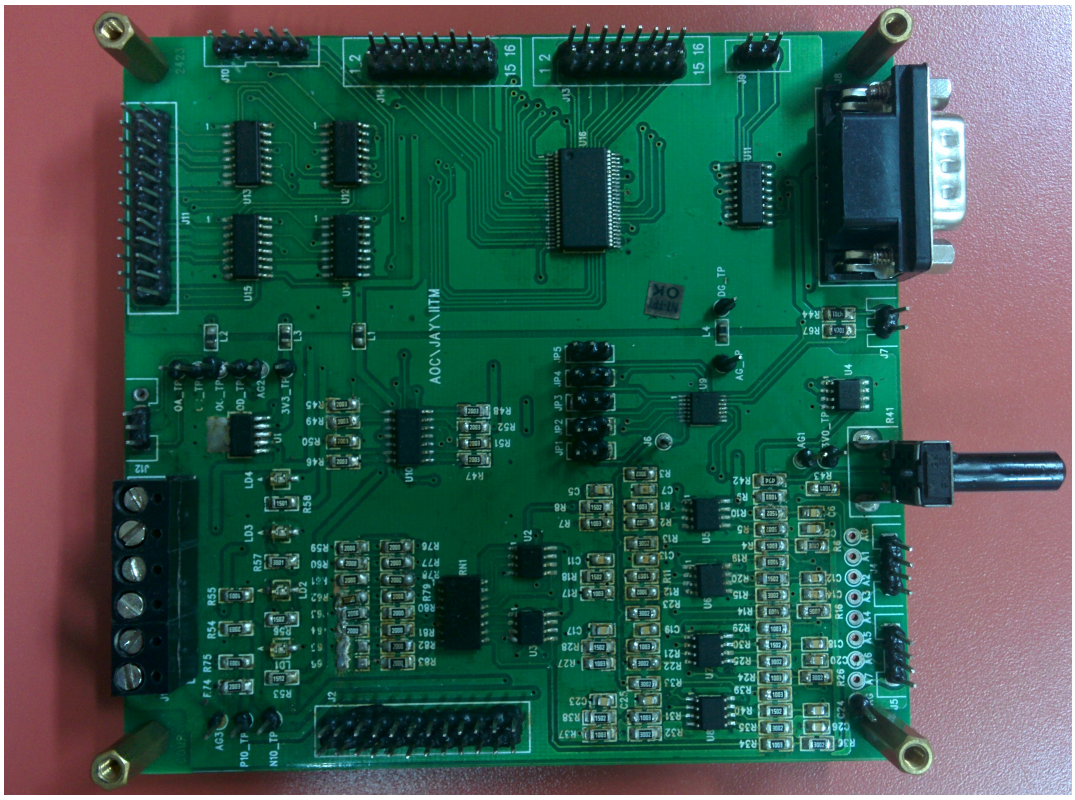

Figure 3.12: Analog conditioning card

3.11 Conclusion

This chapter outlined the features of the TMS320F28335 that are used in implementing the vector control algorithms. The additional hardware used for sensing the voltages and currents and interfacing between the various circuits are also discussed. All the hardware were tested by running a simple open loop V/f control and results are presented. In the next chapter the design of the control structure and the actual implementation of vector control will be discussed.

CHAPTER 4

CONTROL DESIGN AND IMPLEMENTATION

4.1 Introduction

In this chapter, the detailed design of various controllers and estimators used in vector control is presented. All design is done for the 30 kW induction motor whose ratings are specified in Table. 5.1. The design is done following a per unit system with defined base quantities, which makes the implementation easier.

4.2 Parameter estimation

The design of vector control for a machine requires the knowledge of the equivalent circuit parameters of the machine. These parameters for the machine are calculated by performing the No Load(NL) and Blocked Rotor(BR) tests. The stator resistance is calculated by injecting a DC voltage and measuring the current drawn. The results obtained from the NL and BR tests are summarised in Table. 4.1

Table 4.1: No load and Blocked Rotor Test

Test	V_{l-l}	I_l	Power
NL	380V	14.5A	1105W
BR	87V	59A	3017W

The calculated values of the machine parameters using the data from the above tests are given in Table 4.2. These values will be used for designing the control parameters

Table 4.2: Equivalent circuit parameters

Parameter	R_s	$R_r^{'}$	L_{ls}	L_{lr}	L_m
Value	0.1273 Ω	0.127 Ω	1.341 mH	1.341 mH	45.219 mH

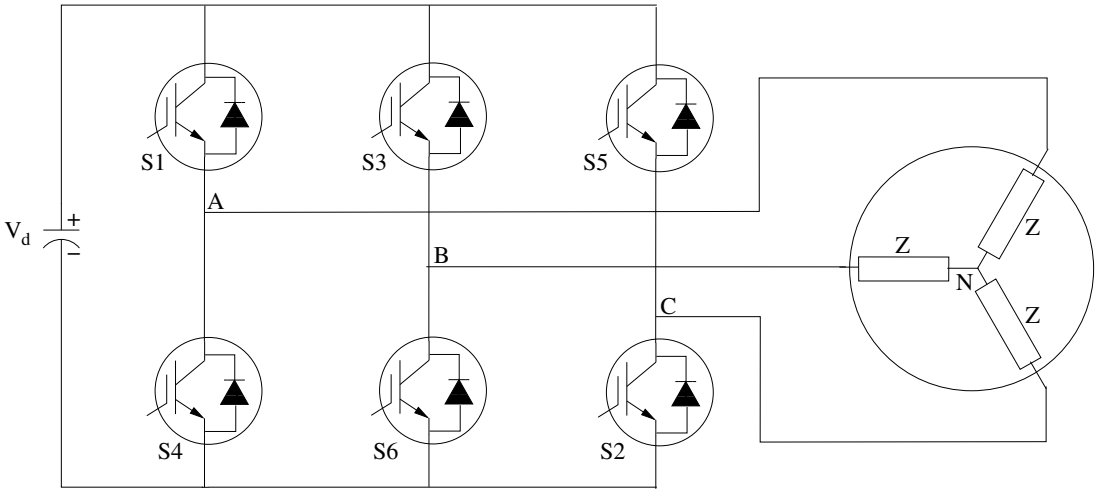

Figure 4.1: 2-level VSI topology

4.3 SVPWM switching for inverter

The power circuit topology for a 2-level VSI using IGBT switches is shown in Fig. 4.1.For this inverter, there are 8 possible combinations of switching. Each of the switching combination corresponds to a particular space vector location. Of these, two are zero vectors corresponding to all top switches or all bottom switches ON. The other six vectors are directed along the vertices of a regular hexagon giving six sectors S_1 - S_6 as shown in Fig.4.2.

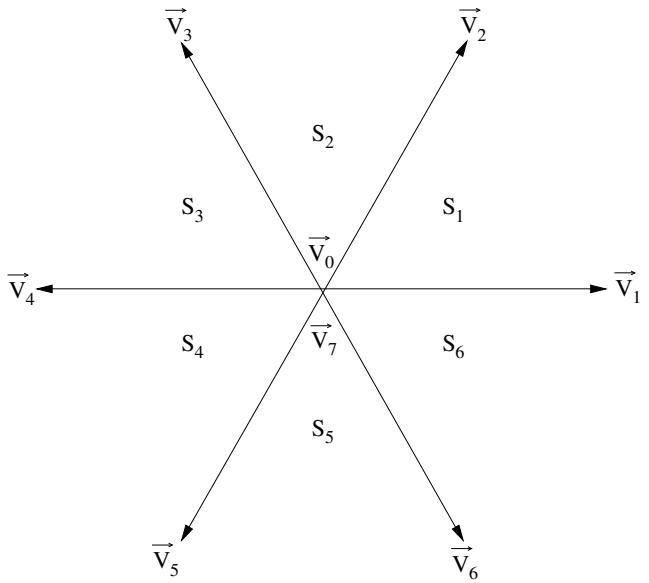

Figure 4.2: Space vector locations for the 2-level VSI

The various possible switching combinations, along with their corresponding space vector locations and the components of these vectors along the α and β axis are listed in Table. 4.3. The state '0' corresponds to the switch being OFF and state '1' corresponds to the switch being ON. The fundamental idea of SVPWM is

Table 4.3: Space vectors for different switching states

S1	S3	S5	V_{AN}	V_{BN}	V_{CN}	Vector	V_α	V_{beta}
0	0	0	0	0	0	V_0	0	0
1	0	0	$2V_d/3$	$-V_d/3$	$-V_d/3$	V_1	$2V_d/3$	0
0	1	0	$-V_d/3$	$2V_d/3$	$-V_d/3$	V_3	$-V_d/3$	$V_d/\sqrt{3}$
1	1	0	$V_d/3$	$V_d/3$	$-2V_d/3$	V_2	$V_d/3$	$V_d/\sqrt{3}$
0	0	1	$-V_d/3$	$-V_d/3$	$2V_d/3$	V_4	$-V_d/3$	$-V_d/\sqrt{3}$
1	0	1	$V_d/3$	$-2V_d/3$	$V_d/3$	V_6	$V_d/3$	$-V_d/\sqrt{3}$
0	1	1	$-2V_d/3$	$V_d/3$	$V_d/3$	V_4	$-2V_d/3$	0
1	1	1	0	0	0	V_7	0	0

that a given reference vector can be realised in an average sense by a combination of the basic space vectors of the 2 level VSI. The reference voltage vector is obtained by mapping the desired 3-ϕ output voltages to the $\alpha\beta$ frame. It is then realised by using the vectors that form the boundary of the sector in which the reference lies. Fig. 4.3 illustrates this technique for a vector that lies in sector 1.

For any sampling interval T_s during which the desired vector is at a location in sector 1 as shown, the sampling interval is divided into 3 sub intervals T_1, T_2 and T_0. The switching is done to obtain the vector $\vec{V_1}$ for T_1 seconds, $\vec{V_2}$ for T_2 seconds and any of the zero vectors for T_0 seconds. The intervals T_0, T_1 and T_2 are chosen such that volt seconds produced by the active vectors and the zero vector

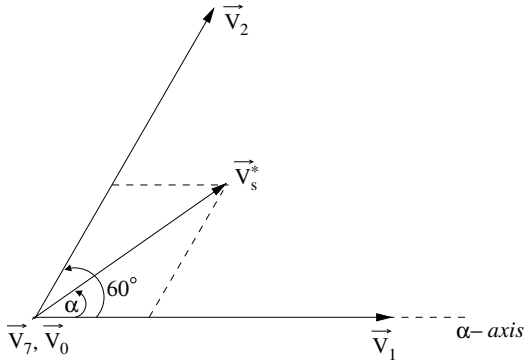

Figure 4.3: Synthesising a desired reference vector by SVPWM

along the α and β axis, are the same as that produced by v_s^*. Therefore,

$$|V_s^*|T_s \cos\alpha = T_1|\vec{V_1}| + T_2|\vec{V_2}| \cos 60^\circ \quad (4.1)$$

$$|V_s^*|T_s \sin\alpha = T_2|\vec{V_2}| \sin 60^\circ \quad (4.2)$$

Solving for T_1 and T_2 and defining the modulation index as $m = \frac{|\vec{V_s}*|}{|\vec{V_1}|}$ gives

$$T_1 = mT_s \frac{\sin(60^\circ - \alpha)}{\sin 60^\circ} \quad (4.3)$$

$$T_2 = mT_s \frac{\sin\alpha}{\sin 60^\circ} \quad (4.4)$$

$$T_0 = T_s - T_1 - T_2 \quad (4.5)$$

The angle α is easily obtained from the components along the α and β axis. Since the same equations apply to any sector, only a 60° sine lookup table is required. Once the duration of the sub-intervals have been calculated, the the compare values that are to be put into the CMP registers of the ePWM module can be calculated for the specific switching pattern used. The switching pattern used in this project for vectors in sector S_1 is as shown in Fig. 4.4.

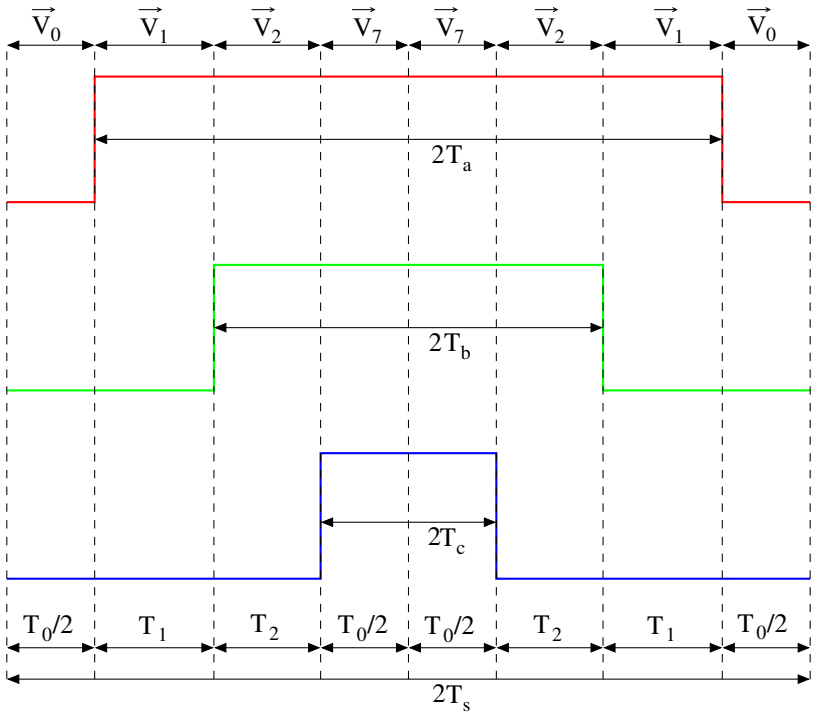

Figure 4.4: Switching pattern for 2 succesive sampling intervals

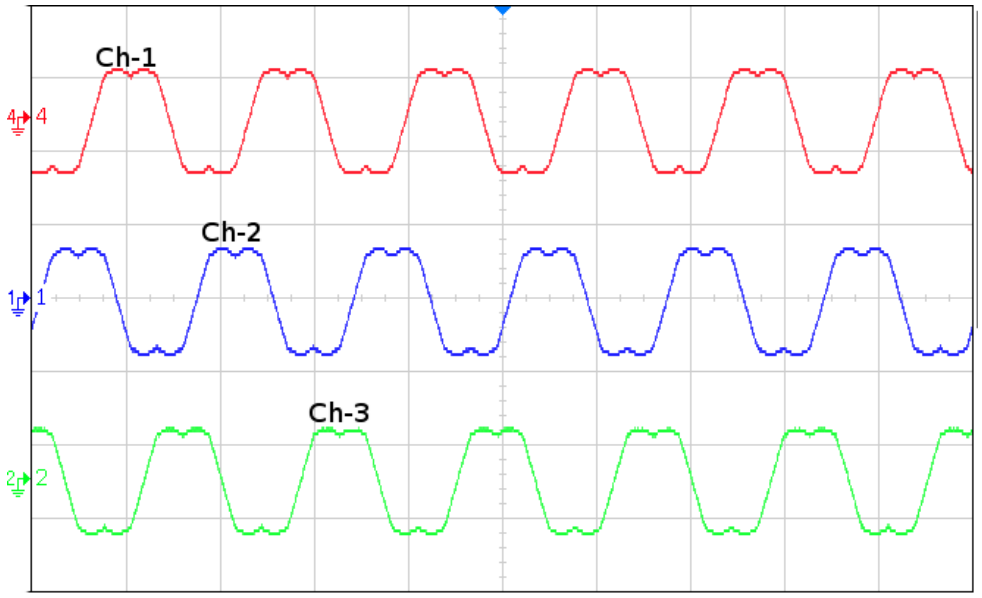

Figure 4.5: 3-ϕ modulating waveforms for steady state operation at 50 Hz *(Ch1- R ph, Ch2- Y ph, Ch3- B-ph, X-axis: 11.8 ms/div, Y-axis: 1.3 pu/div)*

For this pattern it can be seen that,

$$\begin{aligned} T_a &= T_0/2 \\ T_b &= T_1 + T_0/2 \\ T_c &= T_s - T_0/2 \end{aligned}$$

Similarly for each sector, the relation between the calculated durations of each vector and the duty ratio of the switches in each leg can be obtained. When these duty ratios are normalised w.r.t the sampling interval T_s, it directly gives the value that should be put into the compare registers. The relation between the vector durations calculated, and the switch duty ratios in each sector is summarised in Table. 4.4

Table 4.4: Compare register values for different sectors

Sector	S1	S2	S3	S4	S5	S6
T_a	$T_s - T_0/2$	$T_1 + T_0/2$	$T_0/2$	$T_0/2$	$T_2 + T_0/2$	$T_2 + T_0/2$
T_b	$T_2 + T_0/2$	$T_s - T_0/2$	$T_s - T_0/2$	$T_1 + T_0/2$	$T_0/2$	$T_0/2$
T_c	$T_0/2$	$T_0/2$	$T_2 + T_0/2$	$T_s - T_0/2$	$T_s - T_0/2$	$T_1 + T_0/2$

The waveform of the modulating signal obtained from the above implementation for a steady state, 50 Hz operation is given in Fig. 4.5.

4.4 The Per Unit System

In this work, a Per Unit(pu) system has been followed for implementing the control algorithms. This makes the digital implementation easy as all quantities are brought to the same range of values in pu. Thus the controller can use a common number format for performing the computations. For per unitisation of quantities, base values are required which are chosen as per convenience. Table 4.5 gives the base values chosen for the different quantities.

Table 4.5: PU base quantities

Voltage(V_b)	155.13 V
Current(I_b)	20A
Frequency(f_b)	50Hz
Angle(θ)	$2\pi rad$

The base values for the other quantities are calculated as follows:

$$Base\ Angular\ frequency, \omega_b = 2\pi_b = 314.15\, rad/s \tag{4.6}$$

$$Base\ Resistance, R_b = V_b/I_b = 7.7565\,\Omega \tag{4.7}$$

$$Base\ Flux\ Linkage, \psi_b = \frac{V_b}{\omega_b} = 0.4938\, Wb \tag{4.8}$$

$$Base\ Inductance, L_b = \frac{\psi_b}{I_b} = 0.02469\, H \tag{4.9}$$

4.5 Design of controllers

The vector control system uses PI controllers for controlling the flux, speed, d-axis current and q-axis current. The dynamic peformance of the drive is determined by these controllers and therefore it is important to design them for the required performance. Also, the output limiters of the PI controllers ensure that the currents and voltges of the motor are always within the limits. Thus the limiter values should also be designed appropriately.

In this work, the PI controllers have been designed so as to have a first order response for the closed loop system. The inverter and sensor dynamics are neglected and they are treated as constant gain blocks. The bandwidth of the outer loops are selected much smaller than that of the inner loops. This allows us to

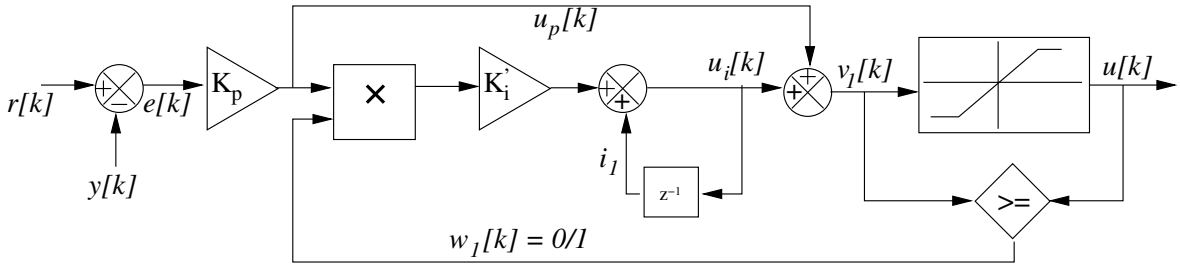

Figure 4.6: Block diagram of the digital PI controller

neglect the inner loop dynamics while designing the outer loops.

4.5.1 PI controller with output limiter and antiwindup

The PI controllers used in vector control are provided with output limiters and integrator antiwindup. Output limiters ensure that the currents and voltages of the machine are within rated limits at all times. The integrator antiwindup disables the integral action when the output of the controller reaches its limit value. This helps in making the controller faster.The structure of the digital PI controller with output limiter and integrator antiwindup is shown in Fig.4.6.
K_p denotes the proportional gain of the controller. The integral gain consists of two gain blocks K_p and $K_i^{'}$ connected in cascade. However, the output of the gain block K_p is multiplied by a binary signal w_1 before passing through the gain stage K_i. Thus the effective integral gain of the controller, K_i is then given as

$$K_i = K_p \times K_i^{'} \times w_1 \tag{4.10}$$

The value of w_1 is zero if the output has reached its limit and one otherwise. Thus w_1 provides the antiwindup action by setting the integral gain to zero when the output hits the limits. The discrete equations implemented are:

$$\text{Proportional term: } u_p[k] = K_p e[k] \tag{4.11}$$

$$\text{Integral term: } u_i[k] = u_i[k-1] + \Big(K_p K_i e[k]\Big) w_1 \tag{4.12}$$

$$v_1[k] = u_p[k] + u_i[k] \tag{4.13}$$

The PI controller output is obtained as:

$$u[k] = \begin{cases} U_{max} & \text{if } v_1[k] > U_{max} \\ U_{min} & \text{if } v_1[k] < U_{min} \\ v_1[k] & \text{otherwise.} \end{cases}$$

4.5.2 d and q axis current controllers

Current controllers[2] primarily deal with the dynamics of the power supply and armature. These should have a response slower than the inverter, but faster than the speed controller and flux controller. From 2.62 and 2.63,

$$\begin{aligned} v_{sd} &= R_s i_{sd} + \sigma L_s \frac{di_{sd}}{dt} - \sigma L_s i_{sq} \omega_{mr} + (1-\sigma) L_s \frac{di_{mr}}{dt} \\ v_{sq} &= R_s i_{sq} + \sigma L_s \frac{di_{sq}}{dt} + \sigma L_s i_{sd} \omega_{mr} + (1-\sigma) L_s \omega_{mr} i_{mr} \end{aligned}$$

Thus by adding appropriate feed forward terms to the input voltages, a first order response can be obtained for the currents and the plant model can be written as a first order transfer function. The feed forward terms are given as

$$v_{ffd} = -\sigma L_s i_{sq} \omega_{mr} + (1-\sigma) L_s \frac{di_{mr}}{dt} \tag{4.14}$$

$$v_{ffq} = \sigma L_s i_{sd} \omega_{mr} + (1-\sigma) L_s \omega_{mr} i_{mr} \tag{4.15}$$

where v_{ffd} and v_{ffq} are respectively the feed forward terms of the d and q axis voltages. Since the loop structure is the same for both d and q axis current loops, the design and controller parameters for both are the same. The block diagram of the current control loop is as shown in Fig. 4.7

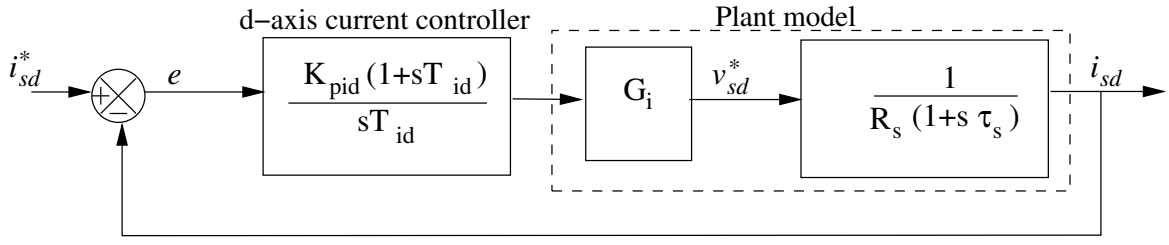

Figure 4.7: Structure of the current control loop

If the bandwidth of the current control loop is chosen as f_b Hz,

$$\tau_b = \frac{1}{2\pi f_b} \tag{4.16}$$

Then the condition for the loop to have a first order response can be written as

$$\frac{K_p(1+sT_{id})}{sT_{id}} \times G_i \times \frac{1}{R_s(1+s\tau_s)} = \frac{1}{s\tau_b} \tag{4.17}$$

where $\tau_s = \frac{\sigma L_s}{R_s}$. By choosing $T_{id} = \tau_s$, then from Eqn. 4.17,

$$\frac{K_p G_i}{R_s \tau_s} = \frac{1}{\tau_b} \implies \boldsymbol{K_p = \frac{R_s \tau_s 2\pi f_b}{G_i}} \tag{4.18}$$

Now the integral gain of the PI controller can be obtained as

$$K_i = \frac{K_p}{T_{id}} \implies \boldsymbol{K_i = \frac{K_p R_s}{\sigma L_s}} \tag{4.19}$$

The subscript b will be used to denote the base quantities and the subscript *(pu)* to denote the quantities in pu. Then,

$$\begin{aligned} e = i^*_{sq} - i_{sq} &= I_b(i^*_{sq(pu)} - i_{sq(pu)}) \\ e_{(pu)} &= i^*_{sq(pu)} - i_{sq(pu)} \end{aligned}$$

Using 4.11 and 4.12, the output of the controller can be written as

$$\begin{aligned} v^*_{sd}[k] &= v^*_{sd}[k-1] + G_i K_p I_b e_{(pu)}[k] + G_i K_i I_b T_s e_{(pu)}[k] \\ \implies v^*_{sd(pu)}[k] &= v^*_{sd(pu)}[k-1] + G_i \frac{K_p I_b}{V_b} e_{(pu)}[k] + G_i \frac{K_i I_b T_s}{V_b} e_{(pu)}[k] \end{aligned}$$

where T_s denotes the sampling time period. From the above equations the pu values of proportional and integral gains for the PI controller can be written as

$$\boldsymbol{K_{p(pu)} = \frac{K_p I_b}{V_b}} \qquad \boldsymbol{K_{i(pu)} = \frac{K_i I_b T_s}{V_b}} \tag{4.20}$$

Per unit feedforward terms : The d and q axis feedforward terms in pu are obtained by suitably dividing by the base values. These are given as

$$\begin{aligned} v_{ffd(pu)} &= \frac{-\sigma L_s \omega_{mr(pu)} i_{sq(pu)} I_b \omega_b}{G_i} \\ v_{ffq(pu)} &= \frac{[\sigma \omega_{mr(pu)} i_{sd(pu)} + (1-\sigma)\omega_{mr(pu)} i_{mr(pu)}] L_s \omega_b I_b}{G_i} \end{aligned}$$

4.5.3 Flux controller

The flux controller controls the flux inside the machine by controlling the magnetising current i_{mr}. The controller output is the reference for the d-axis current. Thus this controller bandwidth is to be chosen much lower than the d-axis current controller. This allows to neglect the dynamics of the d-axis current controller in the design. The basic structure of the control loop is as shown in Fig. 4.8.

If the bandwidth of the i_{mr} control loop is chosen as f_{bmr} Hz, then

$$\tau_{bmr} = \frac{1}{2\pi f_{bmr}}$$

Then the condition for the loop to have a first order response can be written as

$$\frac{K_p(1+sT_{im})}{sT_{im}} \times \frac{1}{(1+s\tau_r)} = \frac{1}{s\tau_{bmr}} \tag{4.21}$$

where $\tau_r = \frac{L_r}{R_r}$. By choosing $T_{im} = \tau_r$,

$$\frac{K_p}{\tau_r} = \frac{1}{\tau_{bmr}} \implies \boldsymbol{K_p = \frac{\tau_r}{\tau_{bmr}}} \tag{4.22}$$

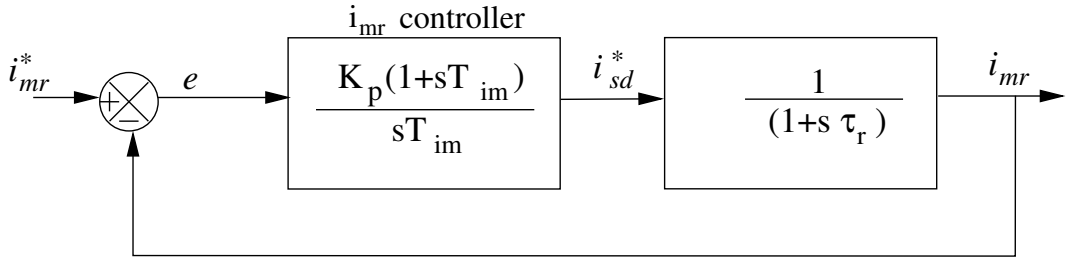

Figure 4.8: Structure of the i_{mr} control loop

Now, the integral gain of the controller is obtained as

$$K_i = \frac{K_p}{\tau_r} \implies \boldsymbol{K_i = \frac{1}{\tau_{bmr}}} \tag{4.23}$$

From the block diagram,

$$e[k] = i^*_{mr}[k] - i_{mr}[k]$$
$$\implies e_{(pu)}[k] = i^*_{mr(pu)}[k] - i_{mr(pu)}[k]$$

Then, using 4.11 and 4.12, the output of the controller is obtained as

$$i^*_{sd(pu)}[k] = i^*_{sd(pu)}[k-1] + K_p e_{(pu)}[k] + K_i T_s e_{(pu)}[k] \tag{4.24}$$

where T_s denotes the sampling time period. From 4.24, the pu values of the proportional and integral gains of the controller is obtained as

$$\boldsymbol{K_{p(pu)} = K_p} \qquad \boldsymbol{K_{i(pu)} = K_i T_s} \tag{4.25}$$

4.5.4 Speed Controller

The speed control loop is as shown in fig. 4.9. The output of the speed PI controller is the reference value of the q-axis current. The current control loop is replaced by its equivalent first order transfer function of bandwidth as designed above. The inverter and speed sensor are treated as constant gain blocks and their dynamics are neglected. The sensor gain is taken as unity.

The design is done using a symmetric optimal pole placement method. The objective here is to design the controller so that the maximum phase angle is obtained at the gain crossover frequency. Considering the block diagram of the control loop shown in Fig. 4.9, the open loop transfer function of the loop can be written as

$$G(s) = \frac{K_p K_t i^*_{mr}(1 + s\tau_\omega)}{J\tau_\omega s^2(1 + s\tau_{is})} \tag{4.26}$$

The bode plot of this transfer function has the form shown in Fig. 4.10. It has an initial slope of -40 dB/decade and then changes to -20 dB/decade due to the

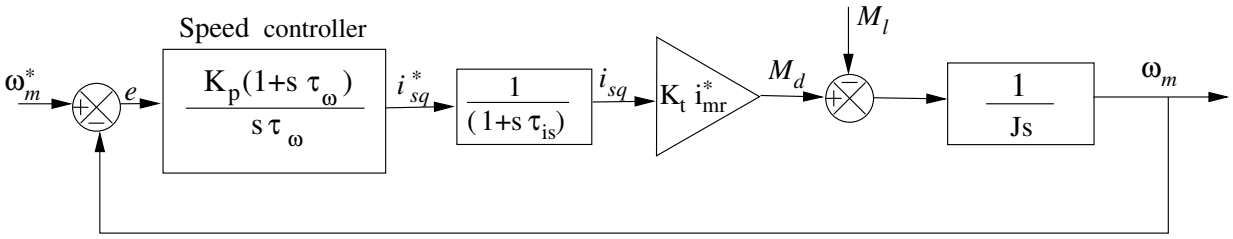

Figure 4.9: Structure of the speed control loop

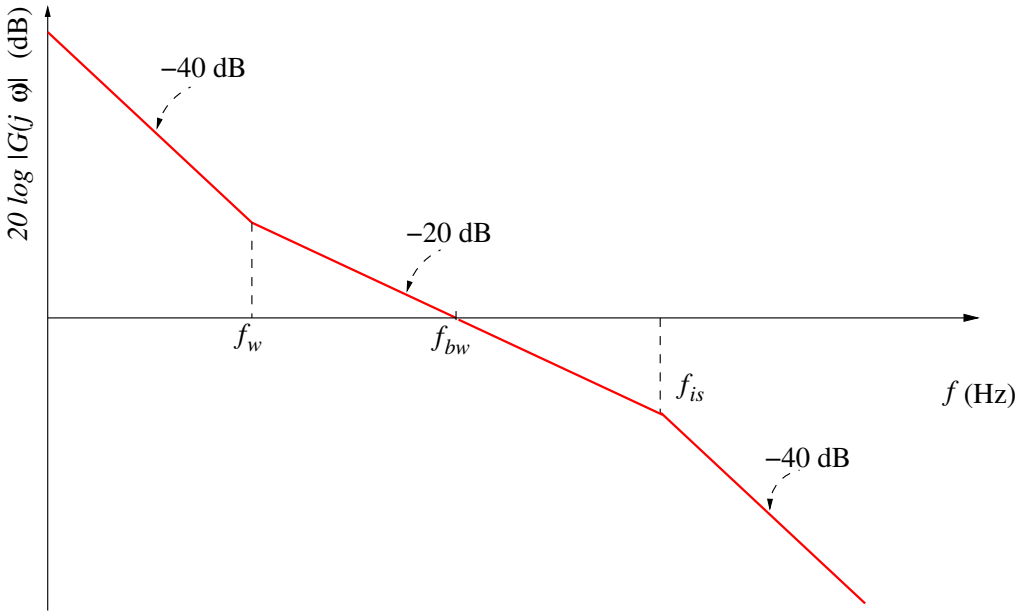

Figure 4.10: Bode plot for the speed loop

effect of the zero of the controller. It again changes back to -40 dB/decade due to the pole in the current control loop. For such a system, the maximum phase angle can be shown to occur at the geometric mean of the two corner frequencies. Thus the aim is to design the speed controller such that the system gain crosses the 0 dB point at this frequency, with a slope of -20 dB/decade.

Thus, once the value of f_{bw} is chosen appropriately, the value of f_w required can be calculated as

$$f_w = \frac{f_{bw}^2}{f_{is}} \tag{4.27}$$

The value of τ_ω for the controller is then obtained as

$$\boldsymbol{\tau_\omega = \frac{1}{2\pi}\frac{f_{is}}{f_{bw}^2}} \tag{4.28}$$

Then the condition for f_{bw} to be the gain crossover frequency of the system can be written as

$$\left.\frac{K_p K_t i^*_{mr}(1+s\tau_\omega)}{J\tau_\omega s^2(1+s\tau_{is})}\right|_{s=2\pi f_{bw}} = 1 \tag{4.29}$$

Since $\tau_\omega >> \tau_{b\omega}$ and $\tau_{is} << \tau_{b\omega}$, approximations can be made as $1 + s\tau_\omega \approx s\tau_\omega$ and $1 + s\tau_{is} \approx 1$. Then Eq. 4.29 simplifies to

$$\frac{K_p K_t i^*_{mr}}{2\pi J f_{b\omega}} = 1$$
$$\implies \boldsymbol{K_p = \frac{2\pi f_{bw} J}{K_t i^*_{mr}}} \tag{4.30}$$

Since the output of the PI controller is a current, the pu values of the proportional and integral gains of the controller can be written as

$$\boldsymbol{K_{p(pu)} = \frac{K_p \omega_b}{I_b}} \qquad \boldsymbol{K_{i(pu)} = \frac{K_i T_s \omega_b}{I_b}} \tag{4.31}$$

where $K_i = \frac{K_p}{\tau_\omega}$.

Estimation of the moment of inertia(J) of the machine It is seen that the design of the speed controller requires the value of the shaft inertia, J. An approximate value of J is obtained by doing a retardation test.

In this test the machine is run at a speed slightly greater than the rated speed and the supply is suddenly cut off. The machine starts to decelerate and this variation of the angular speed with time is recorded. At any speed ω_m, the power consumed in supplying the rotational losses is equal to the rate of change of kinetic energy. i.e.

$$P = \frac{d}{dt}[\frac{1}{2}J\omega_m^2] = J\omega_m \frac{d\omega_m}{dt} \tag{4.32}$$

From the retardation test, $\frac{d\omega_m}{dt}$ at rated speed speed is obtained. Now the machine is again run at rated speed and the input power is noted. Neglecting the core losses and copper losses, the no load power is approximately equal to P. Thus J can now be calculated from Eq. 4.32.

For the 30kW machine, the retardation test gave a value of J = 1.631 $kg - m^2$. Then the controller was designed for a bandwidth of 5 Hz. Although this procedure

gives the design values of the speed controller, the implementation requires some manual fine tuning of the controller, as the calculated value of inertia from the retardation test can have a significant error.

4.5.5 Output limits for the PI controllers

As discussed in Sec. 4.5.1, all the PI controllers have limiters at their outputs and integrator antiwindups. The limits of the speed controller and flux controller are set at the rated values of the q-axis and d-axis currents respectively, while that of the current controllers are set at the rated values of the dq axis voltages. Thus the rated values of these quantities are to be calculated for properly setting the output limits.

For the 30kW machine whose parameters are given in Table 4.2,

Rated speed of rotor flux = *314.159 elect.rad/s*

Rated speed of motor = $\frac{1450}{1500} \times 314.159$ = *303.6873 elect.rad/s.*

Rated Torque = $\frac{\text{Rated Power}}{\text{Rated Speed}} = \frac{30{,}000}{151.844}$=*197.57 Nm*

Also,

$$\tau_r = \frac{L_r}{R_r} = 0.366\,s \qquad \sigma_r = \frac{L_{lr}}{L_m} = 0.0297 \qquad \sigma = \frac{L_s L_r - L_m^2}{L_s L_r} = 0.05677$$

$$\text{and} \quad M_d = K_t i_{mr} i_{sq} \quad \text{where} \quad K_t = \frac{2}{3}\frac{P}{2}\frac{L_m}{1+\sigma_r} = 0.058555\,Nm/A^2$$

Then, using 2.48,

$$\text{Rated}\, i_{sq} = \sqrt{\frac{(\omega_m r - \omega) M_d \tau_r}{K_t}} = \mathbf{117.9274\,A}$$

$$\text{Rated}\, i_{sd} = \frac{M_d}{K_t i_{sq}} = \mathbf{30.7821\ \ A}$$

The rated value of i_{mr} is the same as that of i_{sd}. The rated values of v_{sd} and v_{sq} can be obtained from Eq.(2.62) and Eq.(2.63) by substituting the rated values for the currents i_{sd} and i_{sq}.

$$v_{sd,rated} = R_s i_{sd,rated} - \sigma L_s \omega_{mr} i_{sq,rated} = \mathbf{-94.006\ \ V}$$

$$v_{sq,rated} = R_s i_{sq,rated} + \sigma L_s \omega_{mr} i_{sd,rated} + (1-\sigma) L_s \omega_{mr} i_{mr,rated} = \mathbf{465.266\,V}$$

The controller parameters obtained for the 30kW machine from the above design are given in Table. 4.6

Table 4.6: Controller parameters

Controller	$f_b(Hz)$	$K_p(pu)$	$K_i(pu)$	$U_{max}(pu)$	$U_{min}(pu)$
i_{sd}	100	0.19255	0.004815	0.2	-0.2
i_{sq}	100	0.19255	0.004815	0.87	-0.87
i_{mr}	10	22.987	0.000273	0.75	-0.75
ω_m	5	20	0.00002	1.25	-1.25

4.6 Implementation of the current model

The current model of the induction machine is used for calculating the instantaneous position of the rotor flux in vector control. This is described by the equations 2.47 and 2.48. The equations are discretised and per unitised for implementation. From 2.47, dividing throughout by the base value I_b gives

$$i_{sd(pu)} = i_{mr(pu)} + \tau_r \frac{di_{mr(pu)}}{dt} \tag{4.33}$$

The above equation can be dicretised as

$$\begin{aligned} i_{sd(pu)}[k] &= i_{mr(pu)}[k] + \tau_r \frac{i_{mr(pu)}[k+1] - i_{mr(pu)}[k]}{T_s} \\ \implies i_{mr(pu)}[k+1] &= i_{mr(pu)}[k] + \frac{T_s}{\tau_r}[i_{sd(pu)}[k] - i_{mr(pu)}[k]] \end{aligned} \tag{4.34}$$

Similarly, dividing 2.48 throughout by the base speed ω_b gives

$$\frac{1}{f_b}\frac{d\theta_{(pu)}}{dt} = f_{s(pu)} = f_{r(pu)} + \frac{i_{sq_(pu)}}{\tau_r i_{mr(pu)} \omega_b} \tag{4.35}$$

This equation can be written in discrete form as

$$f_{s(pu)}[k+1] = f_{r(pu)}[k+1] + \frac{1}{\tau_r \omega_b} \frac{i_{sq(pu)}[k]}{i_{mr(pu)}[k+1]} \tag{4.36}$$

Now the instantaneous position of rotor flux angle,$\rho(t)$ can be obtained as

$$\rho(t) = \int \omega_s . dt \tag{4.37}$$

Dividing throughout by 2π gives

$$\rho_{(pu)}(t) = \int f_s.dt \tag{4.38}$$

The discretised equation can now be written using a backward approximation technique as,

$$\rho[k] = \rho[k-1] + T_s f_b f_{s(pu)}[k] \tag{4.39}$$

Thus 4.36 and 4.39 are the required equations for the current model of induction motor in discrete per unitised form.

4.7 Phase voltage calculation

The estimation of the flux using either of the estimation schemes discussed requires the knowledge of the instantaneous phase voltages of the motor. This is calculated using the sensed value of the DC bus voltage and the d and q axis reference voltages to the inverter. If the inverter is assumed to be having a constant gain G_i, then the input d and q axis voltages of the motor can be obtained by multiplying the reference values with the gain. Knowing the values of these voltages, the phase voltages can be calculated using the following equations for transformation from the dq reference frame to the stator reference frame.

$$v_{sa} = \frac{2}{3}[v_{sd}\cos\rho(t) - v_{sq}\sin\rho(t)] \tag{4.40}$$

$$v_{sb} = -\frac{1}{3}[v_{sd}\cos\rho(t) - v_{sq}\sin\rho(t)] + \frac{1}{\sqrt{3}}[v_{sq}\cos\rho(t) + v_{sd}\sin\rho(t)] \tag{4.41}$$

$$v_{sc} = -\frac{1}{3}[v_{sd}\cos\rho(t) - v_{sq}\sin\rho(t)] - \frac{1}{\sqrt{3}}[v_{sq}\cos\rho(t) + v_{sd}\sin\rho(t)] \tag{4.42}$$

where v_{sa}, v_{sb} and v_{sc} denote the a, b and c phase voltages while v_{sd} and v_{sq} denote the d and q axis stator voltages.

4.8 Implementation of estimation algorithms

The different algorithms for speed and flux estimation in sensorless vector control have been discussed in Sec. 2.7. In the following subsections, the discrete, per

unitised equations for these algorithms that are to be implemented on the control platform are derived.

4.8.1 Flux estimation algorithm I

The equations for estimating the alpha axis rotor flux will be derived here. The equations for the beta axis can be derived in an exact simlar fashion.
The alpha axis backemf can be written as

$$e_{b\alpha} = v_{s\alpha} - R_s i_{s\alpha} \tag{4.43}$$

The above equation can be discretised and per unitised as

$$e_{s\alpha}[k] = v_{s\alpha}[k] - R_s i_{s\alpha}[k] \tag{4.44}$$

$$e_{s\alpha(pu)}[k] = v_{s\alpha(pu)}[k] - \tfrac{R_s I_b}{V_b} i_{s\alpha(pu)}[k] \tag{4.45}$$

Then the α axis stator flux is obtained by integrating the backemf followed by subsequent high pass filtering. In pu, this is given as

$$\psi_{\alpha i(pu)}[k] = \psi_{s\alpha(pu)}[k-1] + \frac{V_b T_s}{L_m I_b} \frac{\Big(e_{s\alpha(pu)}[k] + e_{s\alpha(pu)}[k-1]\Big)}{2} \tag{4.46}$$

where $\psi_{\alpha i}$ denotes the output of the pure integrator for the alpha axis.

High pass filter The high pass filter has a transfer function, $H(s) = \frac{s}{s+\omega_c}$. This is represented by the differential equation given as

$$\frac{dr(t)}{dt} - \frac{dy(t)}{dt} = \omega_c y(t) \tag{4.47}$$

This equation is discretised in the following manner.

$$\frac{r[k] - r[k-1]}{T_s} = \omega_c y[k] + \frac{y[k] - y[k-1]}{T_s} \tag{4.48}$$

$$\implies y[k] = \frac{1}{1 + \omega_c T_s}(r[k] - r[k-1] + y[k-1]) \tag{4.49}$$

where y[k] denotes the output of the filter for an input, r[k].

Rotor flux from stator flux From the estimated value of stator flux, the alpha axis rotor flux can now be calculated by using 2.70. Discretising and perunitising the equation gives,

$$\psi_{r\alpha(pu)}[k] = -\frac{L_s L_r - L_m^2}{L_m^2} i_{s\alpha(pu)}[k] + \frac{L_r}{L_m}\psi_{s\alpha(pu)}[k] \tag{4.50}$$

An exact similar procedure can be followed with the β axis quantities to get the following equations for estimating the β axis rotor flux

$$\begin{aligned}
e_{s\beta(pu)}[k] &= v_{s\beta(pu)}[k] - \frac{R_s I_b}{V_b} i_{s\beta(pu)}[k] \\
\psi_{\beta i(pu)}[k] &= \psi_{s\beta(pu)}[k-1] + \frac{V_b T_s}{L_m I_b} \frac{\Big(e_{s\beta(pu)}[k] + e_{s\beta(pu)}[k-1]\Big)}{2} \\
\psi_{r\beta(pu)}[k] &= -\frac{L_s L_r - L_m^2}{L_m^2} i_{s\beta(pu)}[k] + \frac{L_r}{L_m}\psi_{s\beta(pu)}[k]
\end{aligned}$$

4.8.2 Flux estimation algorithm II

The equations to be implemented for this improved flux estimation scheme are given in 2.78 and 2.79.

Discretisation The equations can be written in discrete form in the following manner. Define the alpha and beta axis backemf terms as

$$e_{s\alpha}[k] = v_{s\alpha}[k] - R_s i_{s\alpha}[k] + offset_\alpha[k] \tag{4.51}$$

$$e_{s\beta}[k] = v_{s\beta}[k] - R_s i_{s\beta}[k] + offset_\beta[k] \tag{4.52}$$

where $offset_\alpha = K(\psi^{\sim}_{r\alpha} - \psi^{*}_{r\alpha})$ and $offset_\beta = K(\psi^{\sim}_{r\beta} - \psi^{*}_{r\beta})$. Then the equations for stator flux and rotor flux can be written as

$$\psi^{\sim}_{s\alpha}[k] = \psi^{\sim}_{s\alpha}[k-1] + \frac{T_s}{2}(e_{s\alpha}[k] + e_{s\alpha}[k-1]) \tag{4.53}$$

$$\psi^{\sim}_{s\beta}[k] = \psi^{\sim}_{s\beta}[k-1] + \frac{T_s}{2}(e_{s\beta}[k] + e_{s\beta}[k-1]) \tag{4.54}$$

$$\psi^{\sim}_{r\alpha}[k] = \frac{L_r}{L_m}\psi^{\sim}_{s\alpha}[k] - \frac{L_s L_r - L_m^2}{L_m} i_{s\alpha}[k] \tag{4.55}$$

$$\psi^{\sim}_{r\beta}[k] = \frac{L_r}{L_m}\psi^{\sim}_{s\beta}[k] - \frac{L_s L_r - L_m^2}{L_m} i_{s\beta}[k] \tag{4.56}$$

Now $\cos\rho$ and $\sin\rho$ can be obtained as

$$\cos\rho[k] = \frac{\psi^{\sim}_{r\alpha}[k]}{\sqrt{\psi^{\sim}_{r\alpha}[k]^2 + \psi^{\sim}_{r\beta}[k]^2}} \tag{4.57}$$

$$\cos\rho[k] = \frac{\psi^{\sim}_{r\alpha}[k]}{\sqrt{\psi^{\sim}_{r\alpha}[k]^2 + \psi^{\sim}_{r\beta}[k]^2}} \tag{4.58}$$

$$\tag{4.59}$$

The calculated value of the rotor flux for error correction can then be given as

$$|\psi^{*}_{r}[k]| = \sqrt{L_m(i_{s\alpha}[k]\psi^{\sim}_{r\alpha}[k] + i_{s\beta}[k]\psi^{\sim}_{r\beta}[k])} \tag{4.60}$$

$$\psi^{*}_{r\alpha}[k]| = |\psi^{*}_{r}[k]|\cos\rho[k] \tag{4.61}$$

$$\psi^{*}_{r\beta}[k]| = |\psi^{*}_{r}[k]|\sin\rho[k] \tag{4.62}$$

Per unitisation The above discrete equations can now be written on a per unit basis as given:

$$\begin{aligned}
e_{s\alpha(pu)}[k] &= v_{s\alpha(pu)}[k] - \frac{R_s I_b}{V_b} i_{s\alpha(pu)}[k] + \frac{K\psi_b}{V_b}(\psi^{*}_{r\alpha(pu)}[k] - \psi^{\sim}_{r\alpha(pu)}[k]) \\
e_{s\beta(pu)}[k] &= v_{s\beta(pu)}[k] - \frac{R_s I_b}{V_b} i_{s\beta(pu)}[k] + \frac{K\psi_b}{V_b}(\psi^{*}_{r\beta(pu)}[k] - \psi^{\sim}_{r\beta(pu)}[k]) \\
\psi^{\sim}_{s\alpha(pu)}[k] &= \psi^{\sim}_{s\alpha(pu)}[k-1] + \frac{T_s V_b}{2L_m I_b}(e_{s\alpha(pu)}[k] + e_{s\alpha(pu)}[k-1]) \\
\psi^{\sim}_{s\beta(pu)}[k] &= \psi^{\sim}_{s\beta(pu)}[k-1] + \frac{T_s V_b}{2L_m I_b}(e_{s\beta(pu)}[k] + e_{s\beta(pu)}[k-1]) \\
\psi^{\sim}_{r\alpha(pu)}[k] &= \frac{L_r}{L_m}\psi^{\sim}_{s\alpha(pu)}[k] - \frac{L_s L_r - L_m^2}{L_m^2} i_{s\alpha(pu)}[k] \\
\psi^{\sim}_{r\beta(pu)}[k] &= \frac{L_r}{L_m}\psi^{\sim}_{s\beta(pu)}[k] - \frac{L_s L_r - L_m^2}{L_m^2} i_{s\beta(pu)}[k] \\
\psi^{*}_{r(pu)}[k] &= \sqrt{i_{s\alpha(pu)}[k]\psi_{r\alpha(pu)}[k] + i_{s\beta(pu)}[k]\psi_{r\beta(pu)}[k]} \\
\psi^{*}_{r\alpha(pu)}[k] &= \psi^{*}_{r(pu)}[k]\cos\rho[k] \\
\psi^{*}_{r\beta(pu)}[k] &= \psi^{*}_{r(pu)}[k]\sin\rho[k]
\end{aligned}$$

4.8.3 Speed estimation algorithm

The equations necessary for implementing the speed estimation algorithm are given in Eq.(2.80) and Eq.(2.82). These equations can be implemented in discrete

form as

$$\begin{aligned} \omega_{mr}[k] &= \cos\theta[k]\Big[\frac{\sin\theta[k]-\sin\theta[k-1]}{T_s}\Big] - \sin\theta[k]\Big[\frac{\cos\theta[k]-\cos\theta[k-1]}{T_s}\Big] \\ \implies \omega_{mr(pu)}[k] &= \cos\theta[k]\Big[\frac{\sin\theta[k]-\sin\theta[k-1]}{T_s\omega_b}\Big] - \sin\theta[k]\Big[\frac{\cos\theta[k]-\cos\theta[k-1]}{T_s\omega_b}\Big] \end{aligned}$$

Now, the actual speed in pu can be estimated using 2.48 as

$$\omega_{pu}[k] = \omega_{mr(pu)}[k] - \frac{i_{sq(pu)}[k]}{\tau_r i_{mr(pu)}[k]} \tag{4.63}$$

4.9 Low pass filter implementation

The implementation of vector control with a PWM inverter causes switching frequency noise in different parts of the system. The power supply used can also introduce significant switching noise into the system. Therefore, the use of appropriate low pass filters can remove these noise and help in improving the performance of the system.

The transfer function of a general low pass filter with a cutoff frequency of ω_c rad/s can be written as $H(s) = \frac{\omega_c}{s+\omega_c}$. Thus the input-output relation can be represented by a first order differential equation as

$$r(t) - y(t) = \tau_c \frac{dy(t)}{dt} \tag{4.64}$$

where r(t) and y(t) denotes the input and output signals to the filter respectively, and $\tau_c = \frac{1}{\omega_c}$ is the filter time constant.
Eqn. 4.64 can be written in discrete form as

$$\begin{aligned} \tfrac{y[k]-y[k-1]}{T_s} &= \tfrac{1}{\tau_c}(r[k]-y[k]) \\ \implies y[k] &= \tfrac{\tau_c}{\tau_c+T_s}y[k-1] + \tfrac{T_s}{\tau_c+T_s}r[k] \end{aligned}$$

Since the filter input and output signals are the same physical quantity, the equations in the pu form will also have the same form.

4.10 Conclusion

This chapter presented the design of the vector control system. The design of the PI controllers and the various blocks for estimation and control, used in the vector control system is described in detail and the equations have been presented in a discrete per unit form suitable for digital implementation on the TMS320F28335. In the next chapter the results obtained from the simulation and hardware implementation will be presented and discussed.

CHAPTER 5

RESULTS AND INFERENCES

5.1 Simulation Results

The simulation of sensored and sensorless vector control is done in SIMULINK using the model of a 1MW induction machine whose parameters and ratings have been specified by BHEL. The results obtained are presented in the following sections. The machine ratings and parameters are given in Table 5.1 and 5.2.

Table 5.1: Ratings for the 1 MW motor

Parameter	**Value**
Power	1 MW
Voltage	690 V
Current	1045 A
Power factor	0.8
Connection	Star
Speed	1488 rpm
Rotor type	Squirrel Cage

Table 5.2: Model parameters

R_s	$R_r^{'}$	L_{ls}	L_{lr}	L_m	J
0.00163 Ω	0.0030 Ω	0.2486 mH	0.1276 mH	4.374 mH	42 $kg-m^2$

The design of the controllers and the limiter values have been done following the procedure outlined in Chapter 4 for the 30kW machine. The values obtained from these are given in Table 5.3.

Table 5.3: Controller parameters

Controller	$f_b(Hz)$	K_p	K_i	U_{max}	U_{min}
i_{sd}	200	1.49×10^{-4}	6.52×10^{-4}	0.28	-0.28
i_{sq}	200	1.49×10^{-4}	6.52×10^{-4}	0.89	-0.89
i_{mr}	2	3.008	2	560	-560
ω_m	1	267.1	0.38168	2092	-2092

5.1.1 Sensored Vector Control

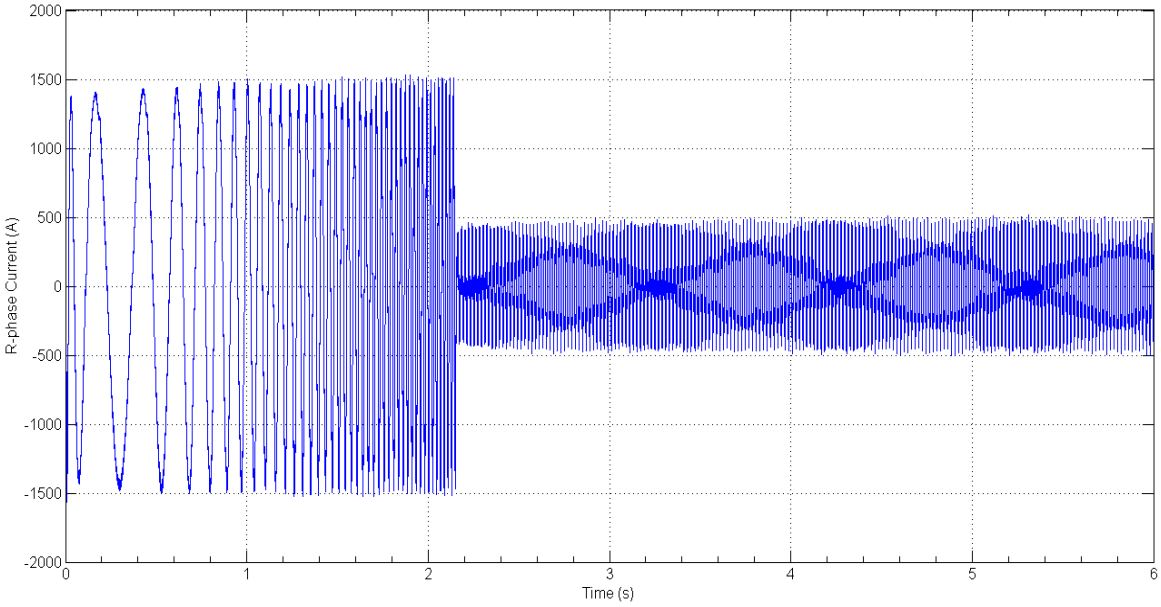

Figure 5.1: *Simulation result*: R-phase current profile during starting *(Scale: X-axis: 1.0 s/div, Y-axis: 500 A/div)*

Fig. 5.1 shows the simulated starting current profile in sensored vector control. Full load current is drawn till the reference speed is reached.

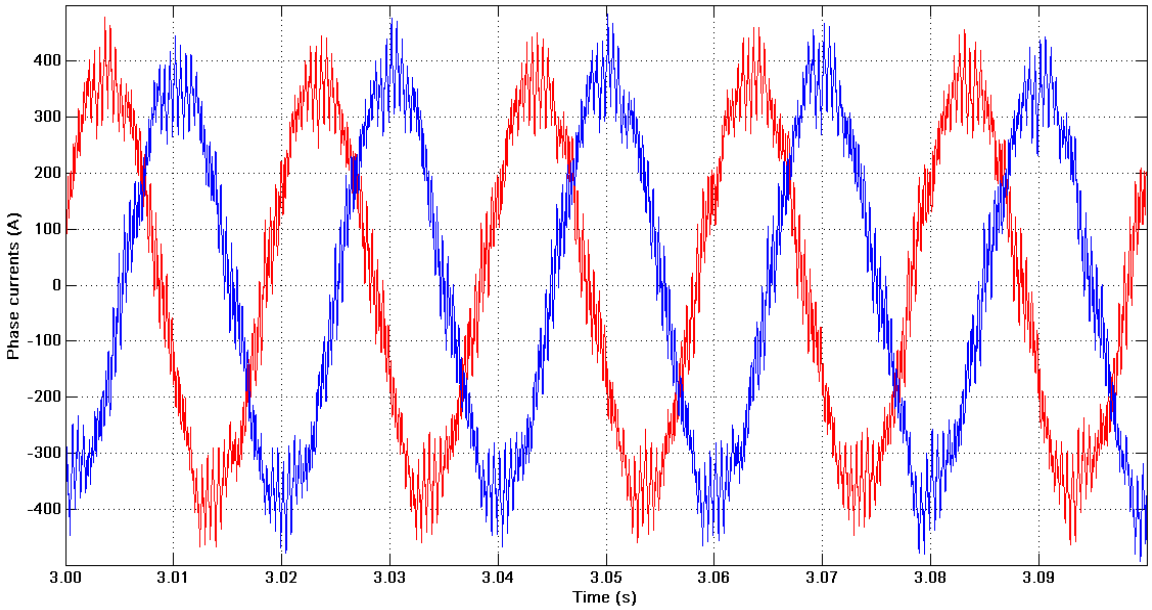

Figure 5.2: *Simulation result*: R(red) and Y(blue) phase currents at steady state *(Scale: X-axis: 10.0 ms/div, Y-axis: 100 A/div)*

Fig. 5.2 shows the simulated R and Y phase currents at no load, steady state with sensored vector control.

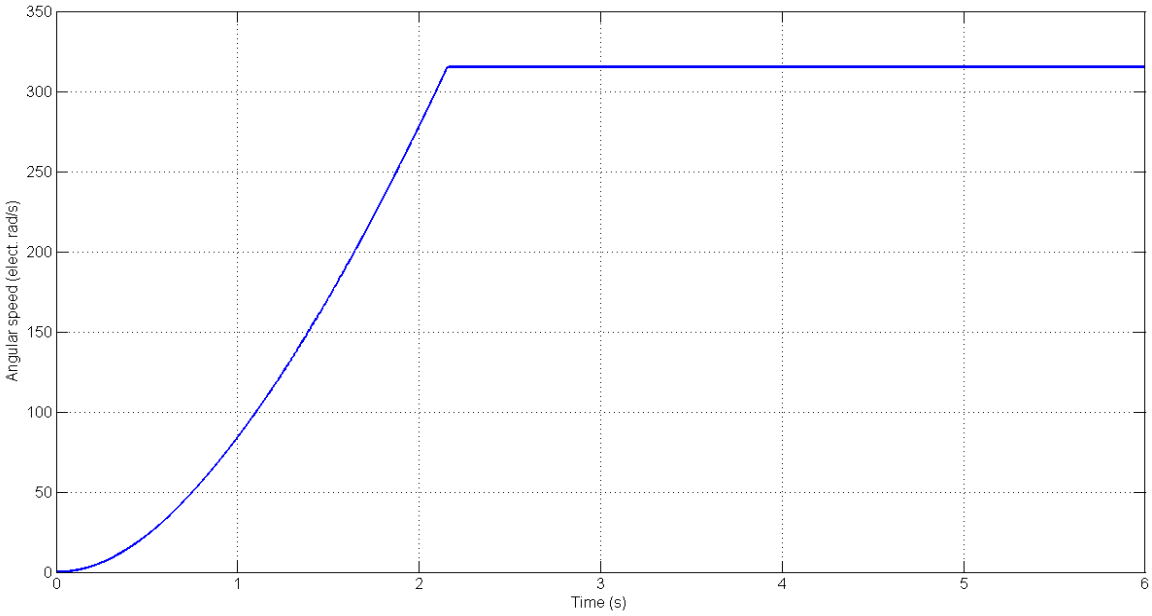

Figure 5.3: *Simulation result*: Shaft speed during starting for a reference of 50 Hz *(Scale: X-axis: 1.0 s/div, Y-axis: 50 elect.rad/s/div)*

Fig. 5.3 shows the simulated speed profile for starting with a sensored vector control with a reference speed of rated value.

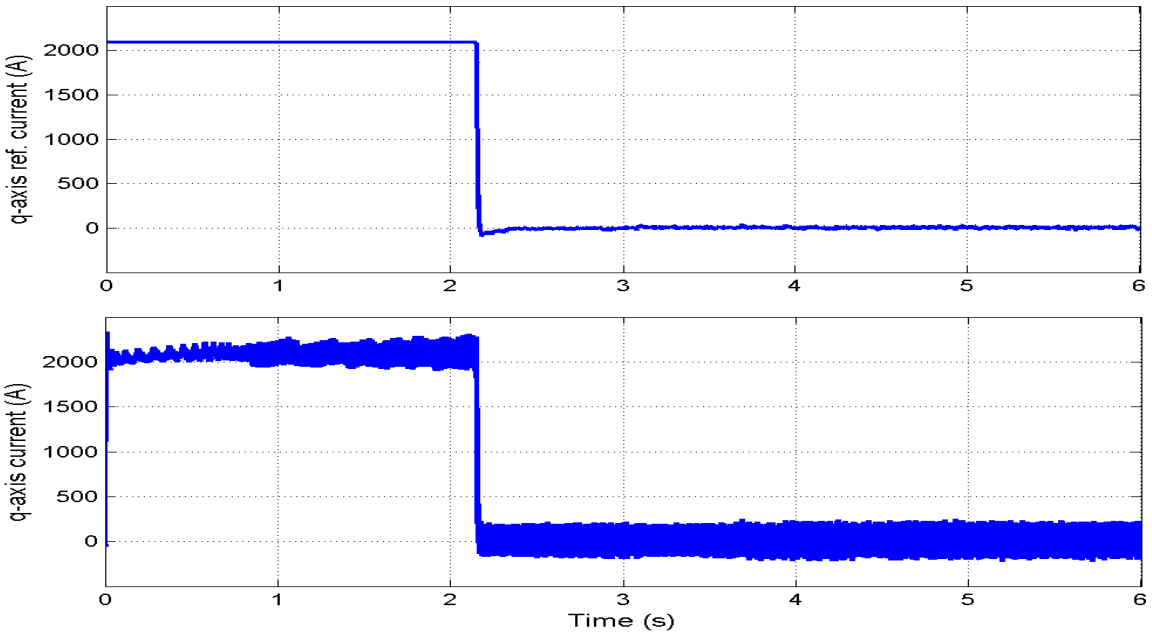

Figure 5.4: *Simulation result*: q-axis reference(top) and actual(bottom) current waveforms during starting *(Scale: X-axis: 1.0 s/div, Y-axis: 500 A/div)*

Fig. 5.4 shows the simulated reference and feedback values of the q-axis current. The q-axis current remains at its rated value till speed reference is reached.

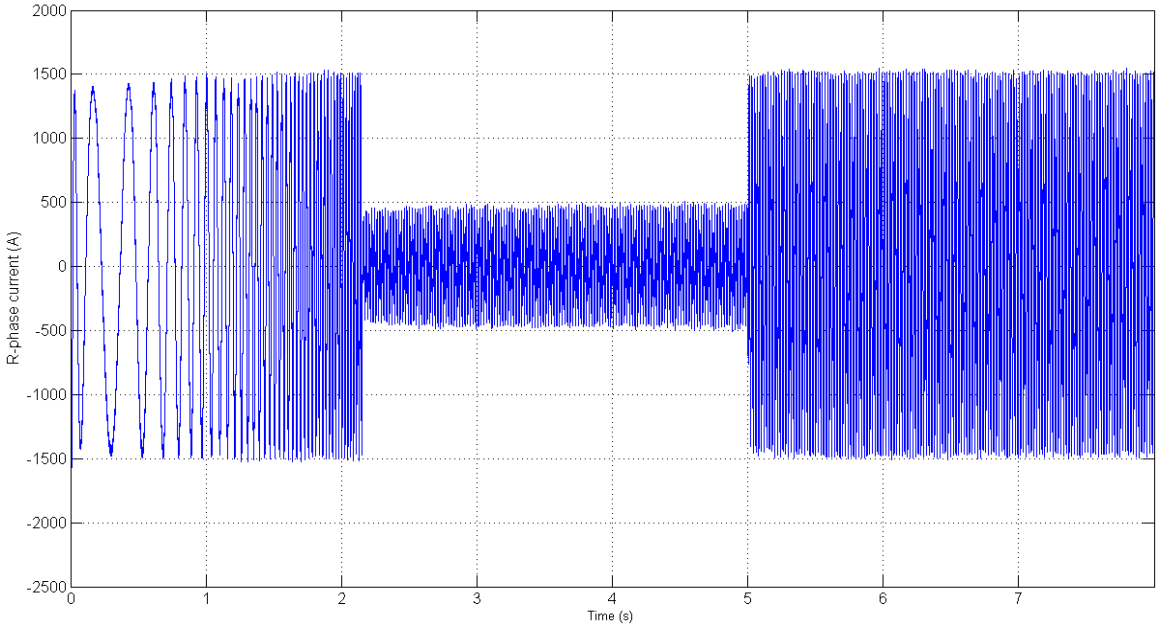

Figure 5.5: *Simulation result*: Current profile for a step change in load torque *(Scale: X-axis: 1.0 s/div, Y-axis: 500 A/div)*

Fig. 5.5 shows the simulated response of the phase current to a step change in load torque of rated value applied at t=5 s. The phase current immediately rises to the full rated value so as to meet the load torque.

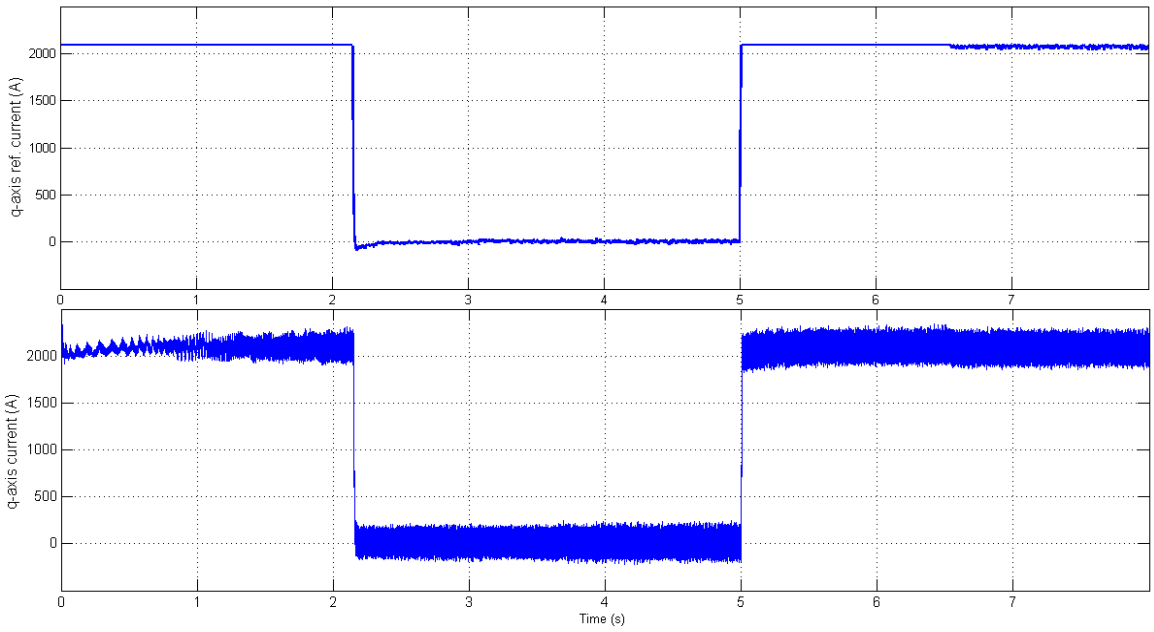

Figure 5.6: *Simulation result*: i^*_{sq}(top) and i_{sq}(bottom) currents for a step change in load torque *(Scale: X-axis: 1.0 s/div, Y-axis: 500 A/div)*

Fig. 5.6 shows the simulated response of i^*_{sq} and i_{sq} to a step change in load torque of rated value applied at t=5 s. The q-axis current immediately rises to the rated value to meet the load torque demand.

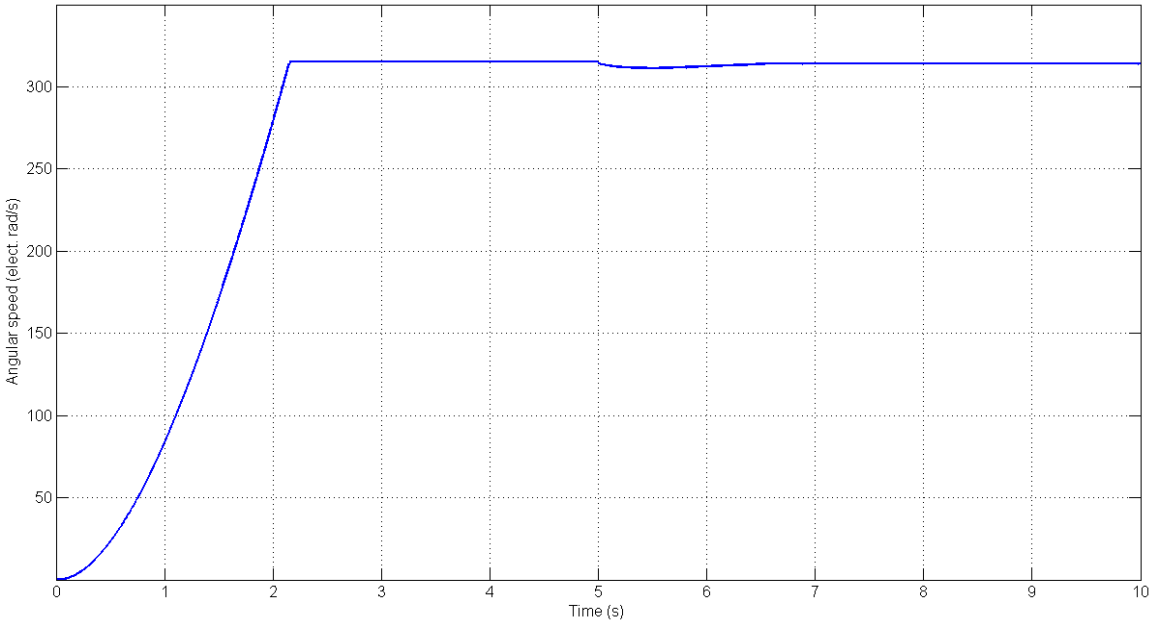

Figure 5.7: *Simulation result*: Speed response for sudden full load torque application *(Scale: X-axis: 1.0 s/div, Y-axis: 50 elect.rad/s/div)*

Fig. 5.7 shows the simulated speed response when a sudden full load torque is applied at t=5 s. It is seen that there is only a small dip in speed at the instant of applying torque.

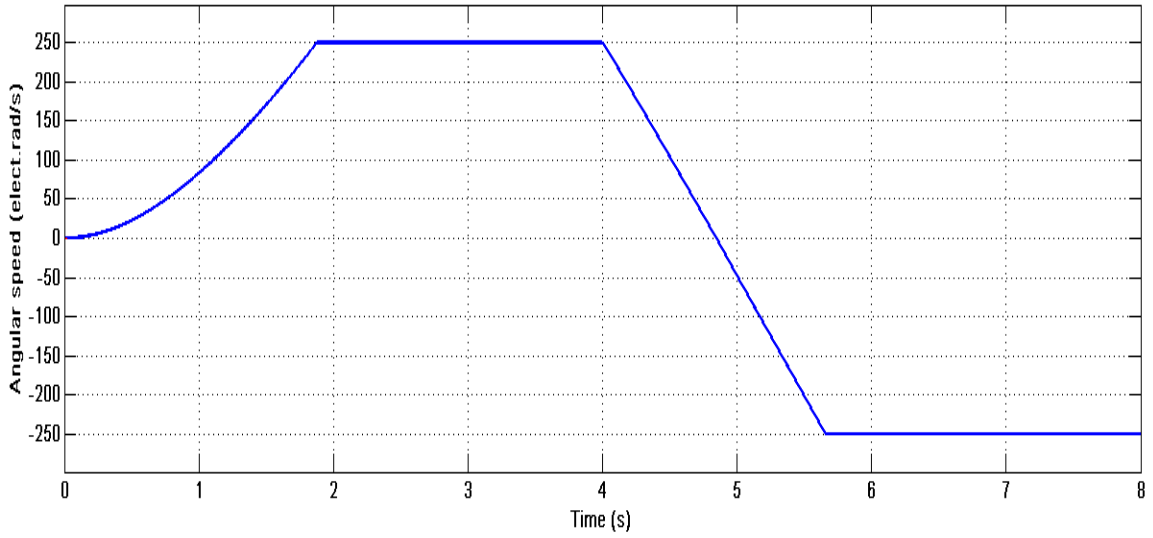

Figure 5.8: *Simulation result*: Response for a speed reversal command *(Scale: X-axis: 1.0 s/div, Y-axis: 50 elect.rad/s/div)*

Fig. 5.8 shows the simulated speed response for a speed reversal command from 250 rad/s to -250 rad/s at t=4 s.

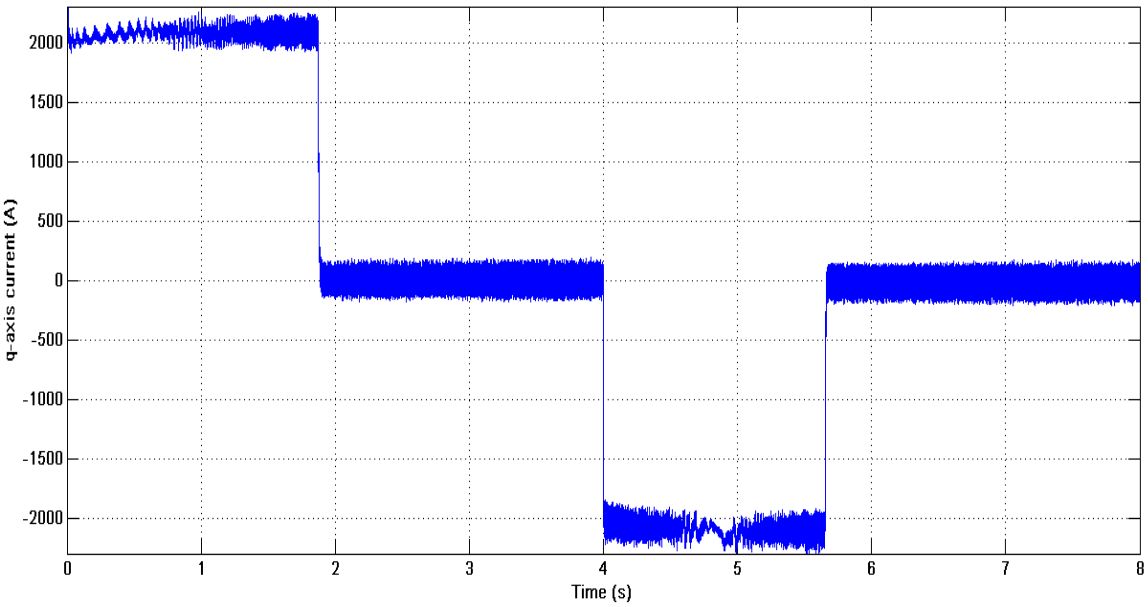

Figure 5.9: *Simulation result*: q-axis current response for the speed reversal command *(Scale: X-axis: 1 s/div, Y-axis: 500 A/div)*

Fig. 5.9 shows the simulated response of i^*_{sq} and i_{sq} during the speed reversal operation shown in Fig. 5.8. During reversal, i_{sq} goes to the negative maximum value indicating that drive is in regeneration mode.

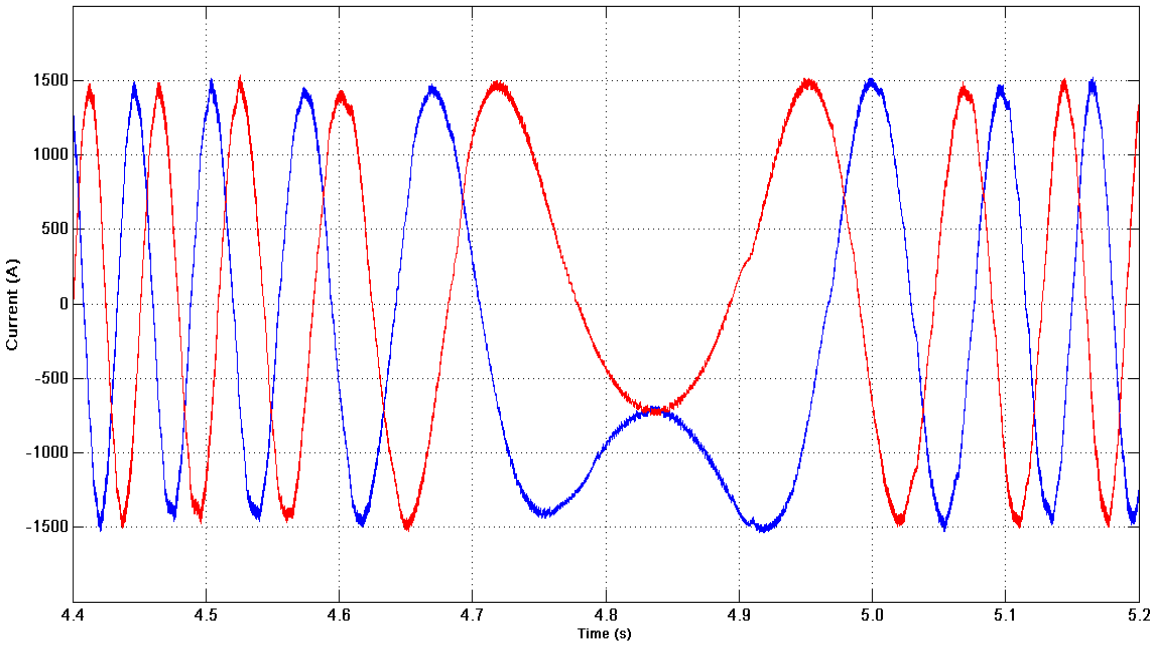

Figure 5.10: *Simulation result*: R(blue) and Y(red) phase currents during speed reversal operation *(Scale: X-axis: 100.0 ms/div, Y-axis: 500 A/div)*

Fig. 5.10 shows the simulated waveforms of the R-phase and Y-phase currents during the speed reversal operation shown in Fig. 5.8. The change in frequency and phase sequence during the reversal can be observed.

5.1.2 Sensorless Vector Control

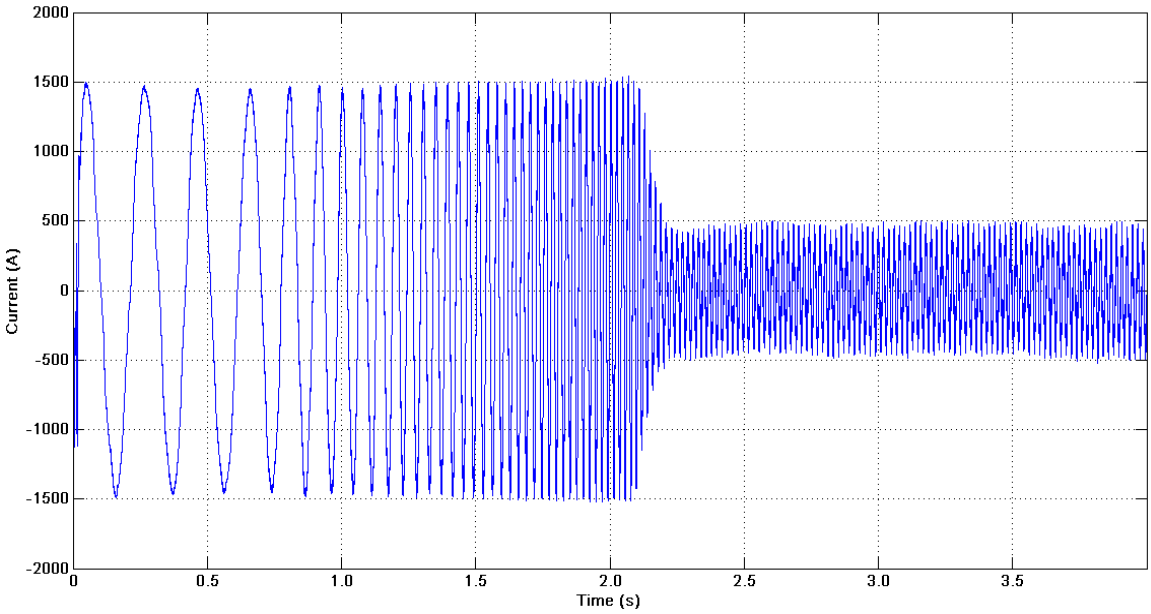

Figure 5.11: *Simulation result*: R-phase current profile during starting *(Scale: X-axis: 500 ms/div, Y-axis: 500 A/div)*

Fig. 5.11 shows the simulated starting current profile in sensorless vector control. Full load current is drawn till the reference speed is reached.

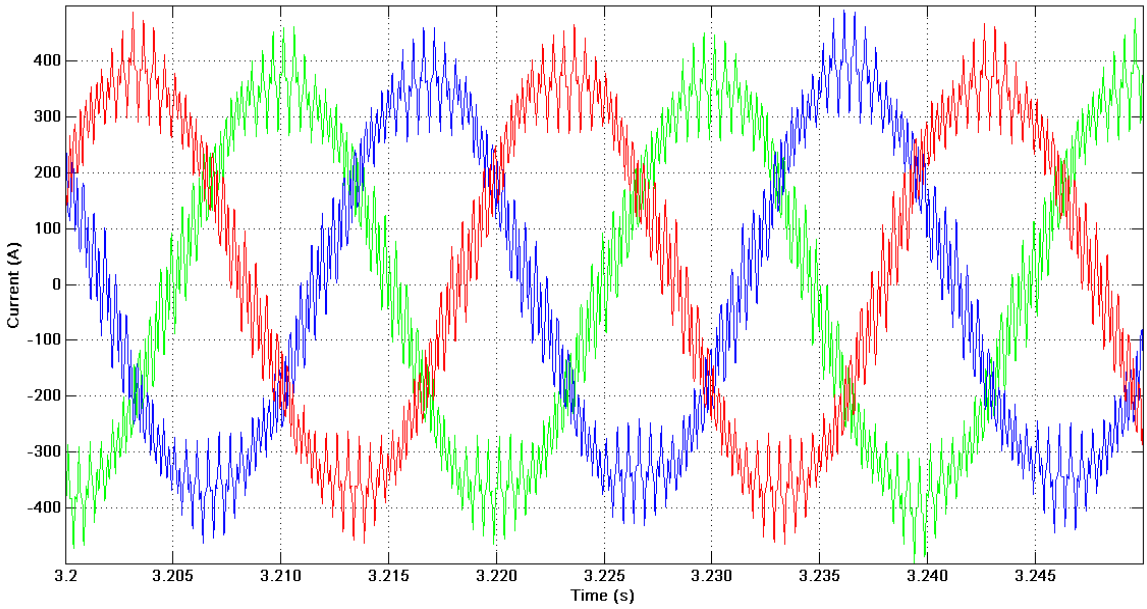

Figure 5.12: *Simulation result*: Steady state current waveforms for no load steady state at rated speed *(Scale: X-axis: 5 ms/div, Y-axis: 100 A/div)*

Fig. 5.12 shows the simulated three phase input currents at no load, steady state for sensorless vector control.

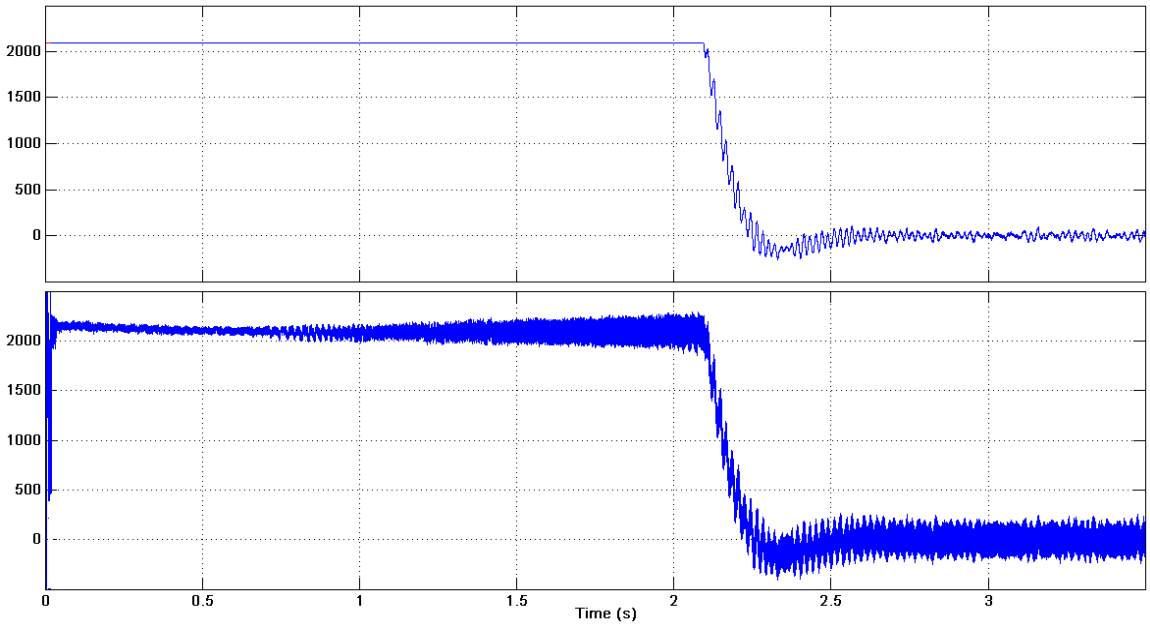

Figure 5.13: *Simulation result*: q-axis reference current and actual currents during starting *(Scale: X-axis: 500 ms/div, Y-axis: 500 A/div)*

Fig.5.13 shows the simulated response of i^*_{sq} and i_{sq} during starting with sensorless vector control. Maximum rated value of i_{sq} is drawn till reference speed is reached.

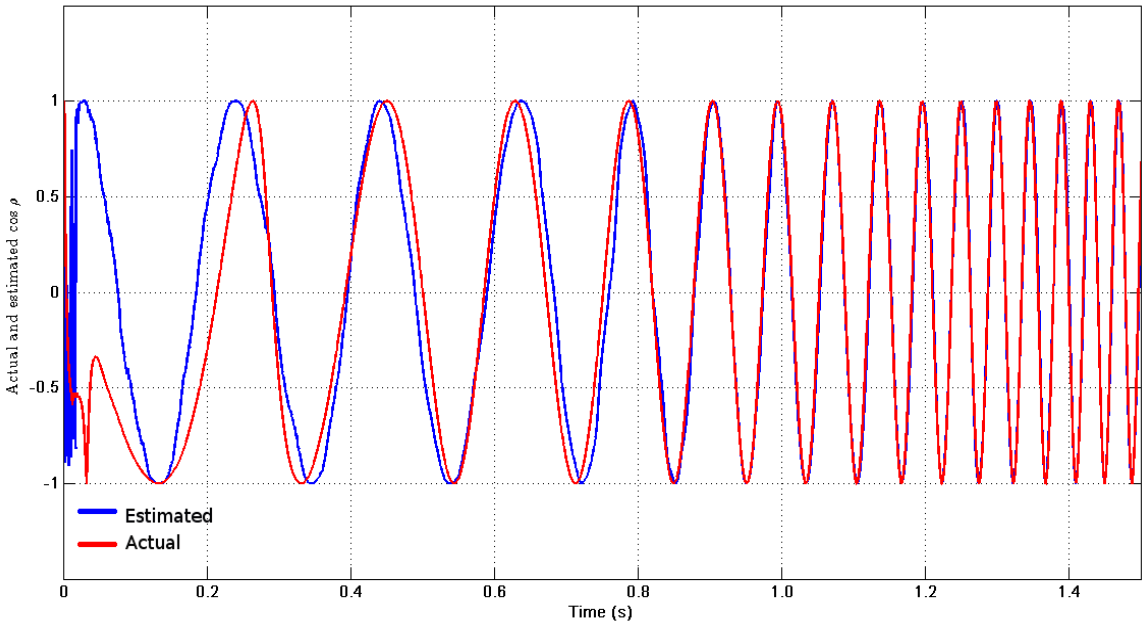

Figure 5.14: *Simulation result*: Actual and estimated values of $\cos\rho$ at starting *(Scale: X-axis: 200 ms/div, Y-axis: 0.05/div)*

Fig.5.14 shows the actual and estimated values of $\cos\rho$ at starting. It is seen that there is a larger error in estimation at starting and low speeds and the error decreases as the speed increases.

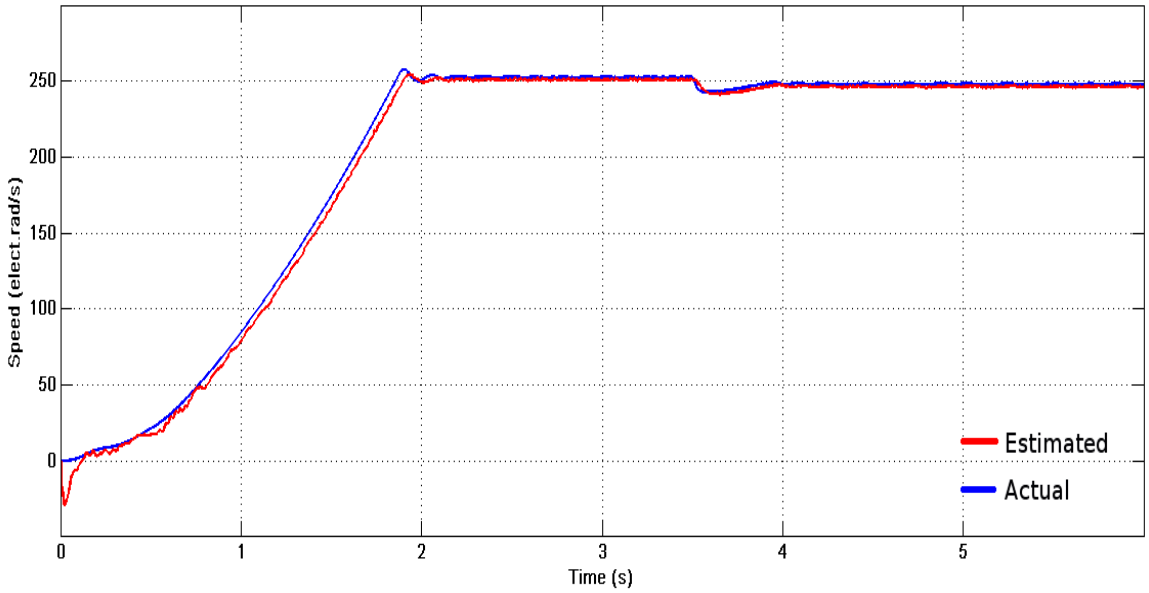

Figure 5.15: *Simulation result*: Actual and estimated speed *(Scale: X-axis: 1 s/div, Y-axis: 50 elect.rad/s/div)*

Fig.5.15 shows the simulated waveforms of actual and estimated speed during starting with a speed reference of 250 elect.rad/s and applying a step load torque of rated value at t=3.5 s.

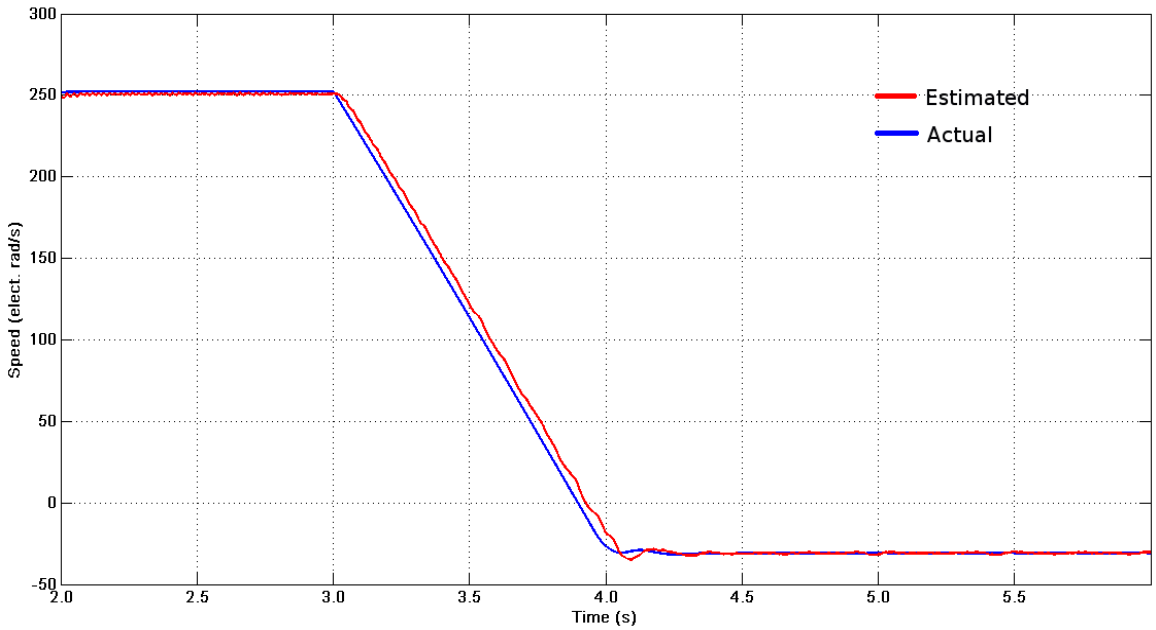

Figure 5.16: *Simulation result*: Actual and estimated values of speed *(Scale: X-axis: 500 ms/div, Y-axis: 50 elect.rad/s/div)*

Fig.5.16 shows the simulated waveforms of actual and estimated shaft speed during a speed reversal command at t=3 s from 250 elect. rad/s to a low speed operation of -5 Hz frequency.

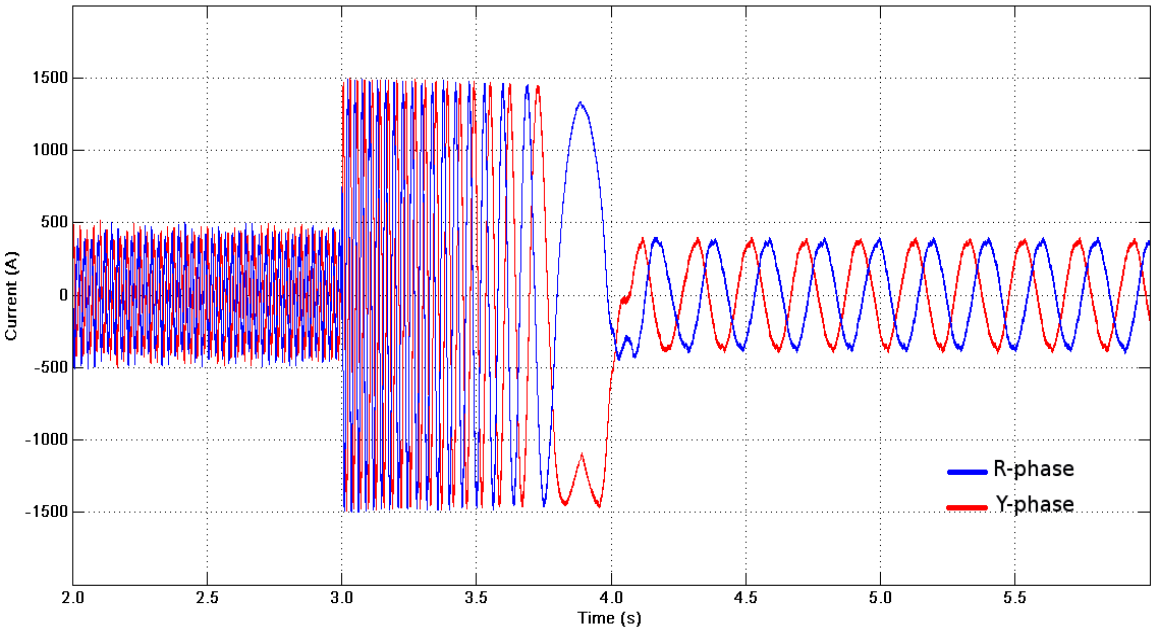

Figure 5.17: *Simulation result*: Phase currents during speed reversal and low speed operation *(Scale: X-axis: 500 ms/div, Y-axis: 500 A/div)*

Fig.5.17 shows the simulated waveforms of the R and Y phase currents during the speed reversal and subsequent 5 Hz operation shown in Fig.5.16. The variation in frequency and the change in phase sequence during the reversal can be observed.

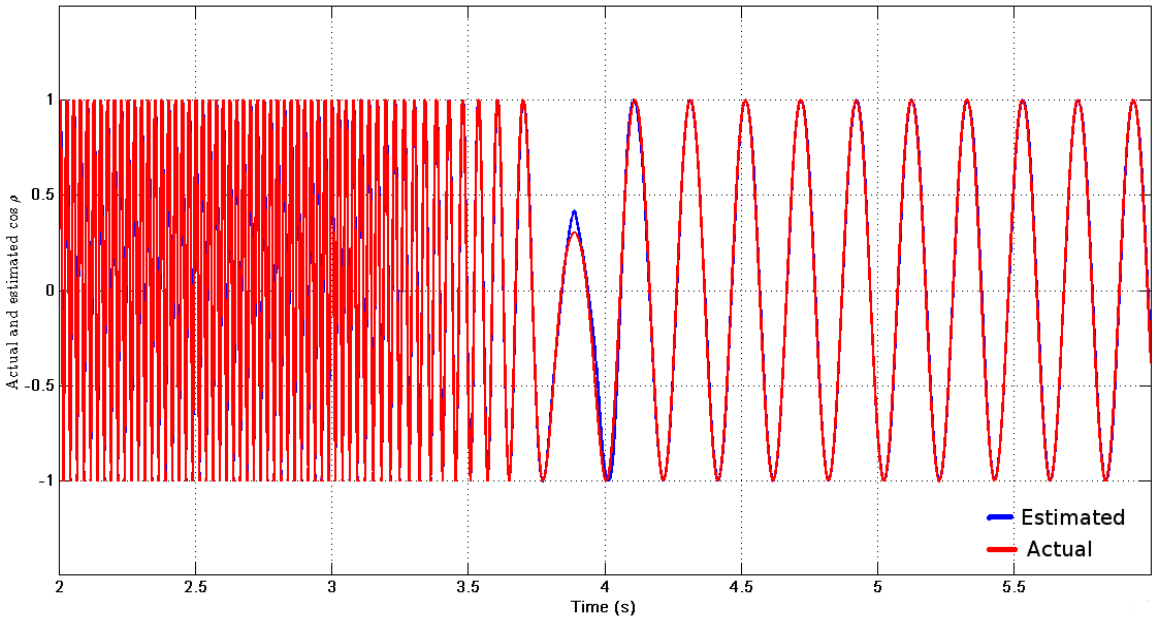

Figure 5.18: *Simulation result*: Actual and estimated $\cos\rho$ *(Scale: X-axis: 500 ms/div, Y-axis: 0.5/div)*

Fig.5.18 shows the simulated waveforms of actual and estimated $\cos\rho$ during the speed reversal and the low speed operation as shown in Fig.5.16.

5.2 Results from Hardware

5.2.1 Sensored Vector Control

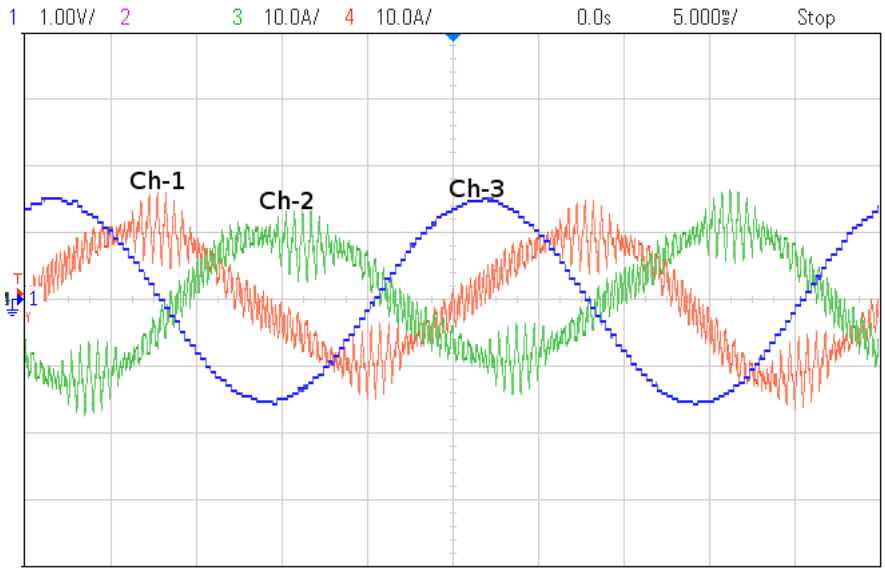

Figure 5.19: *Hardware result*: No load, Steady state waveforms for $\omega_{ref} = 0.8pu$ *(Ch1- R phase current, Ch2- Y phase current, Ch3- R-phase voltage, Scale: X-axis: 5.0 ms/div, Y-axis: Ch1- 10 A/div, Ch2- 10 A/div Ch3- 0.6 pu/div)*

Fig.5.19 shows the oscilloscope waveforms of the phase voltage and phase currents at no load steady state for sensored vector control.

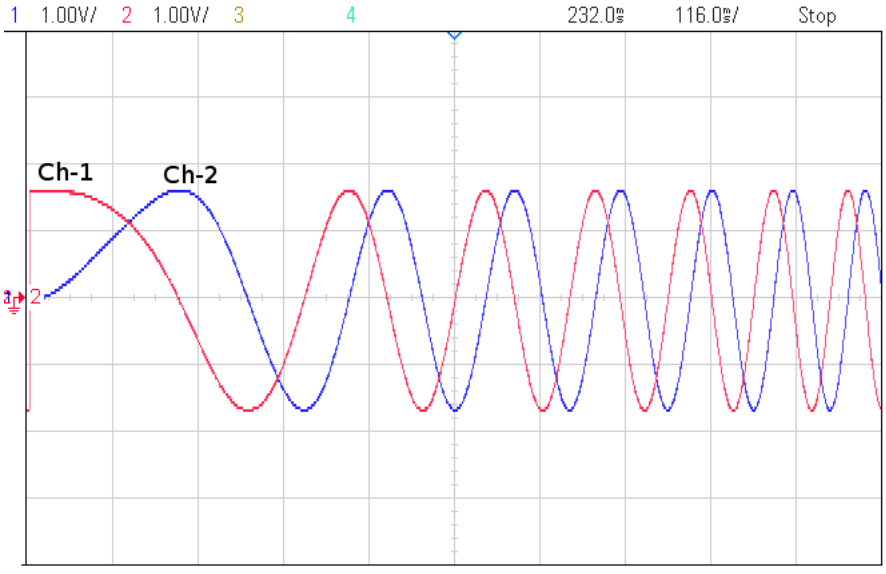

Figure 5.20: *Hardware result*: $\cos\rho$ and $\sin\rho$ waveforms during starting *(Ch1-* $\cos\rho$*, Ch2-* $\sin\rho$*, Scale: X-axis: 116.0 ms/div, Y-axis: 0.6 pu/div)*

Fig.5.20 shows the oscilloscope waveforms of $\sin\rho$ and $\cos\rho$ during starting.

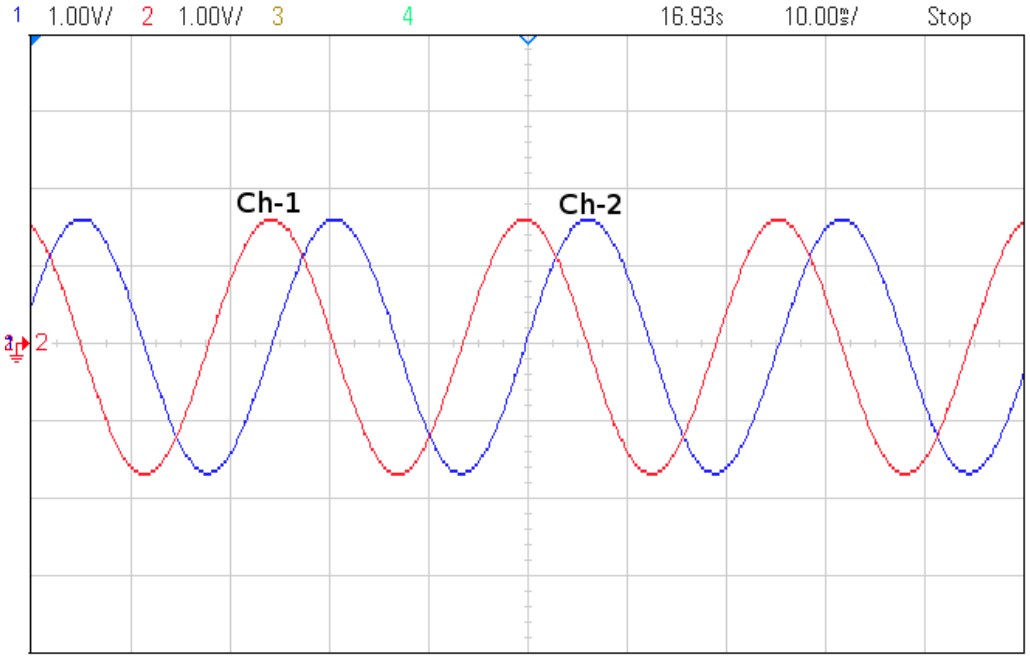

Figure 5.21: *Hardware result*: $\cos\rho$ and $\sin\rho$ waveforms at steady state with 0.8 pu speed *(Ch1-* $\cos\rho$*, Ch2-* $\sin\rho$*, Scale: X-axis: 10.0 ms/div, Y-axis: 0.6 pu/div)*

Fig.5.21 shows the oscilloscope waveforms of $\cos\rho$ and $\sin\rho$ at steady state obtained for sensored vector control.

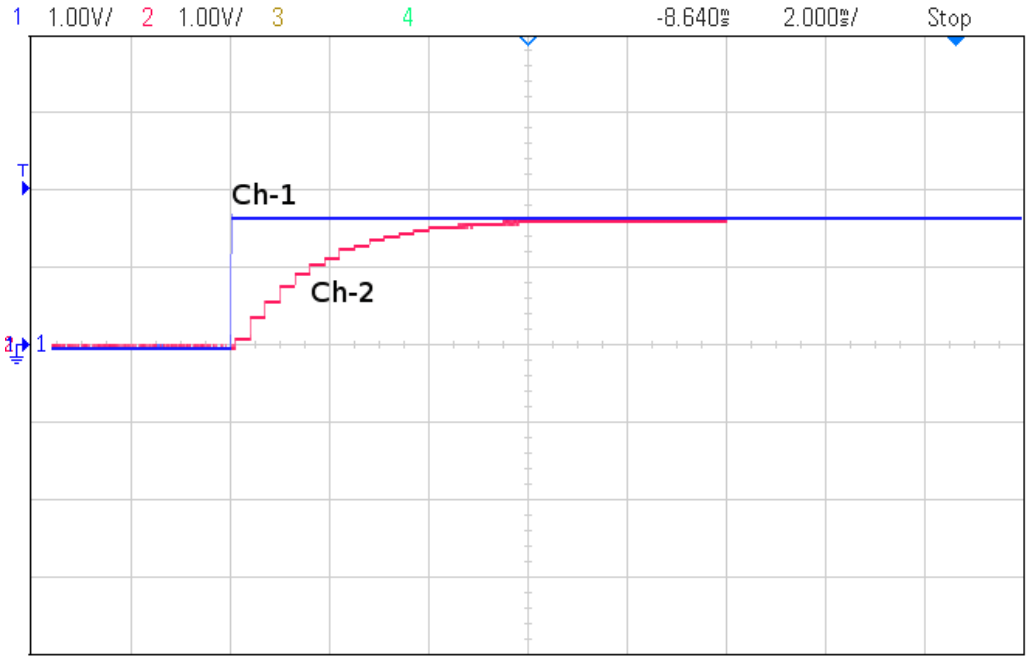

Figure 5.22: *Hardware result*: Step response of the implemented current controllers *(Ch1- Input Step reference , Ch2- Output Response , Scale: X-axis: 2.0 ms/div, Y-axis: 0.6 pu/div)*

Fig.5.22 shows the oscilloscope trace of the step response of the implemented digital PI current controllers of bandwidth 100 Hz.

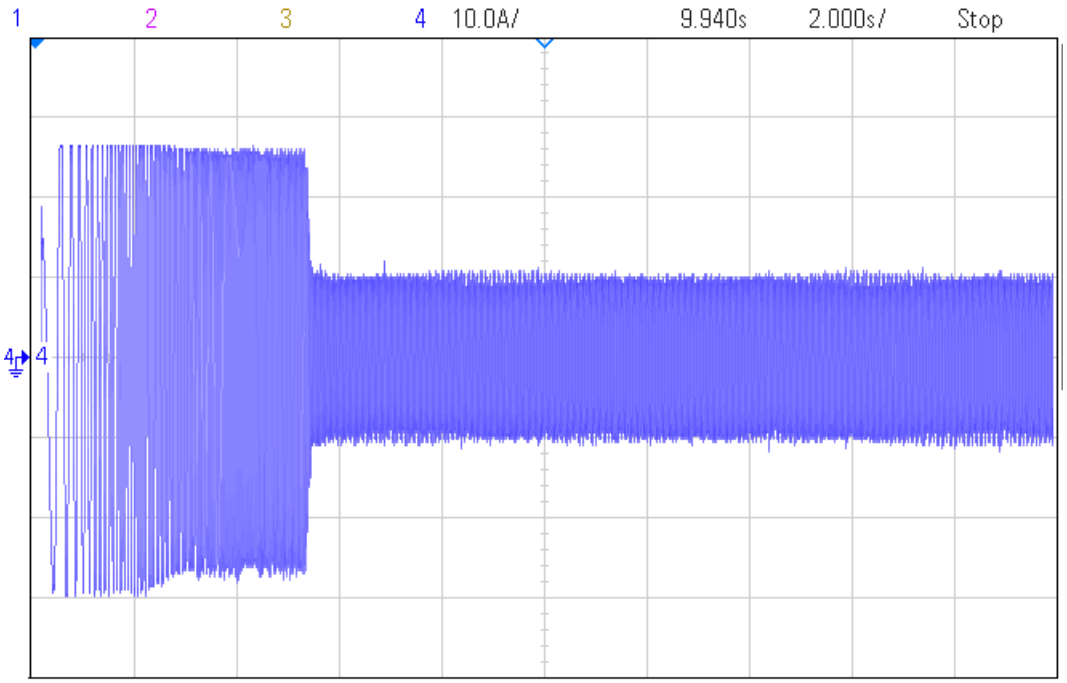

Figure 5.23: *Hardware result*: R-phase current profile *(Scale: X-axis: 2.0 s/div, Y-axis: 10 A/div)*

Fig.5.23 shows the oscilloscope trace of the R-phase current during starting in sensored vector control with a step reference speed of 0.8 pu.

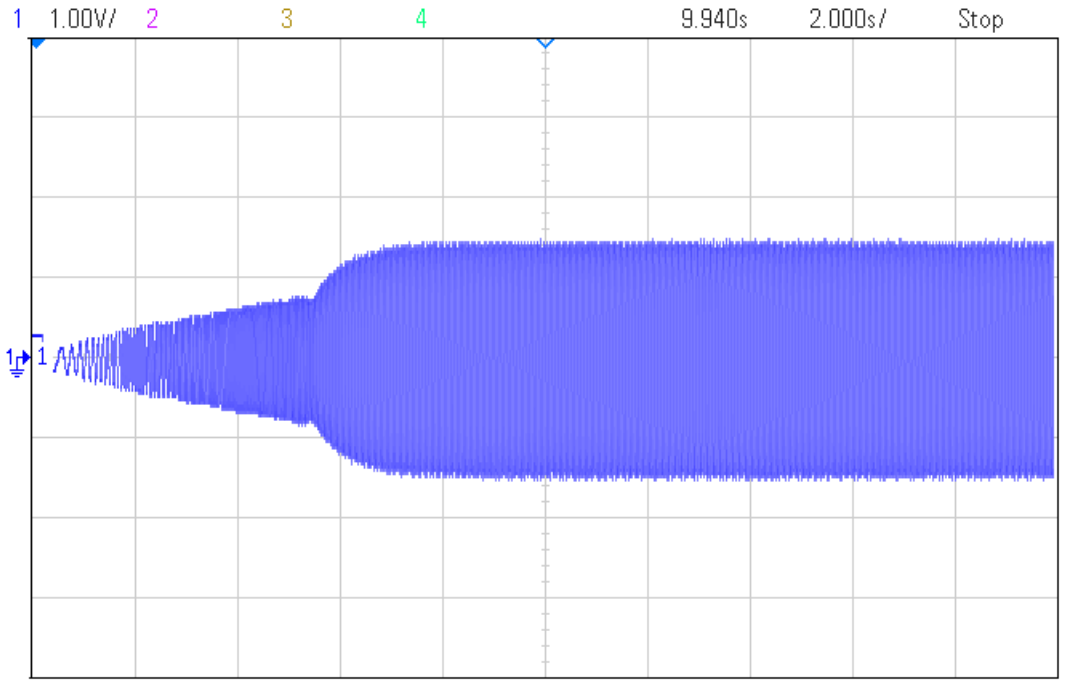

Figure 5.24: *Hardware result*: R-phase voltage profile during starting with a step reference speed of 0.8 pu *(Scale: X-axis: 2.0 s/div, Y-axis: 0.6 pudiv)*

Fig.5.24 shows the oscilloscopic trace of the R-phase voltage obtained during starting in sensored vector control with a speed reference of 0.8 pu.

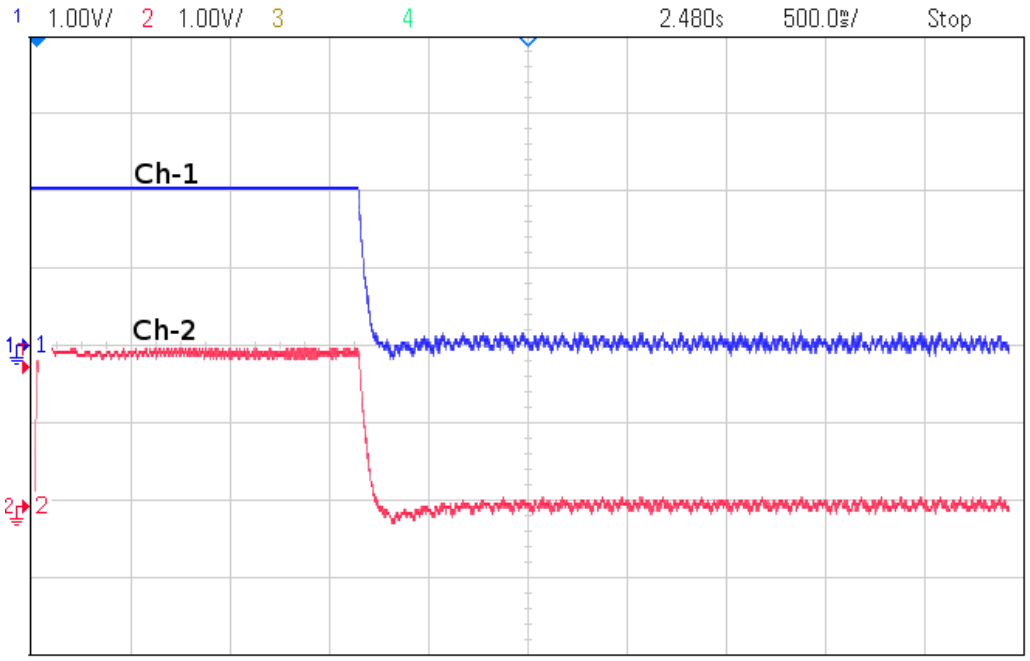

Figure 5.25: *Hardware result*: Reference and actual q axis currents during starting *Ch1-i^*_{sq}, Ch2- i_{sq} (Scale: X-axis: 500 ms/div, Y-axis: 0.6 pu/div)*

Fig.5.25 shows the oscilloscope waveforms of i_{sq} and i^*_{sq} obtained during starting with sensored vector control. i_{sq} is at its maximum during starting and falls to a value close to zero at no load, steady state.

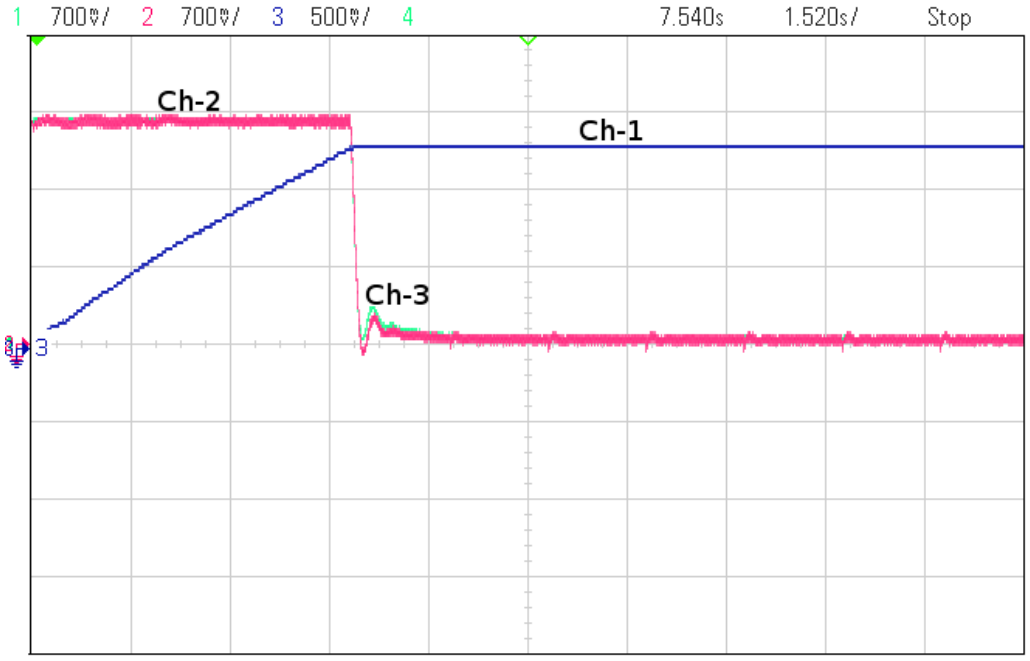

Figure 5.26: *Hardware result*: i_{sq} and ω_m at starting *Ch1- ω_m, Ch2- i_{sq}, Ch3- i^*_{sq} (Scale: X-axis: 1.52 s/div, Y-axis: 0.424 pu/div)*

Fig.5.26 shows the oscilloscope trace of the shaft speed during starting.

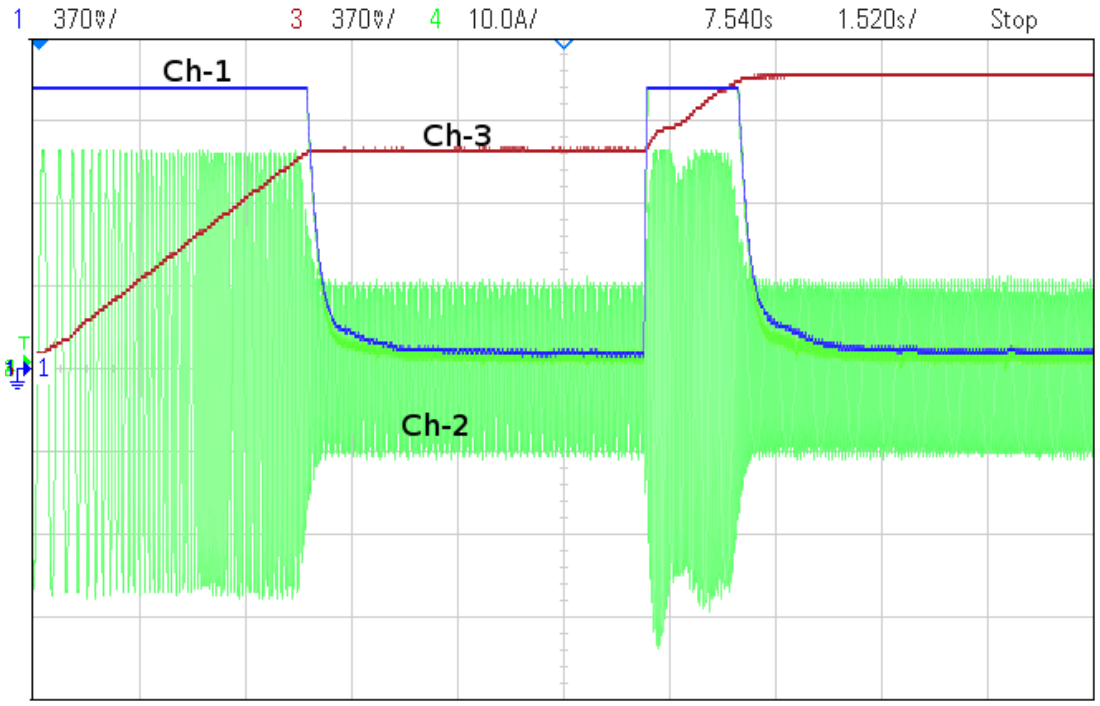

Figure 5.27: *Hardware result*: Response for a step change in speed reference *(Ch1- i_{sq}, Ch2- R-phase current,Ch3- Mechanical speed in pu Scale: X-axis: 1.52 s/div, Y-axis: Ch1,Ch3- 0.225 pu/div Ch2-10 A/div)*

Fig.5.27 shows the response of the R-phase current, i_{sq} and the shaft speed for a step change in speed reference from 0.6 pu to 0.8 pu.

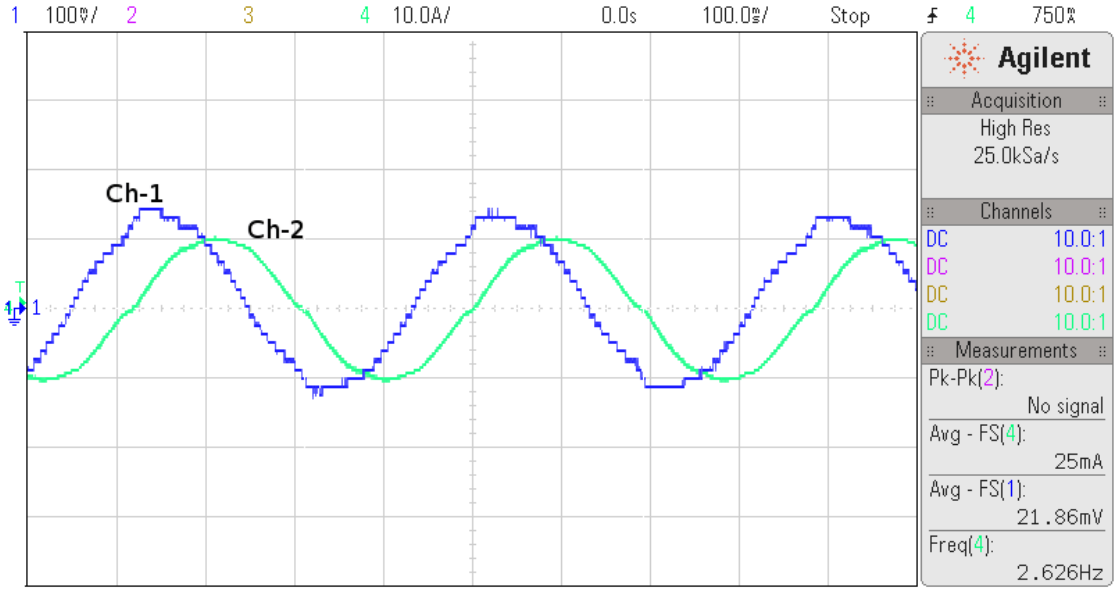

Figure 5.28: *Hardware result*: Low speed operation *Ch1- R-ph voltage, Ch2- R-ph current, (Scale: X-axis: 100 ms/div, Y-axis: Ch1- 0.06 pu/div, Ch2- 10 A/div)*

Fig.5.28 shows the phase voltage and phase current waveforms for a low speed operation at 2.6 Hz stator frequency in sensored vector control.

5.2.2 Sensorless Vector Control

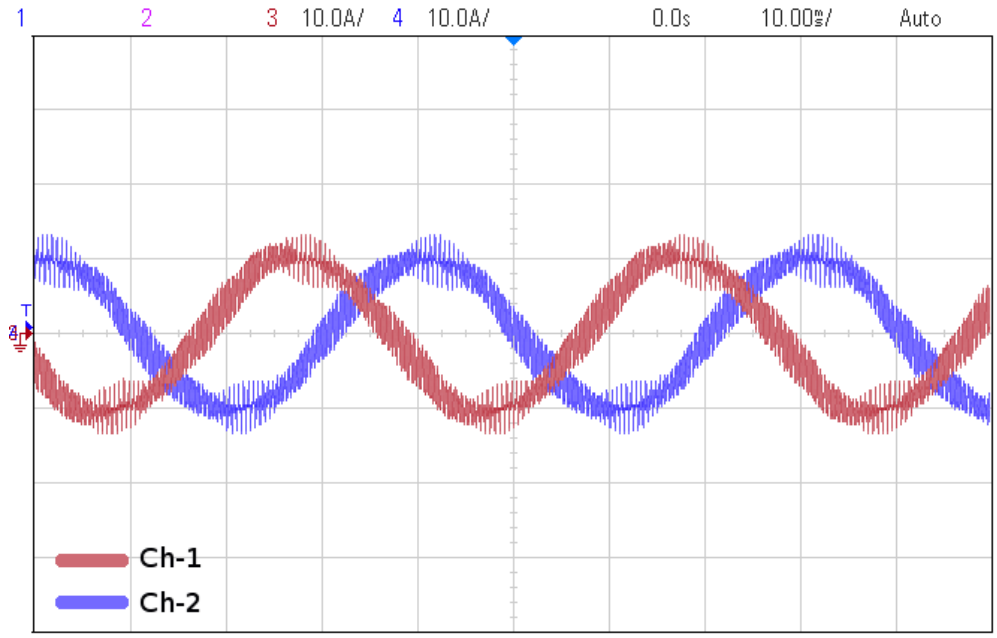

Figure 5.29: *Hardware result*: Phase current waveforms *Ch1- R-ph current,Ch2- Y-ph current Scale: X-axis: 10 ms/div, Y-axis: 10 A/div)*

Fig.5.29 shows the CRO waveforms of the R and Y phase currents at no load, steady state in sensorless vector control.

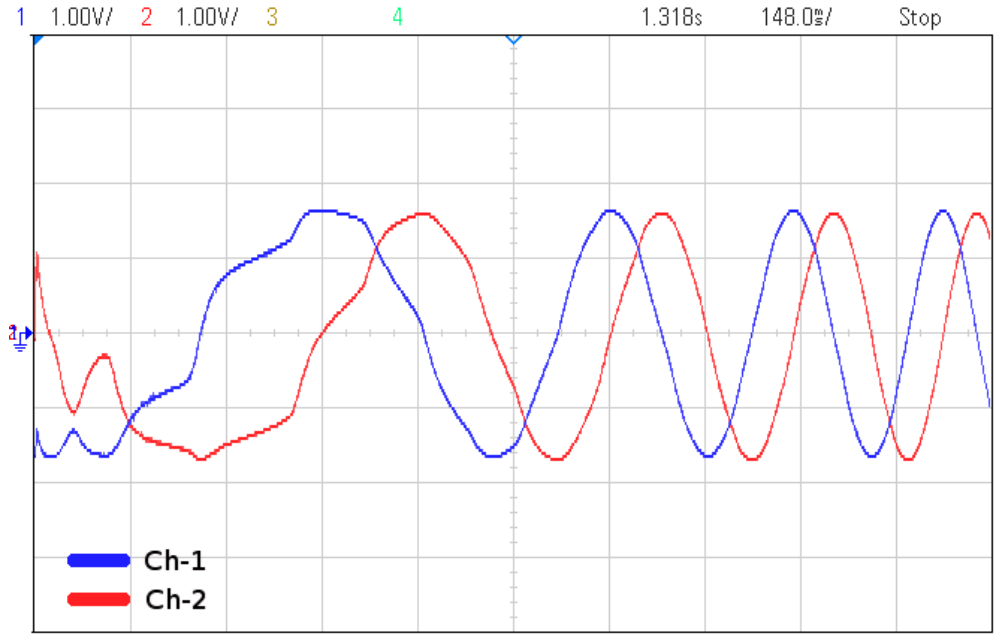

Figure 5.30: *Hardware result*: $\cos\rho$ and $\sin\rho$ at starting *Ch1-* $\cos\rho$*, Ch2-* $\sin\rho$*, (Scale: X-axis: 148 ms/div, Y-axis: 0.6 pu/div)*

Fig.5.30 shows the waveforms of $\cos\rho$ and $\sin\rho$ at starting in sensorless vector control using flux estimation scheme-I.

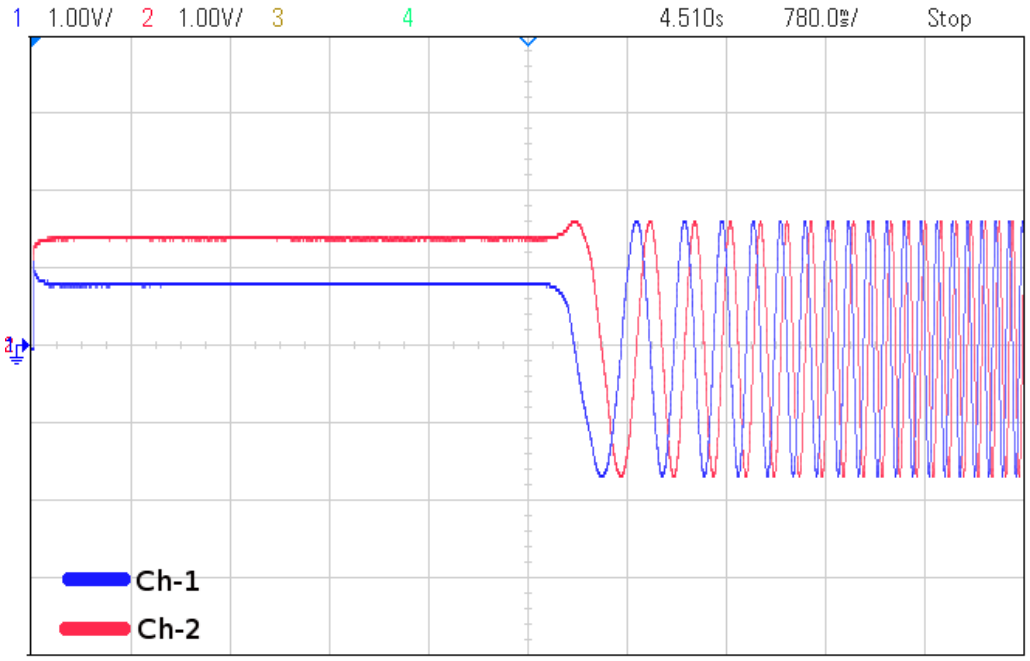

Figure 5.31: *Hardware result*: $\cos\rho$ and $\sin\rho$ at starting with scheme-II *Ch1-* $\cos\rho$, *Ch2-* $\sin\rho$, *(Scale: X-axis: 780 ms/div, Y-axis: 0.6 pu/div)*

Fig.5.31 shows the waveforms of estimated values of $\cos\rho$ and $\sin\rho$ at starting with flux estimation scheme-II and initial DC flux building.

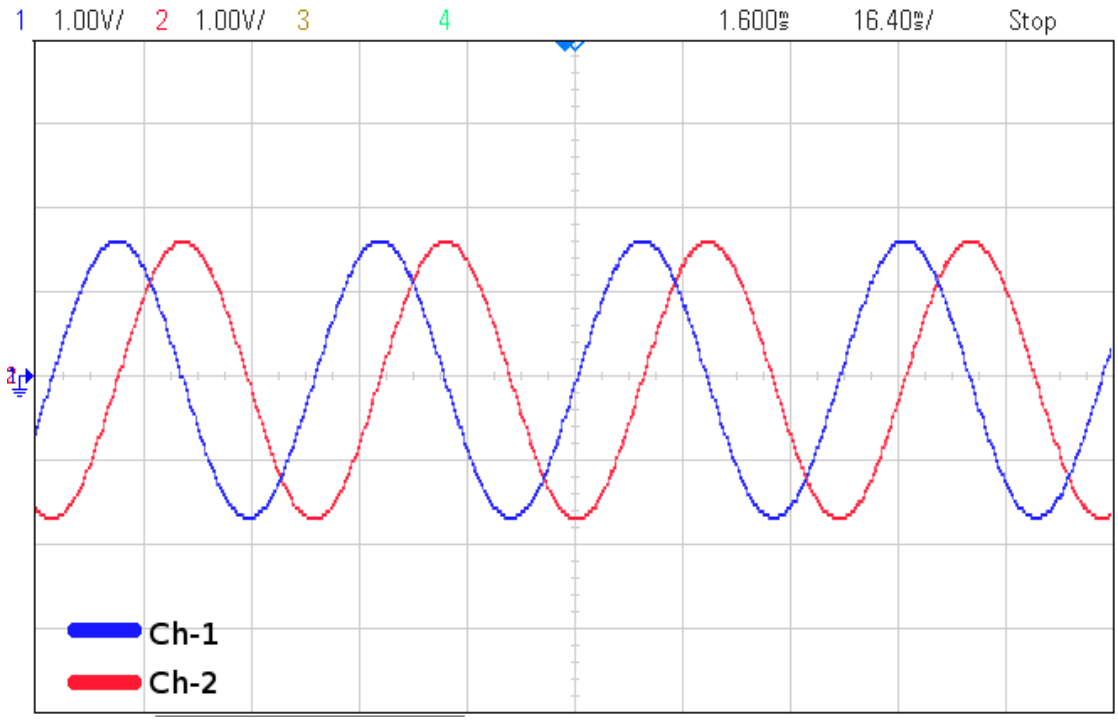

Figure 5.32: *Hardware result*: $\cos\rho$ and $\sin\rho$ at steady state *Ch1-* $\cos\rho$, *Ch2-* $\sin\rho$, *(Scale: X-axis: 16.4 ms/div, Y-axis: 0.6 pu/div)*

Fig.5.32 shows the waveforms of the estimated values of $\cos\rho$ and $\sin\rho$ at steady state using estimation scheme-II.

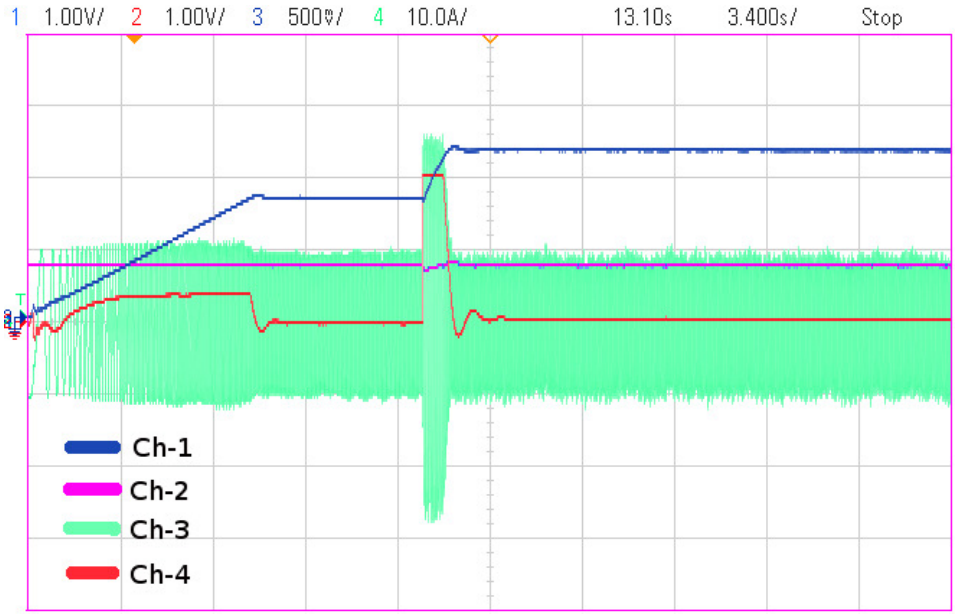

Figure 5.33: *Hardware result*: Starting response with scheme I and a step change in ω_{ref} *Ch1-* ω_m*, Ch2-* i_{sd}*, Ch3- R-phase current, Ch4-* i_{sq} *(Scale: X-axis: 16.4 ms/div, Y-axis: Ch1- 0.3 pu/div, Ch2,Ch4- 0.6 pu/div, Ch3- 10 A/div)*

Fig.5.33 shows the waveforms of the starting response of the drive in scheme-I and for a step change in ω_{ref} from 0.5 to 0.7 pu.

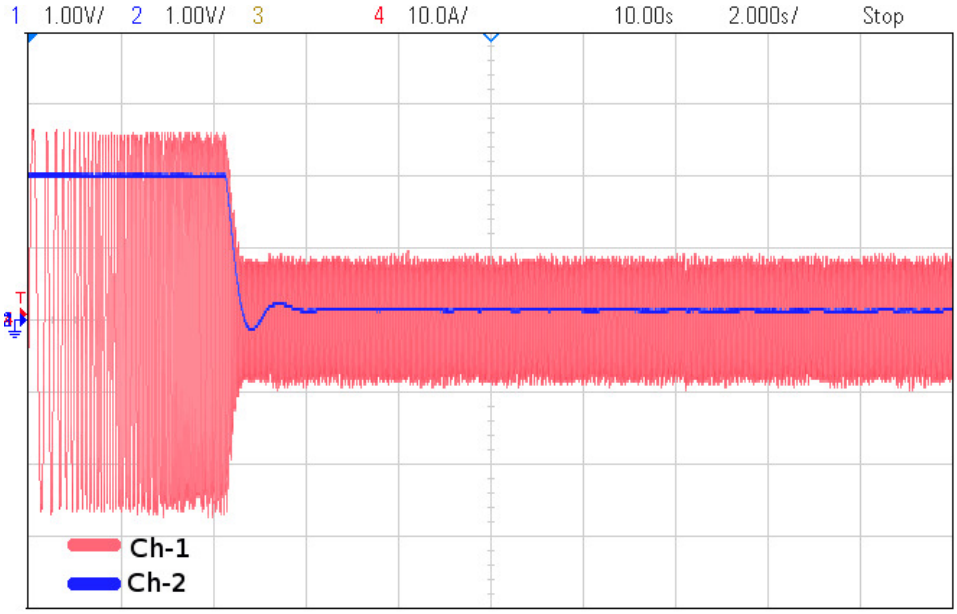

Figure 5.34: *Hardware result*: Starting response with flux estimation scheme II *Ch1- R-ph current, Ch2-* i_{sq}*, (Scale: X-axis: 2.0 s/div, Y-axis: Ch1- 10 A/div, Ch2- 0.6 pu/div)*

Fig.5.34 shows the R-phase current and i_{sq} for starting with estimation scheme-II.

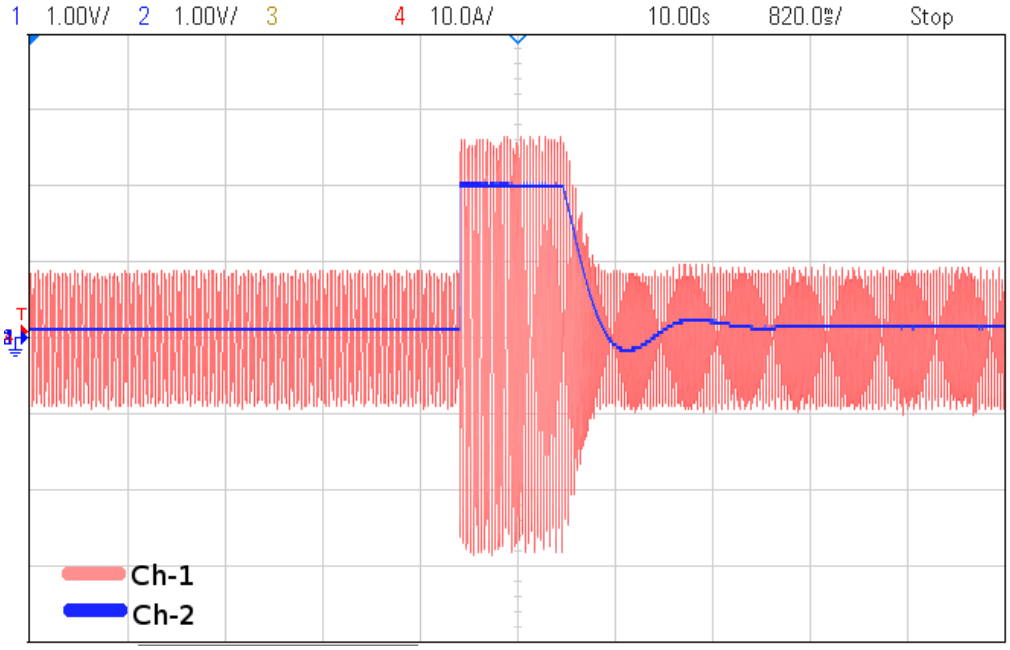

Figure 5.35: *Hardware result*: Response to a step change in ω_{ref} from 0.5 to 0.7 pu *Ch1- R-phase current, Ch2- i_{sq} (Scale: X-axis: 820 ms/div, Y-axis: Ch1- 10 A/div, Ch2- 0.6 pu/div)*

Fig.5.35 shows the response of the R-phase current and i_{sq} in estimation scheme-II for a step change in speed reference from 0.5 to 0.7 pu.

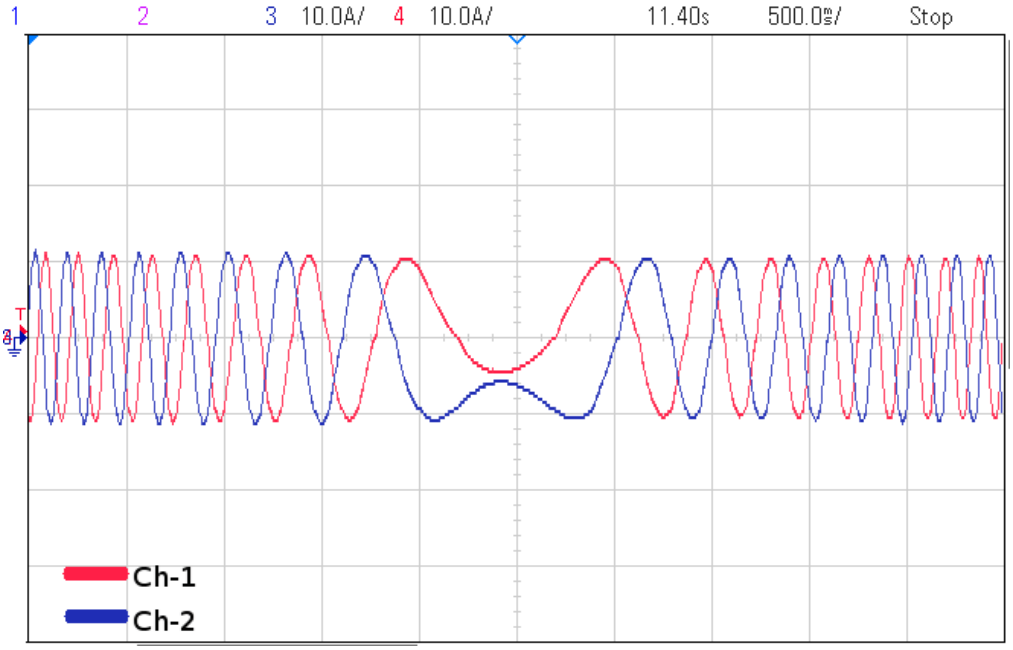

Figure 5.36: *Hardware result*: Phase currents during speed reversal *Ch1- R-phase current, Ch2- Y-phase current, (Scale: X-axis: 500 ms/div, Y-axis: 10 A/div)*

Fig.5.36 shows the waveforms of the R-phase and Y-phase currents during a speed reversal operation.

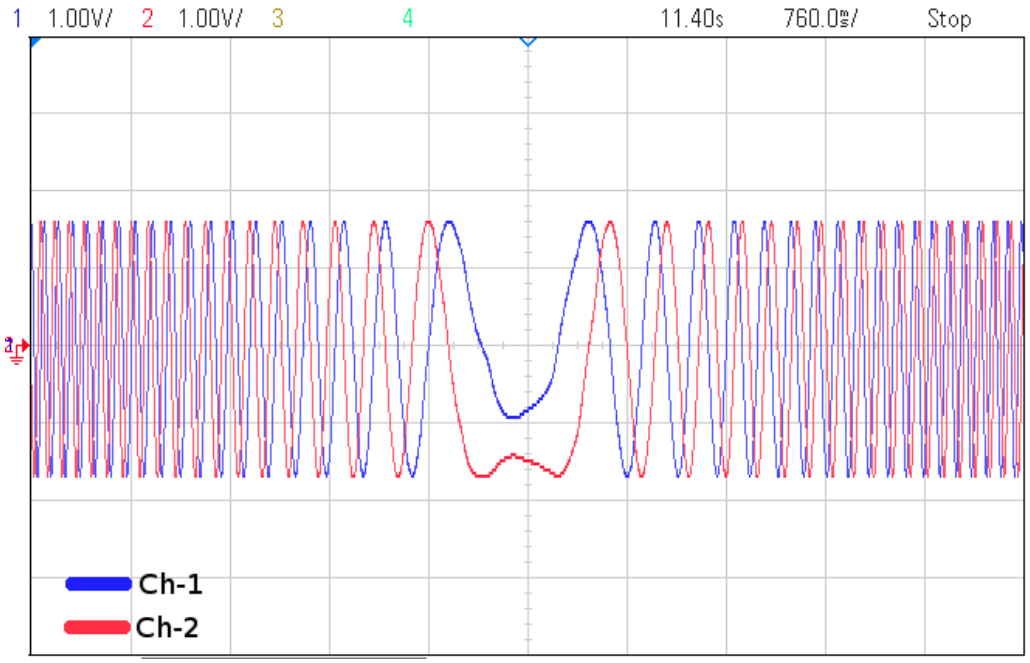

Figure 5.37: *Hardware result*: $\cos\rho$ and $\sin\rho$ during speed reversal *Ch1-* $\cos\rho$, *Ch2-* $\sin\rho$ *(Scale: X-axis: 760 ms/div, Y-axis: Ch1,Ch2- 0.6 pu/div)*

Fig.5.37 shows the waveforms of estimated $\sin\rho$ and $\cos\rho$ in sensorless control during a speed reversal operation.

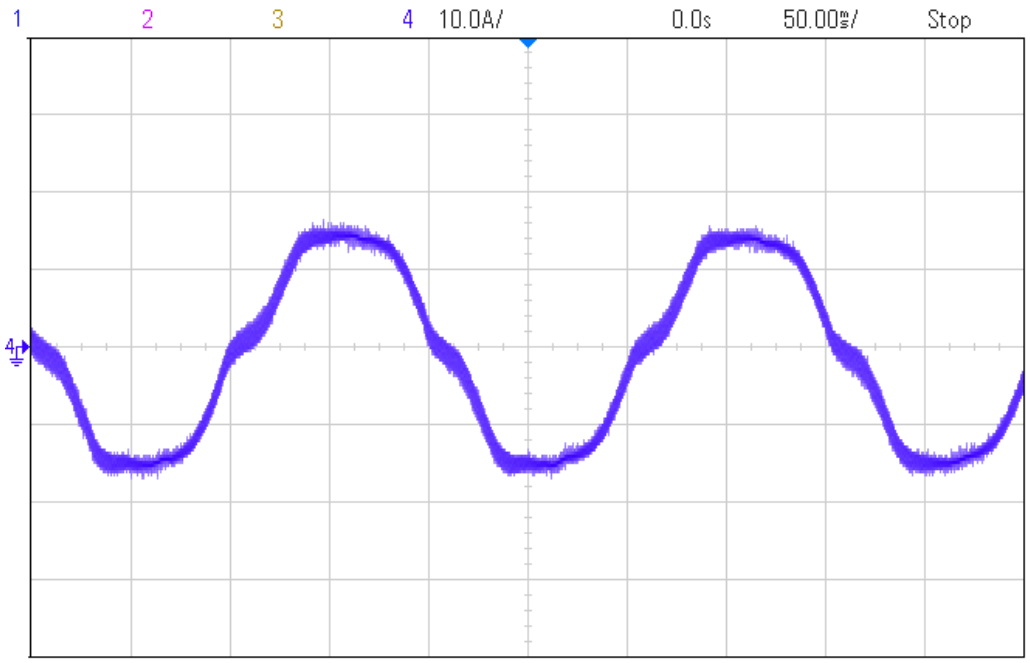

Figure 5.38: *Hardware result*: R-phase current in low speed sensorless operation *(Scale: X-axis: 50 ms/div, Y-axis: 10 A/div)*

Fig.5.38 shows the waveform of the R-phase current during a low speed sensorless operation at 5 Hz stator frequency. The effect of the 5^{th} and 7^{th} harmonics from the inverter dead time are visible at low speeds.

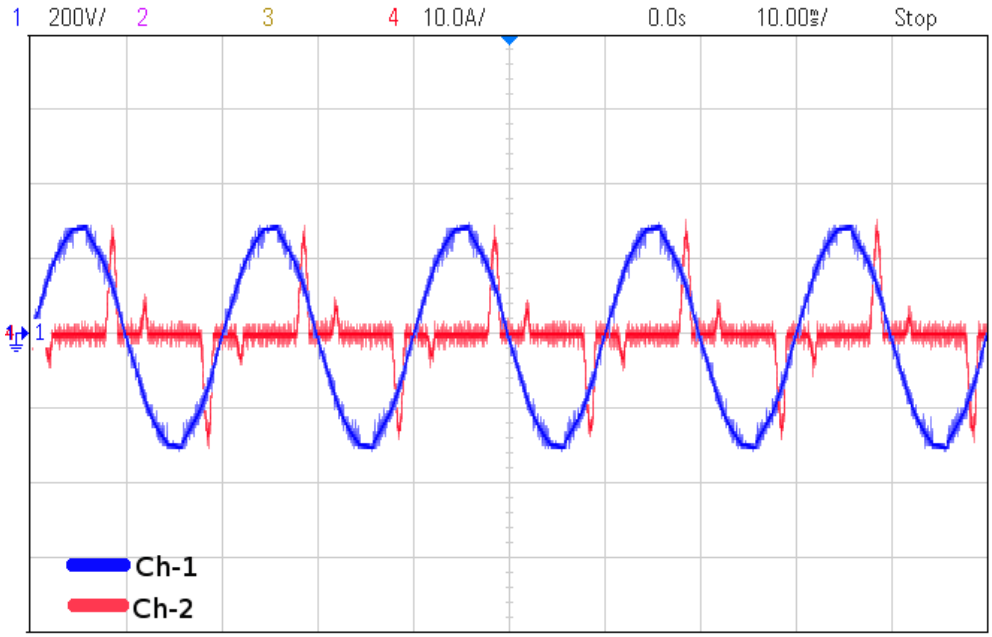

Figure 5.39: *Hardware result*: Rectifier input voltage and current at steady state *Ch1- R-Y line voltage, Ch2- R-phase input current (Scale: X-axis: 10 ms/div, Y-axis: Ch1- 200 V/div, Ch2- 10 A/div)*

Fig.5.39 shows the input R-Y line voltage and R-phase line current of the front end diode bridge rectifier at no load, steady state condition. The currents drawn by the rectifier are found to be highly distorted and peaky.

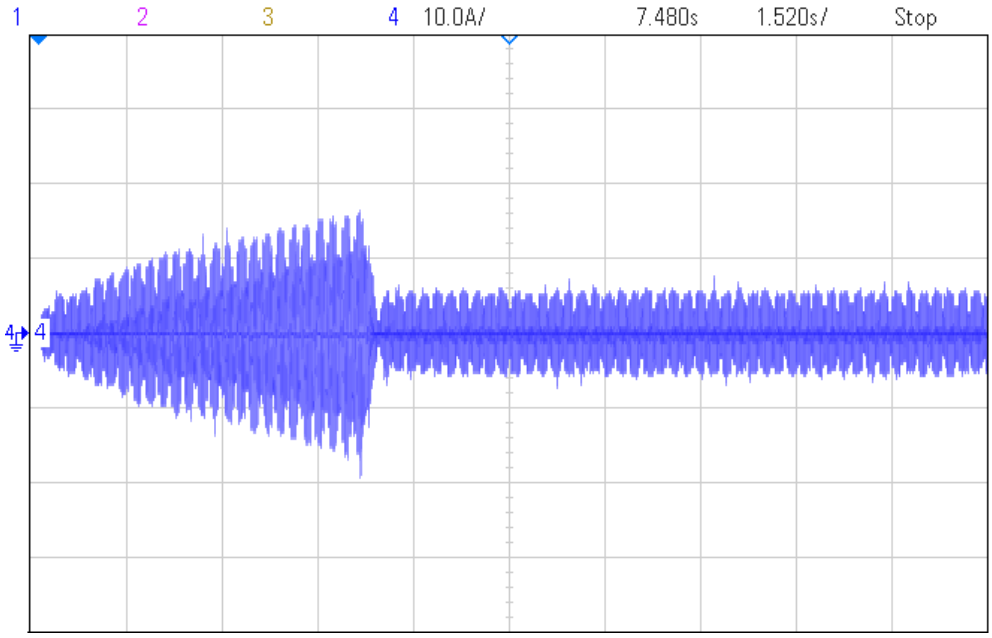

Figure 5.40: *Hardware result*: Rectifier R-phase input current profile during starting *(Scale: X-axis: 1.52 s/div, Y-axis: 10 A/div)*

Fig.5.40 shows the profile of the R-phase input current to the rectifier during starting of the drive.

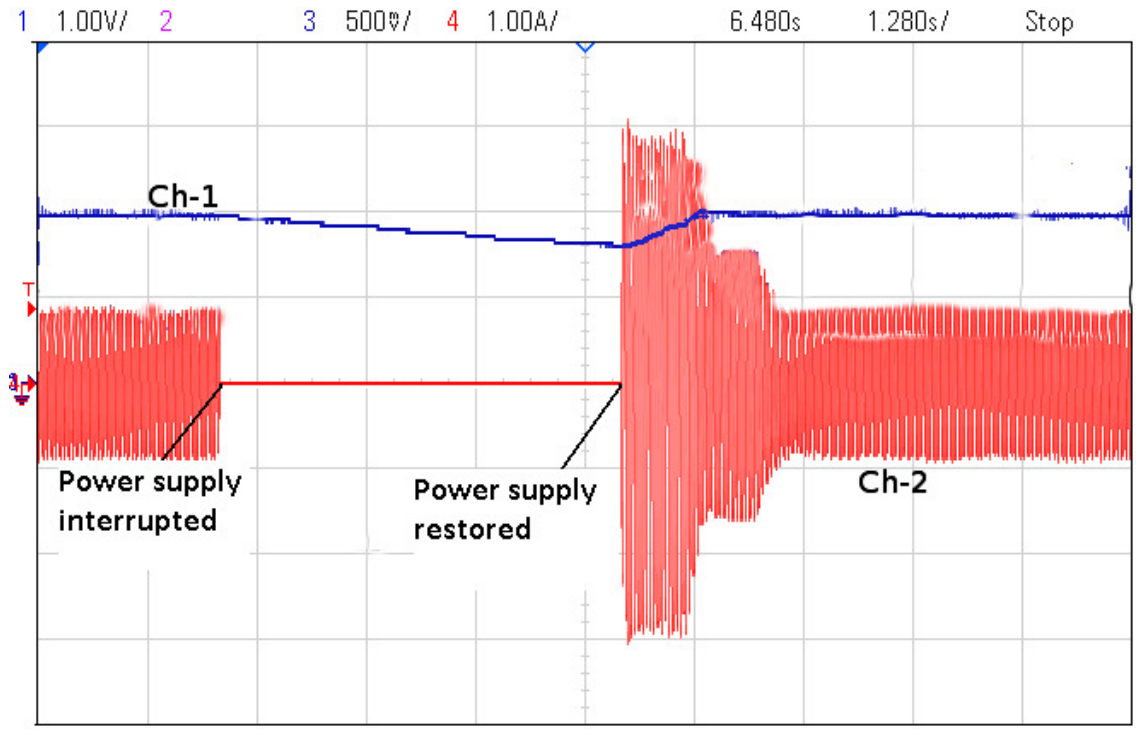

Figure 5.41: *Hardware result*: Speed waveform and R-phase current waveform during a power supply interruption ride through and on-the-fly starting *Ch1- Angular speed, Ch2- R-phase current(Scale: X-axis: 1.28 s/div, Ch1- Y-axis: 0.3 pu/div, Ch2- Y-axis: 10 A/div)*

Fig. 5.41 shows the waveforms of the speed and phase current for ride-through and on-the-fly starting for the sensored vector control. Phase current goes to zero at the moment of supply interruption as all pulses are stopped at this point. DC bus voltage is maintained and the speed falls due to the rotational losses. When the supply voltage is restored, the drive starts smoothly again. With a DC bus voltage of 300 V and the undervoltage setting of the precharge circuit kept at 250 V, a ride through time of upto 4 seconds could be obtained on no load. It can also be noted that the current waveform during the on-the-fly starting is kept within the limits by the PI controller.

5.3 Conclusion

The results from the simulating the sensored and sensoreless vector control for the 1 MW motor, and the experimental results from the actual implementation on the 30 kW motor were presented in this chapter. The experimental results are in close agreement with the simulated waveforms, thus validating the control design. Both

the flux estimation schemes for sensorless vector control were tested. However, the performance of scheme-II is found to be superior to scheme-I, especially at starting and for low speed operation. Low speed operation upto 1 Hz was achieved by the use of scheme-II. These experimental results show that extremely good performance can be achieved from the sensorless vector controlled drive, provided the machine parameters are accurately known. The suitability of the TMS320F28335 DSC for high performance drive applications is also established.

CHAPTER 6

CONCLUSION

6.1 Summary of the present work

The sensor based and sensorless vector control was successfully implemented in this project, on a 30 kW induction motor. The selection of the TMS320F28335 DSP for implementing the control algorithms facilitated and accelerated the implementation. With a sampling time of 100 μs, it was found that only about one-fourth of the processor power was utilised for running the control algorithms and the processor was idle for the remainining time. Since the knowledge of the flux position is critical in vector control, the performance of the sensorless vector control is extremely sensitive to the accuracy of the flux estimation algorithms. Two flux estimation algorithms based on stator voltage integration were tested in this work. The performance of scheme-I is not quite good at low frequencies and at starting while estimation scheme-II gives performance comparable to that of the sensored drive. Low speed sensorless operation upto 1 Hz could be achieved by using scheme-II. However, the inverter used in this work is rated at 10 kVA and therefore the dynamic response of the drive for full load conditions could not be tested. Simulation was done with the 1 MW BHEL machine for both sensored and sensorless control. The results obtained from the hardware are also found to be in close agreement with the simulation results.

6.2 Future Scope of Work

There remains a good scope of extending this project by adding additional features to the drive. The accuracy of estimation of the angular flux position is extremely dependent on the machine parameters. These parameters can drift with respect to time and also vary with temperature during operation. The variation of the stator resistance causes most problems for the sensorless control. Hence an online stator

resistance adaptation scheme[17] can be implemented to give greater accuracy of control. Also a self commissioning scheme[16], that can estimate the parameters of the drive at starting and tune the PI controllers accordingly will be advantageous. The implementation of a field weakening scheme can enable the drive to operate at speeds greater than rated, in a constant power mode. This will be useful in traction applications. The parameter variation that significantly affects the performance of the sensored drive is the rotor time constant variation. A scheme for rotor time constant adaptation[19] if implemented can improve the performance of the sensored drive also. Finally, it is possible to control several motors simulataneously to make use of the full power of the TMS320F28335, as the vector control of a single motor is far below the processing power of this DSP.

REFERENCES

[1] V.T. Ranganathan, *Course notes on Electric Drives* , IISc Bangalore, 2004.

[2] W. Leonhard. *Control of Electrical Drives.* Engineering online library. Springer Berlin Heidelberg, 2001.

[3] B.K. Bose. *Power Electronics And Motor Drives: Advances and Trends.* Elsevier Science, 2010.

[4] T.F. Chan and K. Shi. *Applied Intelligent Control of Induction Motor Drives.* Wiley, 2011.

[5] P.C. Krause and S. Studhoff. *Analysis of Electric Machinery.* IEEE, 2001.

[6] R. Krishnan. *Electric motor drives: modeling, analysis, and control.* Prentice Hall PTR, 2001.

[7] P. Vas. *Vector control of AC machines.* Monographs in electrical and electronic engineering. Clarendon Press, 1990.

[8] Blaschke. F. Apparatus for the field-related regulation of asynchronous machines, March 12 1974. US Patent 3,796,935.

[9] A. Wintrich, U. Nicolai, T. Reimann, W. Tursky, and SEMIKRON International GmbH & Co. KG. *Application Manual Power Semiconductors.* ISLE-Verlag, 2011.

[10] Frederik Sargos and SEMIKRON International GmbH & Co. KG. *Application Note: IGBT Power Electronics Teaching System.* AN-8005, Sep 2008.

[11] K.D. Hurst, T.G. Habetler, G. Griva, and F. Profumo. Zero-speed tacho-less im torque control: simply a matter of stator voltage integration. In *Applied Power Electronics Conference and Exposition, 1997. APEC '97 Conference Proceedings 1997., Twelfth Annual*, volume 2, pages 749–753 vol.2, Feb 1997.

[12] J. Holtz. Developments in sensorless ac drive technology. In *Power Electronics and Drives Systems, 2005. PEDS 2005. International Conference on*, volume 1, pages 9–16, 2005.

[13] J. Holtz, W. Lotzkat, and S. Stadtfeld. Controlled ac drives with ride-through capability at power interruption. *Industry Applications, IEEE Transactions on*, 30(5):1275–1283, Sep 1994.

[14] A. von Jouanne, P. Enjeti, and B. Banerjee. Assessment of ride-through alternatives for adjustable speed drives. In *Industry Applications Conference, 1998. Thirty-Third IAS Annual Meeting. The 1998 IEEE*, volume 2, pages 1538–1545 vol.2, Oct 1998.

[15] J. Holtz and Juntao Quan. Sensorless vector control of induction motors at very low speed using a nonlinear inverter model and parameter identification. In *Industry Applications Conference, 2001. Thirty-Sixth IAS Annual Meeting. Conference Record of the 2001 IEEE*, volume 4, pages 2614–2621 vol.4, Sept 2001.

[16] A.M. Khambadkone and J. Holtz. Vector-controlled induction motor drive with a self-commissioning scheme. *Industrial Electronics, IEEE Transactions on*, 38(5):322–327, Oct 1991.

[17] T. Bhattacharya and L. Umanand. Improved flux estimation and stator-resistance adaptation scheme for sensorless control of induction motor. *Electric Power Applications, IEE Proceedings* -, 153(6):911–920, November 2006.

[18] Seyoum, D; Rahman, MF and Grantham, C. Improved Flux Estimation in Induction Machines for Control Application. *Journal of Electrical Electronics Engineering, Australia*, Vol. 22, No. 3, 2003: 243-248.

[19] L. Umanand and S. R. Bhat. Adaptation of the rotor time constant for variations in the rotor resistance of an induction motor. In *Power Electronics Specialists Conference, PESC '94 Record., 25th Annual IEEE*, pages 738–743 vol.1, Jun 1994.

[20] Seung-Gi Jeong and M.-H. Park. The analysis and compensation of dead-

time effects in pwm inverters. *Industrial Electronics, IEEE Transactions on*, 38(2):108–114, Apr 1991.

[21] Texas Instruments. TMS320x2833x, 2823x Enhanced Pulse Width Modulator (ePWM) Module. *Texas Instruments Reference Guide, Literature Number:SPRUG04A*, Oct 2008.

[22] Texas Instruments. TMS320x2833x, 2823x System Control and Interrupts. *Texas Instruments Application Note, Literature Number:SPRUFB0D*, Mar 2010.

[23] Lori Heustess, Texas Instruments. Programming TMS320x28xx and 28xx Peripherals in C/C++. *Texas Instruments Application Note, Literature Number:SPRAA85D*, Jan 2013.

[24] Texas Instruments. TMS320F2833x ADC Module. *Texas Instruments Reference Guide, Literature Number:SPRU812A*, Oct 2007.

[25] Pradeep Shinde, Texas Instruments. Designing analog interface with TMS320F28xx/28xxx DSCs. *Texas Instruments Application Note, Literature Number:SPRAAP6A*, May 2008.

[26] Texas Instruments. TMS320x2833x, 2823x Enhanced Capture(eCAP) Module. *Texas Instruments Reference Guide, Literature Number:SPRUFG4A*, Jun 2009.